POLITECNICO DI TORINO
UNIVERSIDAD POLITÉCNICA DE MADRID

Double Master's Degree
Mechatronics - Automations and Robotics

Master's Degree Thesis

Design and Development of a Spherical Rover for Planetary Exploration

Supervisors
Prof. Stefano MAURO
Dr. Matteo MELCHIORRE
Prof. Claudio ROSSI

Candidate
Tommaso COLAMARTINO

July 2023

Resume

Spherical robots (SRs) play an important role in the field of mobile robots thanks to their several advantages over the classical wheeled and legged ones. Their spherical shell protects the inner components from possible contaminations (water, dust, etc.) and collisions; moreover, the symmetrical geometry makes impossible to overturn the robot. This allows the robot to make falls and to be thrown over obstacles without the risk of damaging or flipping. The spherical shape permits the robot to roll down a slope without any energy consumption. Moreover, some SRs, depending on their driving mechanism, can perform omnidirectional movements.

Because of these characteristics, SRs are an excellent choice for a wide range of applications. They are mainly thought for the exploration of unstructured, harsh, and hostile environments like planets, caves, pipes; inspection of disaster areas to assess damages and potential hazards; search and rescue (SAR) operations; underwater inspection, data collection, environment monitoring; surveillance, social services, indoor exploration, and child monitoring.

This master's thesis focuses on the design and development of a pendulum-driven SR, drawing inspiration from prior research conducted by [1]. The framework outlined in [1] successfully addressed some of the technical challenges associated with creating such a complex robot. To enhance the robot versatility, the work proposed in [1] an innovative differential mechanism to transfer the torque from the motors to the pendulum, allowing to place the motors far from the sphere center and lowering the Center Of Mass (COM) of the system. However, some limitations were identified, motivating further studies to enhance the robot's capabilities. The primary objective of this research was to develop a viable solution that could improve the robot's obstacle-climbing capability.

To achieve this goal, a performance parameter called Maximum Step Height (MSH) was defined. Its value is computed as the height of a step at which the SR, when generating the maximum torque, is able to maintain an equilibrium condition on the step edge. The MSH value of the SR designed by [1] was equal to 25 mm. The objective of this thesis consisted of improving it up to a value equal or greater than 100 mm.

For a simple pendulum-driven spherical robot it was shown that the MSH value depends only on the distance between the barycenter and the sphere center. The following equation represents this relation:

$$\frac{MSH}{R} = 1 - \sqrt{1 - \left(\frac{a}{R}\right)^2} \tag{1}$$

where R is the sphere radius and a is the position of the system COM from the sphere center. It can be observed that the only solution to improve the MSH consists in designing a system whose COM is as far as possible from the center of the sphere. Nevertheless, this complicates a lot the design process, and this solution was already implemented by [1].

The solution proposed in this thesis entails the integration of a Control Moment Gyroscope (CMG) system. The first part of this work was dedicated to study its working principle. It was explained how a CMG group is able to generate a temporary torque exploiting the principle of conservation of the angular momentum. When a flywheel is spinning with a high angular velocity about a first axis and it is tilted about a second axis perpendicular to the previous one, a torque is generated along a third direction defined by the right hand rule. Coupling two gyroscopes with opposite spinning and tilting velocities, the result is a varying torque along a constant direction. Its magnitude is described through the following equation:

$$\tau_G = 2I\omega\Omega \; cos\,(\Omega \cdot t) \tag{2}$$

where I is the flywheel inertia about the spinning axis, ω is the spinning velocity, and Ω is the tilting velocity.

An innovative spherical robot driving mechanism composed only by gyroscopes was proposed. It was demonstrated that two three-gimballed gyroscopes allow to generate a torque along any desired direction, making the robot omnidirectional. However, after a detailed analysis, it was concluded that this system couldn't be used to meet the project requirements. Hence, the CMG group was selected as an auxiliary propulsion system to be coupled with a pendulum and the differential mechanism developed by [1].

When needed, the CMG can be used in order to generate a torque that opposes to the pendulum raising movement. This is equivalent to an instantaneous increase of the pendulum weight without changing the barycenter position. As a consequence, more torque is needed to maintain the pendulum at a 90° angle, and therefore more torque is transferred to the sphere shell. Consequently, the MSH does not depend only on the COM but also on the generated gyroscopic torque. Equation 1 can be corrected by substituting the barycenter position with a new term that accounts also for the gyroscopic torque:

$$a^* = a + \frac{\tau_G}{(m_p + M_s)g} \tag{3}$$

From this equation it can be observed that the MSH is no longer a barycenter position constraint, but rather a design guideline that can be used to compute the gyroscopic torque needed to overcome a step of height h knowing the robot barycenter position a.

After this preliminary study, the design process of the robot started, paying a

DESIGN AND PROJECT REQUIREMENTS	
Diameter	0.5 m
Max. Mass	25 kg
a/R	0.35
Nominal Speed	2.5 m/s
Nominal Slope Angle	15°
Runtime at Nominal Condition	1h
MSH	0.1 m

Table 1: Design guidelines and objectives of the project. The nominal working point is defined by the nominal speed and the nominal slope angle.

particular attention to fulfil the project requirements shown in table 1. First, the design of the CMG group was realized. A comprehensive study with the aim of optimizing the flywheel dimension was conducted. To select the spinning motors, a thorough analysis of the losses due to the air friction was realized. After finalizing the design of the CMG group, the two main motors controlling the pendulum were dimensioned, selecting them based on the nominal robot speed requirement of 2.5 m/s.

Once all the motors were selected, the main structure of the pendulum was designed in order to support all the internal components. This allowed to define the distance of the main motors from the center of the sphere, which was used to dimension the belt transmission necessary to transfer the torque from the motors to the differential system developed by [1].

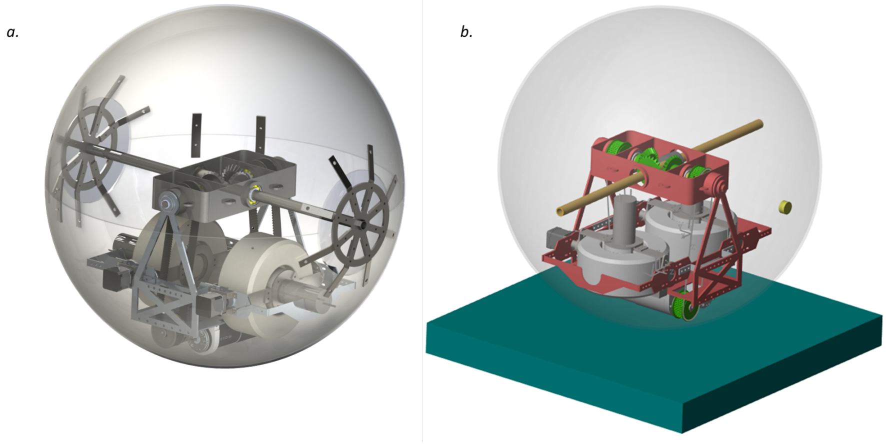

Figure 1: a) Rendering of the SR from Sloidworks. b) The same SR assembled in Simscape.

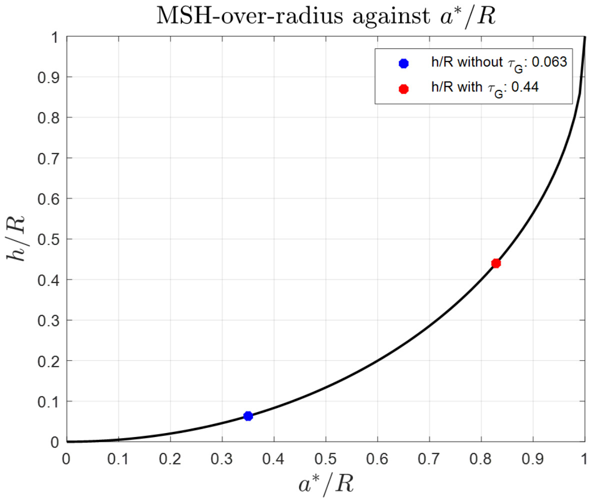

Figure 2: Curve representing *MSH/R* VS a^*/R. The red point identifies the *MSH/R* value when using the gyroscopes, while the blue one when not using them.

The battery pack was dimensioned to meet the runtime requirement of a minimum of 1 h while working at the nominal operating point (climbing a slope of 15° at a speed of 2.5 m/s).

For the spherical shell, the harmonic steel sheets used in [1] were substituted with two PMMA hollow hemispheres. A second layer made of impermeable rubber is needed to enhance the static friction of the shell on the ground, like in [1].

The final result of the design process can be seen in fig. 1(a), where a rendering of the SR model realized in Solidworks is shown. Its diameter is equal to 0.5 m, and its total mass is 18 kg. The batteries and the hardware weren't included, but the whole dimensioning process was performed considering a total mass of 22 kg, allowing for the inclusion of hardware components weighing up to 4 kg while still adhering to the project requirements.

After completing the design process of the SR, simulated models were created to study its performance. An analytical model able to describe the straight motion on an inclined plane was developed, and linear speed controllers were designed based on this model. More comprehensive multibody models of the SR were utilized to verify the project requirements and test the designed controllers. In fig. **??**(b), the multibody model of the SR realized in Solidworks is shown.

The results demonstrated that the CMG system successfully enhanced the robot's obstacle overcoming capability. Through a simplified multibody model incorporating all the specifications obtained from the design process it was shown that the CMG system allowed to successfully climb steps with the expected height. In fig. 2, the curve derived from the representation of eq.1 is plotted and two points have been marked.The blue one corresponds to the MSH over radius of this robot without the aid of the gyroscopes, which only depends on the barycenter position. The red one, instead, represents the MSH that can be overcame when the gyroscopes are functioning with the spinning and tilting velocities defined during the design, which are 8000 rpm and 15 rpm, respectively. The MSH/R is increased from a value of 0.06325 to 0.8285, which correspond to steps of a height equal to 15.8 mm and 110 mm, respectively. In fig. 3, four frames of the SR overcoming the step are shown. The first one shows that the robot is standstill in front of the step with the pendulum raised at 90°. The mere barycenter offset doesn't allow the robot to overcome the obstacle. In the subsequent frames, the spinning gyroscopes start the tilting motion, leading to an increase of the total torque transmitted to the spherical shell and allowing the robot to finally overcome the step.

However, when testing the robot's obstacle overcoming capability and the linear speed controllers on the more comprehensive multibody models with the differential mechanism developed by [1], discrepancies between the expected and obtained results were observed. These findings highlighted the challenges associated with controlling the spherical robot through the differential mechanism.

Overall, this master's thesis made significant progress in the design and development of a pendulum-driven spherical robot, presenting a viable solution to improve its obstacle-climbing capability. The integration of a Control Moment Gyroscope auxiliary propulsion system showed promise in enhancing the robot's performance. Further research should focus on selecting the appropriate hardware components, designing a rubber cover with surface features to enhance gripping capabilities, and developing a control system capable of controlling the robot on both straight and curvilinear paths. These future efforts will contribute to advancing the field of spherical robotics and maximizing the robot's capabilities in various applications.

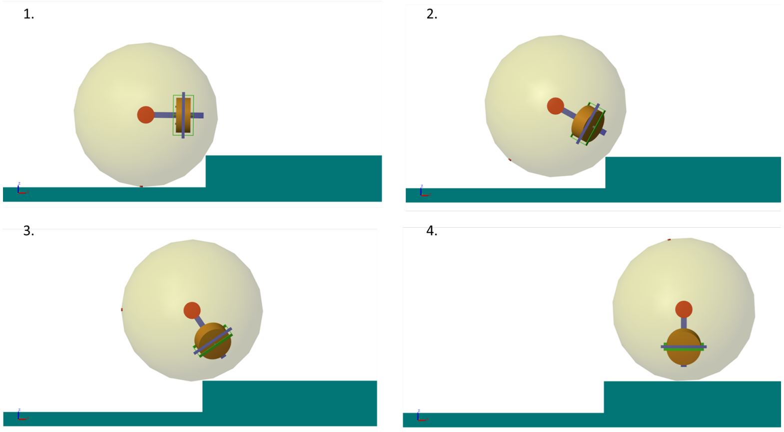

Figure 3: Four frames of the simplified model of SR overcoming a step of 110 mm.

Table of Contents

List of Tables

List of Figures

Acronyms

SR

Spherical Robot

SAR

Search And Rescue

UGV

Unmanned Ground Vehicle

BCO

Barycenter Offset

DOF

Degree Of Freedom

MSH

Maximum Step Heigh

MSA

Maximum Slope Angle

CMG

Control Moment Gyroscope

IMU

Inertia Measurements Unit

RW

Reaction Wheels

Chapter 1

Introduction

Spherical robots (SRs) play an important role in the field of mobile robots thanks to their several advantages over the classical wheeled and legged ones. Their spherical shell protects the inner components from possible contaminations (water, dust, etc.) and collisions; moreover, the symmetrical geometry makes impossible to overturn the robot. This allows the robot to make falls and to be thrown over obstacles without the risk of damaging or flipping. The spherical shape permits the robot to roll down a slope without any energy consumption. Moreover, some SRs, depending on their driving mechanism, can perform omnidirectional movements.

Because of these characteristics, SRs are an excellent choice for a wide range of applications. They are mainly thought for the exploration of unstructured, harsh, and hostile environments like planets, caves, pipes; inspection of disaster areas to assess damages and potential hazards; search and rescue (SAR) operations; underwater inspection, data collection, environment monitoring; surveillance, social services, indoor exploration, and child monitoring.

This thesis presents the design and development of a spherical mobile robot. The inspiration for this prototype was drawn from the spherical Unmanned Ground Vehicle (UGV) developed by M. Melchiorre et al. [1], which provided a solid foundation upon which the current prototype was built. The original project is shown in figure 1.1. The driving mechanism was selected by [1] after realizing a trade-off analysis of the state-of-the-art spherical robot propulsion systems. Design, performance and control simplicity are the main characteristics that were studied to carry out the choice. The single pendulum driving system was selected by [1] as the best possible choice. It belongs to the Barycenter offset (BCO) propulsion mechanisms, and it is characterized by a 2 Degrees Of Freedom (DOF) pendulum attached to a central diametral shaft, which is anchored to the robot spherical shell. When the motors lift the pendulum, a reaction torque acts on the sphere, causing it to move.

The framework described in [1] enabled to overcome some of the technical

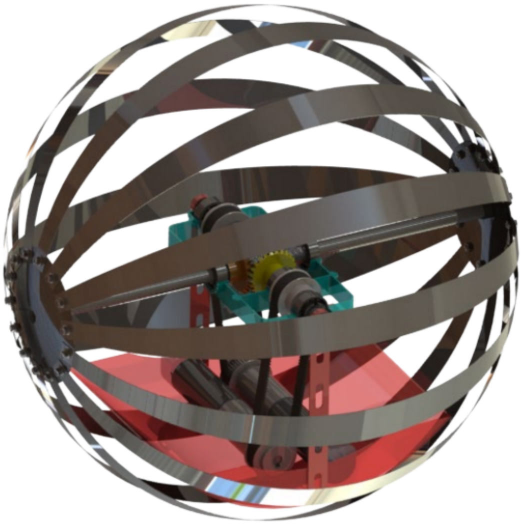

Figure 1.1: Rendering of the SRs designed by M. Melchiorre et al. [1].

challenges associated with developing such a complex robot. At the meantime, the limitations of its design [1] were identified, and a significant effort was made to improve the efficiency and versatility of the robot. One of its main drawbacks was its limited maximum torque, which negatively affected its ability to overcome obstacles.

The first part of this work was dedicated to find a viable solution to this issue. At first, an alternative to the BCO driving mechanism was considered, with a propulsion system made only of Control Moment Gyroscopes (CMGs). However, due to the complexity of designing and controlling the system, along with the limitations of this driving mechanism, it was decided to use it only as an auxiliary driving system to be paired with the 2 DOF pendulum described in [1]. Therefore, an optimal design for the CMGs and internal components of the robot was studied to improve the robot obstacle-surmounting ability. Once the design was finalized, a multibody simulation was conducted and the control of the robot was studied.

Max. Step Height	25 mm
Max. Slope Angle	15°
Min. Velocity	2.5 m/s
Min. Acceleration	0.5 m s2
Max. Diameter	0.5 m
Max. Mass	25 kg

Table 1.1: Design specification of the spherical robot by [1]

1.1 Project Objectives

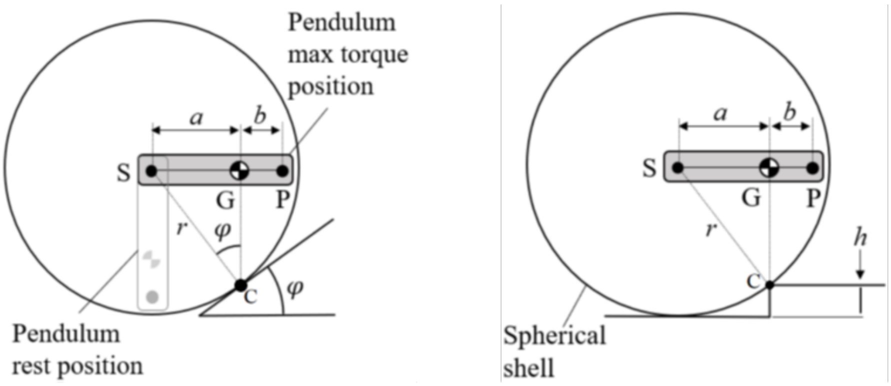

Figure 1.2: Analysis of limit cases of incline (a) and step (b). Image from [1].

The design specifications of the original project [1] are listed in table 1.1. Two performance parameters were defined to evaluate the robot capability of climbing slopes and obstacles: the “Maximum Step Height” (MSH), and the “Maximum Slope Angle” (MSA). Both are calculated solving a static equilibrium problem. The MSA refers to the maximum slope angle at which the robot can maintain an equilibrium condition while generating the maximum torque (which for a pendulum-driven robot is obtained when the pendulum is at 90°, fig. 1.2(a)). The MSH, instead, is determined as the height of a step at which the SR, when generating the maximum torque, can maintain an equilibrium condition on the step edge (fig. 1.2(b)).

The limited MSH value of the original robot [1] is due to the BCO driving system. In static conditions, this type of SRs can develop a maximum driving torque when raising the pendulum at a 90° angle (Figure 1.2) and it only depends on the system barycenter distance from the sphere center. As a matter of fact, a static equilibrium is possible only when the barycenter of the robot is vertically aligned with the contact point between ground and sphere (point C in Figure 1.2). Two significant relationships can be deduced from this observation. Having defined “a” as the distance between the barycenter and the sphere center:

$$\frac{a}{R} = \sin\varphi \quad \longrightarrow \quad \varphi = \arcsin\frac{a}{R} \tag{1.1}$$

$$\frac{a}{R} = \sqrt{1-(1-\frac{h}{R})^2} \quad \longrightarrow \quad \frac{h}{R} = 1-\sqrt{1-(\frac{a}{R})^2} \tag{1.2}$$

The first one defines the equilibrium condition of the sphere on a slope; φ is the angle of the slope and it’s equal to the MSA. The second one defines the

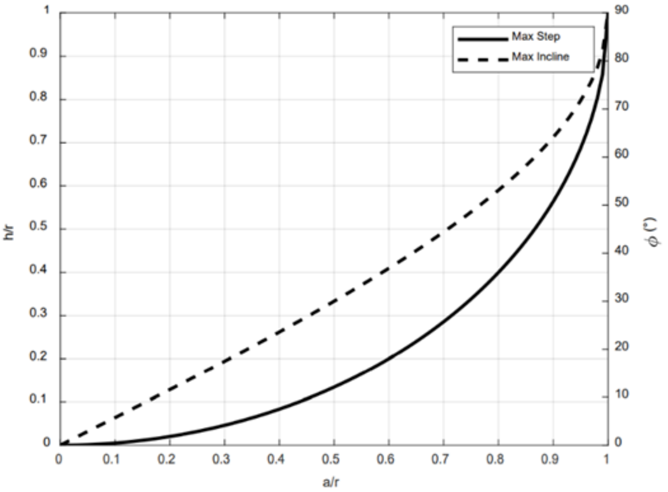

Figure 1.3: MSA and MSH-over-Radius curves obtained from the static equilibrium equation. Image from [1].

equilibrium condition between the sphere and a step; h is the height of the obstacle and it's the MSH. In Figure 1.3, a plot of the two equations above is shown. It should be noted that the MSH-over-radius curve exhibits a much more pronounced nonlinear behavior. As a result, to overcome higher steps, it is necessary to place the sphere barycenter as close as possible to the shell. This provides a crucial guideline in the design process of the robot. By defining the MSH as one of the project objectives, it becomes possible to calculate the lower bound for the distance between the barycenter and the sphere center. Nevertheless, this may complicate a lot the design process.

The addition of a CMG auxiliary propulsion system allows to relax this constraint. As it will be explained in Chapter 3, the CMG group can be used to generate a temporary torque that opposes to the pendulum raising movement. This is equivalent to an instantaneous increase of the pendulum weight without changing the barycenter position. As a consequence, more torque is needed to maintain the pendulum at a 90° angle, and therefore more torque is transferred to the sphere shell. Hence, the MSH is no longer a barycenter position constraint, but rather a design guideline that can be used to compute the gyroscopic torque needed to overcome a step of height h once the robot barycenter position has been fixed.

The only constraint to the barycenter position is now defined by the MSA the robot is required to climb. In the previous project [1] this parameter was chosen to be $\varphi = 15°$, as indicated in Table 1.1. Consequently, the ratio between the barycenter position and the sphere radius is approximately $a/r \approx 0.26$. However, it's worth noting that the smaller this ratio, the greater the gyroscopic torque required to overcome obstacles, which could lead to a more challenging design.

Therefore, a minimum ratio of 0.35 was chosen as reference. Consequently, the correspondent MSA is approximately $\varphi \approx 20.5°$. Without the use of any gyroscopic group, the MSH would be equal to $16mm$.

The objective of the project consisted in developing a CMG system to improve the obstacle overcoming capability of the robot while meeting the design requirements. A reference value for the MSH was chosen, which is MSH= $100mm$. A list of the other design requirements of the project is shown in table 1.2.

DESIGN AND PROJECT REQUIREMENTS	
Diameter	0.5 m
Max. Mass	25 kg
a/R	0.35
Nominal Speed	2.5 m/s
Nominal Slope Angle	15°
Runtime at Nominal Condition	1h
MSH	100 mm

Table 1.2: Design guidelines and objectives of the project. The nominal working point is defined by the nominal speed and the nominal slope angle.

1.2 Contribution of this Work

This thesis makes a significant contribution to the field of pendulum-driven spherical robots by addressing the challenge of limited Maximum Step Height (MSH) due to the barycenter position. The contributions of this work are as follows:

Firstly, a comprehensive state-of-the-art review is provided, establishing the foundation for the research. A novel concept design of a CMG-only-propelled spherical robot is proposed. However, due to the complexity limitations of this design, it was decided to use the CMG group only as an auxiliary propulsion system. This innovative integration strategy advances the field of propulsion systems in spherical robots and offers a practical solution to enhance their performance.

While similar solutions have been described in the literature ([2],[3],[4]), many of them remain unimplemented or abandoned. In contrast, this thesis presents a thorough overview of the design process for the CMG auxiliary propulsion system. Extensive efforts were dedicated to maximizing the robot's MSH while adhering to the project's design specifications. The design process covers the study of CMG systems' principles, the design of gyroscopes, the selection of CMG motors, and the dimensioning of the motors responsible for the control of the pendulum integrated with the auxiliary propulsion system.

To better understand the robot's functioning, an analytical model representing the dynamics of the spherical robot rolling along a straight path is proposed.

This analytical model serves as a foundation for developing a linear speed control architecture, enabling precise control of the robot's velocity along a straight path.

Furthermore, more comprehensive multibody models are employed to evaluate the performance of the designed robot. Through these simulations, the effectiveness of the CMG system in enhancing obstacle overcoming capability is demonstrated, providing practical insights into the implications of the proposed design.

Overall, this thesis contributes significantly to the field of pendulum-driven spherical robots by addressing the limited MSH challenge and presenting a novel design incorporating a CMG auxiliary propulsion system. The comprehensive design process, analytical modeling, and evaluation using multibody simulations contribute to the knowledge base of researchers and engineers in the field, advancing the development and application of spherical robots.

Chapter 2

State of the Art

2.1 Introduction

In the following paragraphs, an up-to-date state of the art of the Spherical Robots (SRs) is presented. It focuses on the most common driving mechanisms that have been developed so far, presenting some of the most recent paper about this topic.

2.2 Spherical Mobile Robots: Driving Mechanism Classification

In this section, a State of the Art of the SRs is presented, classifying them on the basis of the driving mechanisms that have been developed so far. Gravity Driving, and Shape Transformation methods are the most common ones. Some other propulsion strategies can be found in the literature, such as RW (Reaction Wheels), CMG (Control Moment Gyroscope), and Differential Driving Systems. Each one of these driving mechanisms is individually covered in the next paragraphs, explaining their functioning, and presenting several examples. Finally, some less popular propulsion systems are analyzed.

2.2.1 Gravity Driving Methods: Barycenter Offset

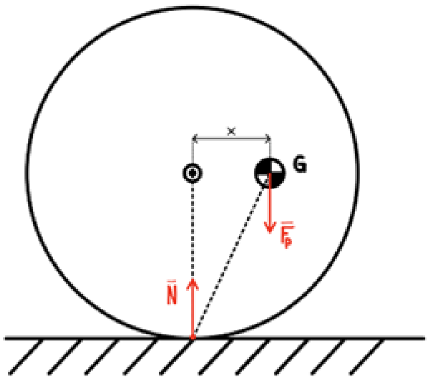

Figure 2.1: 2D representation of a spherical robot with the barycenter displacement

The gravity driving method consists of an internal system that displaces the barycenter of the SR. Consequently, an eccentric torque is generated, causing the robot to roll towards the barycenter position. This locomotion strategy allows to move on flat surfaces, overcome small obstacles, and climb-up gentle slopes. Barycenter offset is mainly generated through two mechanisms: using a 2-DOF pendulum (**pendulum driving strategy**) or by means of an internal driving unit (IDU). The IDU consists in a single wheel or in a wheeled platform that climbs up the inner shell surface (**hamster ball**). Another mechanism that has been used in some prototypes is the so called "**Shifting Masses**" strategy, which is composed by several masses that can linearly displace inside the robot along fixed shafts. A few more systems of marginal interest have been developed; two examples are presented at the end of this section.

Pendulum Driving Strategy

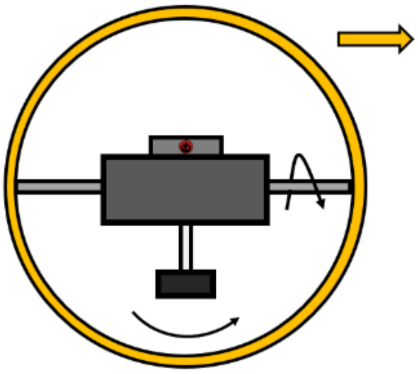

Figure 2.2: Sketch of a single pendulum driving mechanism. Image from [5].

The pendulum driving strategy consists of a 2-DOF pendulum that can swing around the pitch and roll axes of the robot. It is usually attached to a central diametral shaft. A schematic representation of the system is presented in Figure 2.2. When the motors lift the pendulum, a reaction torque acts on the sphere, causing it to move. The design of this SR can be quite challenging, and its main disadvantages are its lack of omnidirectionality and limited torque.

A first example of pendulum spherical robot is GroundBot from Rotundus AB [6] (Figure 2.3(c)); with a diameter of 60cm, it can reach 3 m/s. The unit is equipped with cameras mounted in clear domes on the sides of the robot and can be operated from a sophisticated telepresence command station. It can be commanded to patrol a route autonomously using GPS.

GroundBot was chosen by M. Seeman et al. [7] for a study on the autonomy of a surveillance robot. They were able to point out the several advantages of spherical robots, such as stability and robustness; some drawbacks were met, such as the image stabilization problem due to the uncontrolled oscillations. GroundBot represents one of the best of its kind but when it comes to overcome obstacles, it has some limitations due to its driving mechanism.

S. Xie et al. [8] developed a spherical mobile robot for polar region scientific research. It can navigate thanks to the internal pendulum system or by exploiting the wind thrust. Two motors control the forward and lateral swing of the pendulum.

Y. Ping et al. [9] developed a pendulum-driven "[...] spherical robot carrying a binocular stereovision, referred to as Visionbot. Stereovision is used to enhance the environmental perception of spherical robots, thus reducing cumulative errors caused by sliding, mechanical clearance, and model error". Therefore, a motion control technique that exploits visual feedback is proposed; the overall goal is to realize an autonomous robot. [7] and [9] are two of the few papers that cover the

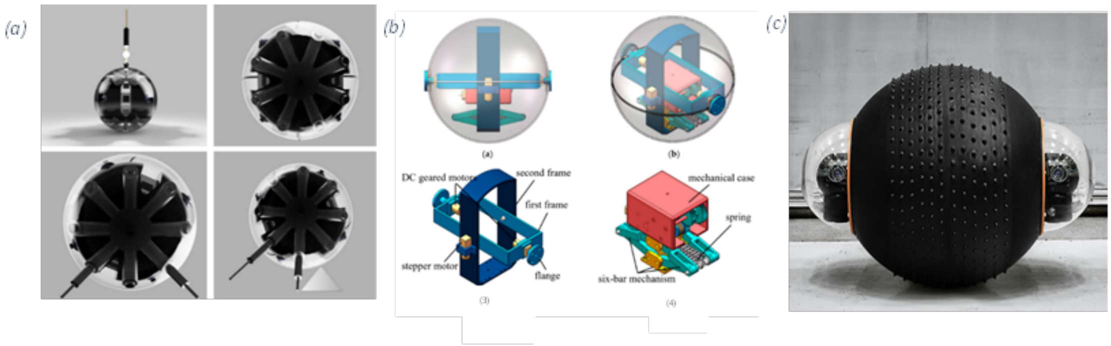

Figure 2.3: (a) Rendering of the DAEDALUS robot [11]. (b) prototype of a rolling and jumping spherical robot [12]. (c) GroundBot from Rotundus AB [6].

autonomous driving in the field of spherical robots.

M. Yang et al. [10] tried to overcome one of the limitations of this type of driving mechanism. When the pendulum is attached to the central shaft, its range of motion around the roll axis is limited by the shaft itself. To solve this problem, they realized a structure where the pendulum is mounted inside a squared shape instead of a simple shaft. A similar solution can be found in [8]. Tow pairs of motors are used to control the two DOF of the pendulum.

A. P. Rossi et al. [11] presented an example of pendulum driven SR named DAEDALUS. The aim of this model is to explore and characterize the entrance of Lunar lava tubes (Figure 2.3(a)). The election of a spherical mobile robot instead of a classical rover is due to the protection that the spherical shell assures to the internal components (sensors and scientific equipment) and the higher stability in unstructured terrain. Extendable pods that come out of the shell are used to improve the locomotion capabilities, to increase the stability during data collection and to prevent failures.

F. Wang et al. [12] presented a novel design of spherical robot characterized by a multi-mode motion: rolling and jumping. The jumping is realized through

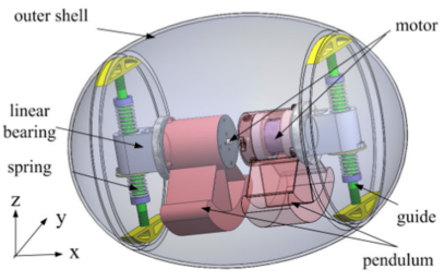

Figure 2.4: Double pendulum driven spherical robot [13]

a spring mechanism that can release the elastic potential energy stored, allowing it to hop up to a height of 17cm. The rolling, instead, is achieved through the barycenter offset caused by the swinging of the jumping driving module, which is used as a pendulum (Figure 2.3(b)).

Most of the pendulum driven spherical robots in the literature are characterized by a single pendulum system, like the ones presented above. However, a little number of double-pendulum-driven SR can be found [14], [13]. An example is the one developed by Zhao et al. [13] for reconnaissance and unstructured hostile environment exploration (Figure 2.4). The main characteristic of this type of spherical robot is the semi-omnidirectionality: through a synchronous rotation of the two pendulums in opposite directions, the inertia moment around the yaw axis is the only force acting on the sphere, causing the robot to turn in place.

Hamsterball (Direct Driving Methods)

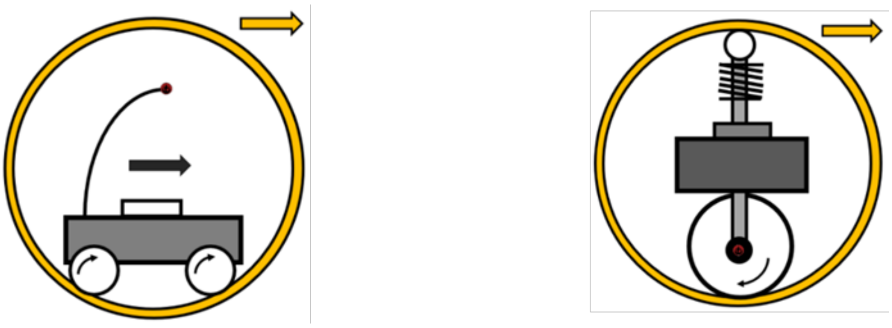

Figure 2.5: Sketch of multi-wheeled (left) and a single-wheeled (right) IDU. Images from [5]

The hamster ball driving system consists of a multi/single wheeled mobile robot placed inside the spherical shell and usually referred as IDU (internal driving unit). When the IDU moves, it climbs up the internal surface of the sphere, causing the barycenter to displace towards the desired direction.

This system has several advantages: the barycenter is closer to the shell surface with respect to a pendulum driven system, which allows maximizing the output torque. The design is simple, and the driving mechanism is straightforward to control. In some hamster-ball-driven spherical robots, the IDU is kept in place through a tensioning element, that is usually a platform or a rod with a wheel placed at the top. The introduction of the tensioning element is important for preventing the IDU from slipping or overturning.

One of the biggest problems of this system is that the internal surface of the sphere needs to be as uniform as possible to maintain the friction between the

IDU wheels and the shell. Collisions with obstacles could cause the loss of contact between wheels and surface too, and, in the worst case, the overturning of the robot [4].

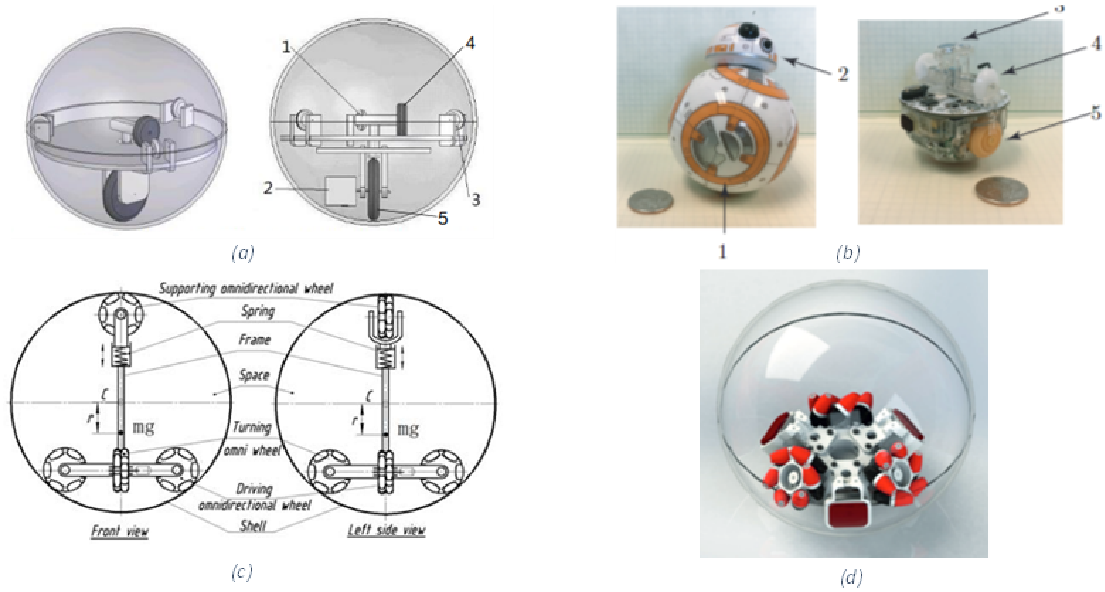

Figure 2.6: :(a) Structure of BHQ-3: (a1) Motor2, (a2) Motor1, (a3) Sponge wheels, (a4) Steering wheel, (a5) Driving wheel. (b) BB-8 from SPHERO: (b1) and (b2) are the spherical shell and cap, (b3) mechanism that actuates the cap, (b4) wheels to maintain contact with the shell, and (b5) the driving wheels. (c) Robot described in [15]. (d) Model developed by Y. L. Karavaev and A. A. Kilin [16]

The omnidirectionality of the robot depends on the type of wheels of the IDU. The most recent developed hamster-ball-driven robots are characterized by omni wheels, which allow omnidirectional movements [15, 16, 17]. A simpler design based on classic wheels can enable both quasi-omnidirectional and omnidirectional movements [18, 19, 20]. Below, a more in dept analysis of some prototypes is presented.

Q. Zhan et al. [18] present BHQ-3, a hamster-ball-driven spherical robot that can perform omnidirectional movements. Its IDU is characterized by two simple wheels: a bigger one, that is the driving wheel, and a second one used to steer the driving one. The driving wheel is in contact with the inner surface of the shell, and it climbs up the sphere causing the barycenter to move; the sphere rolls due to the moment of gravity. The second wheel rotates on a central platform that is kept in contact with the inner surface of the shell through three sponge wheels. The authors realized a prototype of the mobile robot: with a 150 mm radius, the robot was able to climb a 17° slope and cross a 3 cm height obstacle. It must be noticed that, compared to an omnidirectional wheel, this system needs to actuate the steering wheel to place the driving one along the desired direction, and only then the robot will move (Figure 2.6(a)).

A. Singh et al. [19] realized a modular snake robot composed by three spherical robot modules. Each one of these modules takes inspiration from BHQ-3. Omnidirectional motion, and the ability to navigate in marshy, wet, and sandy terrains without any risk for the internal components are the main reasons why the authors decided to use spherical modules. The main difference from the Q. Zhan et al. prototype consists in the use of a pinion-crown gear system instead of the small steering wheel. This solution prevents the steering wheel from slipping.

Y. L. Karavaev and A. A. Kilin [16] developed a spherical robot with a three omni-wheeled IDU (2.6(d)). Omni-wheel axes are rotated of 45° with respect to the wheels plane to ensure contact with the internal surface of the shell. The authors present both a kinematic and a dynamic model of the problem and various control architectures. A similar prototype has been developed by P. D. Ba et al. [15].

W. Liu et al. [17] developed a novel design of spherical robot with an actuation system that combines a multi-wheeled platform with a supporting rod. In particular, the internal driving unit consists of a platform with 4 omnidirectional wheels (MECANUM wheels) actuated by two motors, one for each pair of wheels. To prevent the platform from overturning and to keep the wheels always in contact with the surface, a rod is placed perpendicular to the platform and has at the top an omni wheel rolling on the surface of the opposite hemisphere (2.6(c)).

A hamster-ball-driven spherical robot that had a lot of success is the “Sphero Bolt” by Sphero, a coding robot that lets kids learn coding through hands-on play and STEAM activities and is nowadays on the market. In [20], the internal components of a Sphero BB-8 robot are presented: a semispherical structure holds all the electronics and the two actuators used to actuate the two driving wheels (2.6(b)).

Other Barycenter Offset Strategies

The hamster ball and the pendulum driving mechanisms are the most common propulsion systems adopted for spherical mobile robot motion. Among the barycenter displacement driving strategies, there are a few more of marginal interest. A first example is the shifting masses method. It consists of several masses that can displace inside the robot along fixed linear guides. Compared to the pendulum driving strategy, this system allows omnidirectional movements, and a more precise control of the barycenter position. However, the mechanical design and the necessary control architecture are very complicated; the efficiency of the system is low because high power actuators are needed to perform faster and smoother movements. Moreover, collisions at the points where the linear guides are attached to the shell are undesirable.

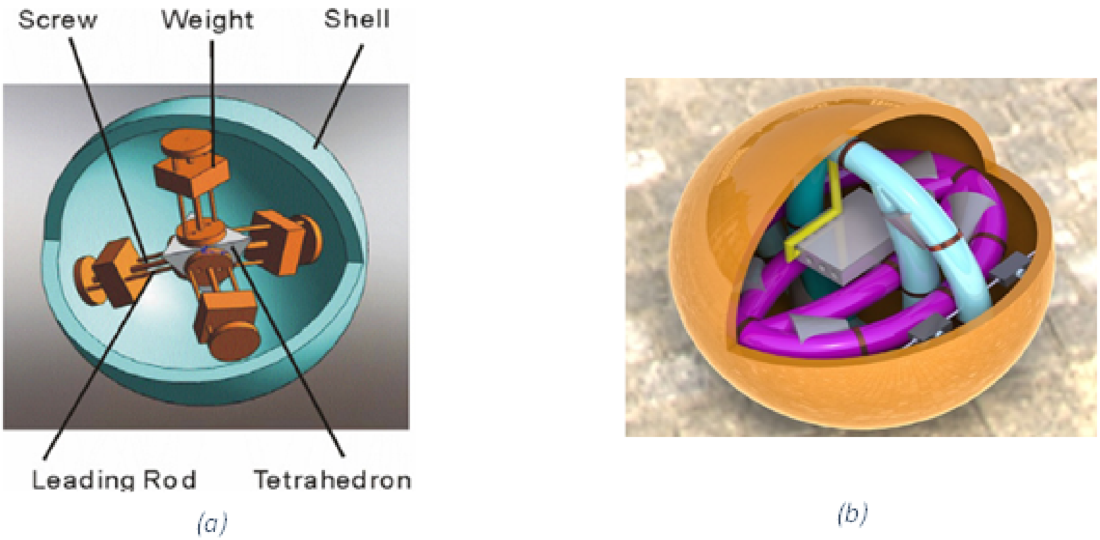

(a)

(b)

Figure 2.7: (a) Spherical robot designed by S. Sang et al. [21]. (b) Fluid actuated spherical mobile robot [22]

An example of this type of system is the one developed by S. Sang et al. [21] (Figure 2.7(a)). The propulsion system is composed by "four power screwed spokes, connected in 109.47° inside a tetrahedral shape". "There are four heavy objects (heavy shortly or weight), placed through spokes, which are elevated upward and downward using four stepper motors [. . .]". Another example of driving system is the one developed by S.A. Tafrishi et al. [22]. They presented a study of a fluid actuated spherical mobile robot (Figure 2.7(b)). Their model is characterized by an inner pipe structure where an incompressible fluid circulates driven by a hydraulic system. The displacement of the fluid generates the moment needed for robot motion. Among the pipes, the ones responsible for the forward (pitch) and lateral (roll) motion can be distinguished. One of the main benefits of this novel type of actuation is the absence of the unstable points that characterize the pendulum-like systems.

L. Jia et al. [23] designed a type of amphibious spherical robot that can navigate underwater and autonomously head toward the water thanks to a double inverted pendulum mechanism (Figure 2.8). The robot is characterized by a spherical shell where the batteries, the payloads, three DC motors, and the control board are encapsulated. Two arms are attached to the sides of the hull and two propellers are placed at the end of the arms. The rolling movement is performed displacing the center of gravity of the robot using the arms as inverted pendulums. To change the heading direction, a small flywheel is placed inside the shell and is rotated, generating a reaction force on the structure that will cause a change in the yaw angle (COAM driving mechanism). The underwater navigation is performed through the propellers placed at the end of the arms. Two small grippers are placed next to the motors for manipulation tasks.

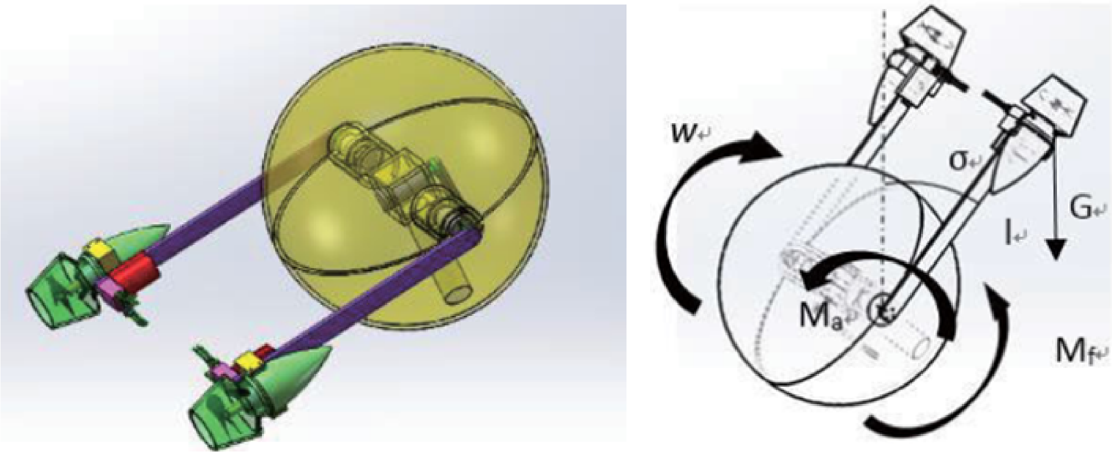

Figure 2.8: Amphibious robot by L. Jia et al. [23]; 3D rendering (left) and inverted pendulum driving mechanism (right).

2.2.2 Shape Transformation Spherical Robots

The shape transformation spherical robots include two groups that exploits two different propulsion strategies: the shell deformation, which consists in deforming the spherical shape in such a way that will generate a driving force; the hybrid robots, which can transform their structure to change the propulsion method. The most common are the hybrid ones; a lot of robots able to roll and perform another type of movement can be found in the literature. The main advantage of being able to transform the shape is the significant enhancement of the cross-obstacle ability while maintaining the spherical shape benefits. On the other hand, the mechanical design and the control architecture of this type of robot are much more complicated. In the next paragraphs, some examples of crawling and rolling, flying and rolling, amphibious, and soft inflatable spherical robots are presented.

Crawling And Rolling SR

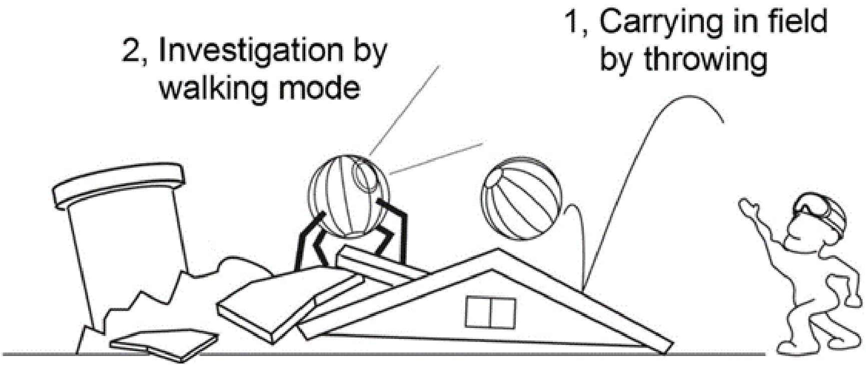

Figure 2.9: Application concept of a hybrid walking and rolling robot. Image from [24].

This type of robots is characterized by the ability of walking and rolling. They can be in a closed configuration, exploiting the rolling motion for a less power-consuming travel, or they can extend their legs and crawl. The walking ability improves the capability of obstacle crossing and solves the limited maximum torque problem of pendulum and hamster-ball driven spherical robots. At the same time, the spherical shape ensures the several advantages of a SR. The application concept of a hybrid walking and rolling robot is shown in Figure 2.9.

S. Kamon et al. [25] presented a model of reconfigurable robot that can transform from a sphere into a three-legged walking robot using a linear motor. It doesn't have any driving module that allows its control while it's in the spherical configuration; in this case, the ball-shape is exploited to protect the robot and its inner mechanism from collisions. For its locomotion, 10 motors are used, 3 for each leg and one linear motor for opening/closing the upper hemisphere of the shell while transforming.

T. Aoki et al. [24] developed another example of rolling and walking spherical robot called QRoSS V (Figure 2.10(a)). The robot can transform from a storage state, where the legs are inside the spherical shell, to a configuration where the legs are deployed outside the shell. Their prototype is characterized by an external shell made of SMA (shape memory alloys) wires fixed to a central pole through flanges; the 4 legs of the robots are fixed to the central rod and can be stored inside the outer shell. Inside the central pole is placed an air dumper to absorb the shock in the axial direction. The rolling motion is performed through a leg kick. The experimental results show that the robot is able to overcome a 14cm obstacle.

N. Bun-Athuek and P. Laksanacharoen [27] developed another example of reconfigurable spherical robot. It can crawl thanks to its three legs or roll on its spherical shell (Figure 2.10(c)). The robot structure consists of two hemispheres connected through an actuated mechanism that enables the opening of the shell; the legs are placed on the edge of the hemispheres, two on one side and the third on the other side. To perform the rolling movement the legs are used to push the sphere in the desired direction; it must be noticed that the control action can

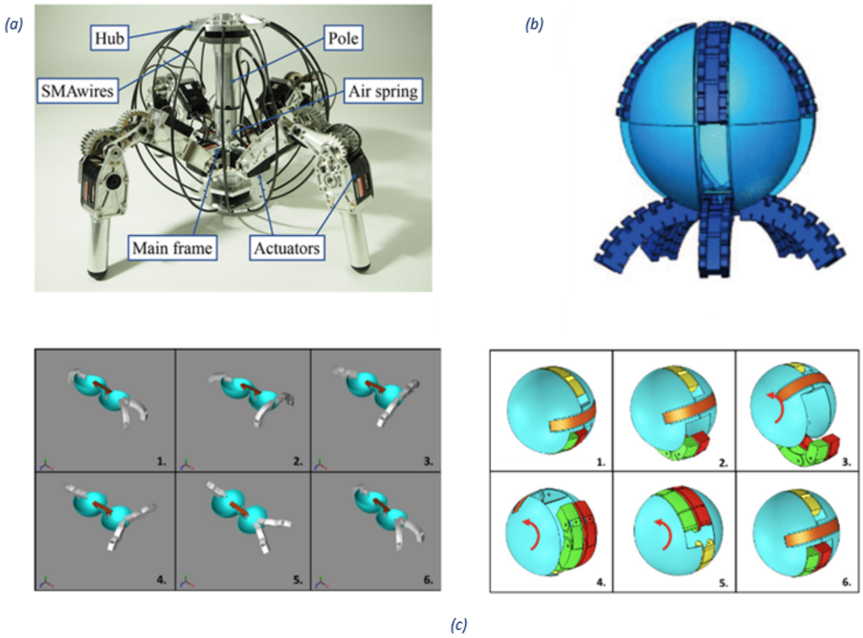

Figure 2.10: (a) QRoSS V robot [24]. (b) Soft spherical robot by J. Pan et al. [26]. (c) Butterfly movement and rolling movement concept of the reconfigurable spherical robot by N. Bun-Athuek and P. Laksanacharoen [27]

be performed only when the legs are in contact with the ground. The walking movement consists of a butterfly swimming motion where 2 legs pull the two half hemispheres while the third one pushes it.

J. Pan et al. [26] presented a prototype of soft spherical robot inspired by organs and modularity of organisms such as starfish and octopuses (Figure 2.10(b)). The robot is composed by two hemispherical 3D printed shells kept together by electromagnets. On each one of these 2 hemispheres, 5 silicone gel robotic feet are placed. Their movement is controlled through SMA springs, two for each foot. These feet are used both for crawling and to push the robot to make it roll when closed in a spherical shape. Moreover, the two hemispheres can separate and can move independently to overcome obstacles or navigate through smaller spaces.

Amphibious SR

This category of spherical robots includes all the ones that are designed to move on land and navigate underwater. Li M. et al. [28] presented in their paper a prototype of spherical amphibious robot able to quadruped walking on land and navigating underwater thanks to a water-jet propulsion system 2.11. Its structure is characterized by a reconfigurable spherical shell that opens its lower half when walking. The choice of a spherical structure was driven by the maximum internal space it provides, the advantages of a symmetrical shape both on land and underwater and the possibility to move in confined spaces. Inside its shell it carries several micro-robots that can collect/manipulate underwater object or monitor the environment in a restricted space.

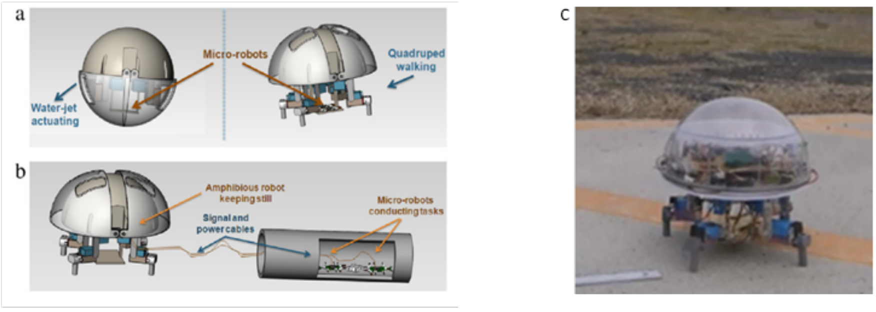

Figure 2.11: (a) Spherical robot moving towards the water. (b)Micro-robots conducting tasks in restricted spaces. (c) Image of the prototype.

Soft Inflatable SR

Among the spherical robots characterized by the ability of transforming their shape, some inflatable robots can be found.

K. Ho and N. M. Mayer [29] a prototype of spherical robot composed by 12 inflatable sections; the motion of the robot is performed through deflating and inflating these segments (Figure 2.12(a)). To stay in a still position, “the section towards the ground is deflated and sunken.” To move forward, “the above-mentioned section is inflated while the neighboring section towards the intended direction is deflated”. The actuation and control system are placed in the center of the sphere. The possible advantages of this robot are the same of the other soft robots: ability of navigating in an unstructured field, safe human interaction, etc.

Flying And Rolling SR

Finally, an interesting prototype of spherical robot able to roll, crawl, and fly has been developed by M. Zhang et al. [30] (Figure 2.12(b)). These motion modes have been combined to exploit their respective advantages and to enhance the robot applicability across various situations. The robot can flexibly switch between the motion modes, as the authors demonstrated via simulations in the Gazebo environment.

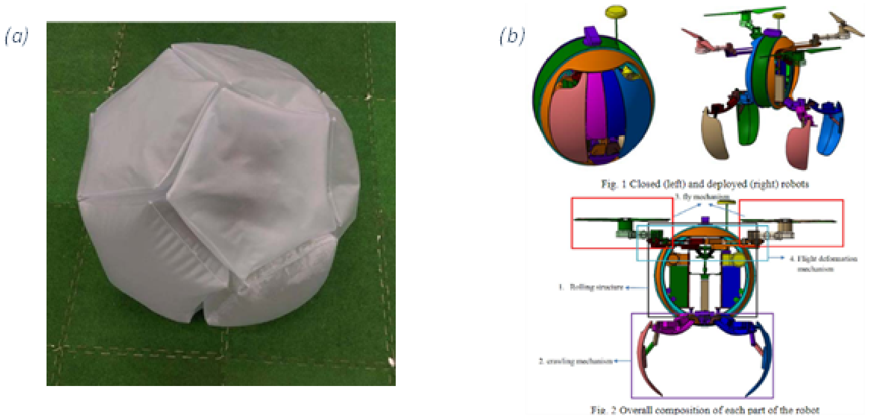

Figure 2.12: (a) Inflatable soft spherical robot. (b) Closed and deployed configuration of the robot by Zhang et al. [30].

2.2.3 Driving System Exploiting Angular Momentum

Some SR exploit the angular momentum conservation principle to enhance their movement capabilities. Two possible strategies are used: the control moment gyroscope (CMG), which consists in tilting a spinning rotor, and the reaction wheel (RW), which exploits the third Newton's law.

CMG: Control Moment Gyroscope

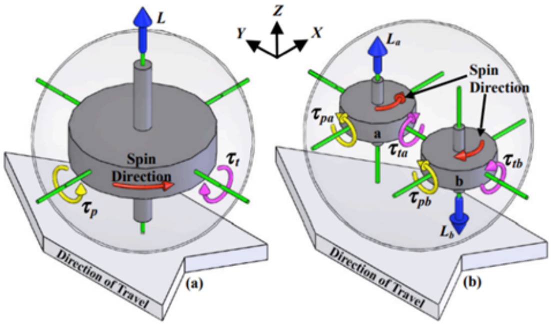

Figure 2.13: (a) Single and (b) dual CMG configurations. Image from [4].

Various SR using CMG can be found in literature. It relies on the same principle used in spacecraft attitude control systems. A CMG group consists of one or more spinning rotors that can be tilted through one or more motorized gimbals; the changing of the rotor spinning axes orientation causes a gyroscopic torque that can be used to accelerate or change the heading direction of the spherical robot. Usually, two counter rotating rotors are used, otherwise the tilting torque would cause an undesired motion of the sphere [4]. This driving mechanism is often together with another one (usually a gravity driving method).

In Figure 2.13 the single and dual CMG configurations are shown; in the case of the dual configuration, the resulting torque acting on the robot is the sum of the two gyroscopic torques τ_{pa} and τ_{pb}. The disposition of the rotors presented in Figure 2.13 can be used to accelerate the robot and overcome the limited torque provided by a barycenter offset driving system. The disposition shown in 2.14, instead, generates a net torque on the robot along the yaw axes, causing a change in the heading direction. A more in-depth analysis of how the gyroscopic torque works is presented in the next chapter.

An example of spherical robot with a CMG driving system is the one developed G. C. Schroll [4]. This robot exploits two actuating mechanisms: the pendulum driving strategy for forward and lateral movements and a CMG group to gain a greater torque to overcome steepest slopes and obstacles. The CMG group consists

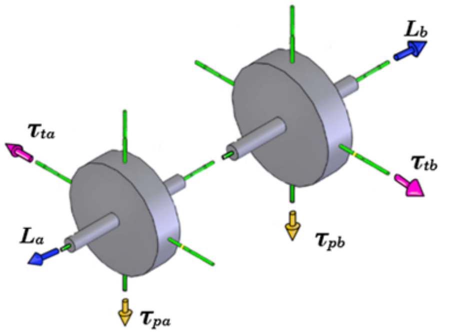

Figure 2.14: Dual CMG configuration to rotate the robot along the yaw axis.

of two rotors arranged as shown in Figure 2.13(a). It allows to solve the limited torque problem of the pendulum-driven robots. Moreover, it includes a stable platform for sensors to enhance the environmental perception. A similar example is the one developed by Chen et al. [2] (Figure 2.15(a)). Another example of spherical robot that uses a CMG group as driving system is the one proposed by Shu G. et al. [31] (Figure 2.15(a)). The model proposed (CNU-sphere robot, where CNU stands for Chungnam National University) is characterized by three actuators: two are used to actuate two wheels in contact with the inner surface of the spherical shell that provide the driving force; a CMG actuator is used to control the heading angle (yaw). The model has been realized on precedent studies performed on a disk-type robot.

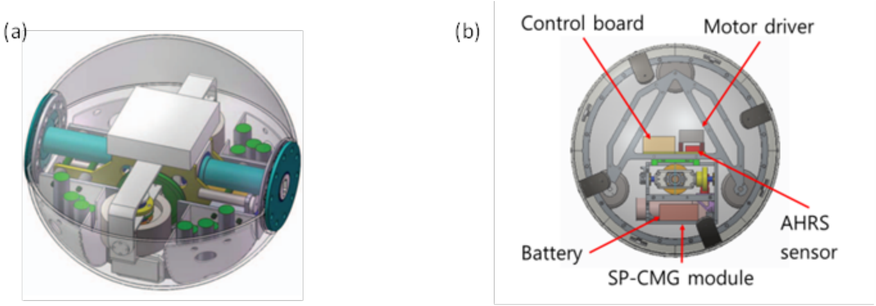

Figure 2.15: (a) Spherical robot using a CMG driving system to accelerate [2]. (b) Spherical robot using a CMG driving system to change the heading direction [31].

RW: Reaction Wheels

The RW (Reaction Wheels) is another driving method that exploits the spinning of a rotor. In this case, the driving principle is the third Newton's law. The rotor is a stationary flywheel and when a torque is applied to spin it, an opposite reaction torque will be generated, resulting in the opposite change of momentum of the sphere. A possible drawback of this system is the occurrence of an undesirable gyroscopic precession, which means that the flywheel must be stopped before changing the heading direction [4]. An example of RW driven spherical robot is L.U.N.A., a prototype that has been developed for the DEADALUS project [6] while studying the different possible locomotion strategies (Figure 2.16(b)). The prototype was discarded because of the too high-power consumption and the difficulties in controlling the mobile robot. Another example is the one developed by Jia Q. et al. [32] (Figure 2.16(a)). In this case, the flywheel has a double purpose: it's used like a pendulum for forward driving and for changing the heading direction, while a third motor is used to spin the rotor so that the angular momentum of the robot is increased. A Kalman Filter is used to estimate the robot pose through the information coming from IMU and motor drivers. Two more sensors are used to know the lean angles and spin rates of the flywheel.

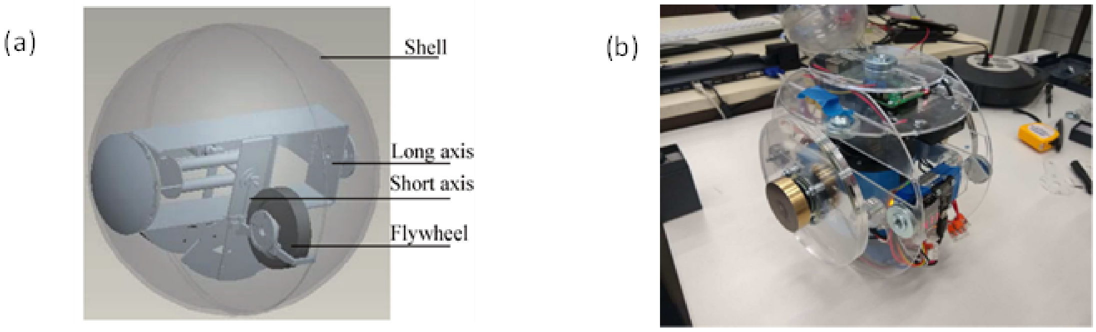

Figure 2.16: (a) The spherical robot developed by Jia Q. et al. [32]. (b) L.U.N.A. [11]

2.2.4 Differential Driving System

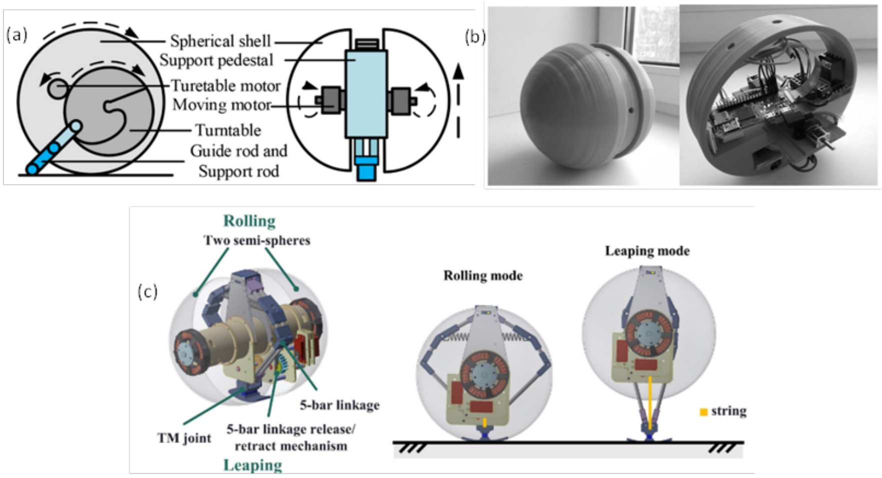

Figure 2.17: (a) Differential driving spherical mobile robot by Y. Dong et al. (b) One of the two prototypes developed by E. V. Potapov et al. (c) RolLeapO by Chang W. et al.

The differential driving system consists in a still central platform where two motors are placed to actuate the two hemispheres independently. The locomotion principle is the same of a hoverboard-Segway. The still central platform can be used for placing exteroceptive sensors, ensuring a more stable acquisition compared to spherical robots with other propulsion systems. Several spherical robots use the central platform for placing a hopping mechanism, to enhance the obstacle-crossing ability.

In 2020, E. V. Potapov et al. [33] realized two similar prototype of differential driven spherical mobile robots whose aim is to explore an indoor environment and recognize objects through computer vision algorithms. In the central platform are placed the batteries, the motors, the microprocessor and the camaras. The small motors used allow the prototypes to move at a constant speed of 0.26m/s (Figure 2.17(b)). Chang W. et al. [34] presented a model of spherical robot with a differential driving system and a five-bar linkage with a release/retract mechanism for leaping (Figure 2.17(c)). The combination of the spherical shape and a leaping-system allow this robot to navigate in both flat and extremely rough terrain. The choice of a differential driving system is due to the larger amount of available space inside the robot compared to other propulsion methods, necessary to store the leaping system. The robot was able to leap up a barrier of 14.5 cm, which is 1.14-times the radius of the robot. Y. Dong et al. [35] presented another example of spherical robot that can roll and jump, enhancing the robot mobility on rough terrain (Figure 2.17(a)). The robot structure consists of two hemispherical shell that can rotate independently. Between the two hemispherical shells, a support pedestal holds the two brushless motors and the hopping mechanism. The latter consists of a spring mechanism that stores elastic potential energy to release it when the robot needs to overcome an obstacle. The authors realized a prototype and the tests showed that it was able to jump up to 58 cm with a take-off angle of 60°.

2.2.5 Other Spherical Robots

There are few other examples of spherical mobile robot that can be found in the literature. Below, some spherical robot actuated by an internal drone, underwater spherical robots and wind-driven robots are presented.

SR Actuated by an Internal Drone

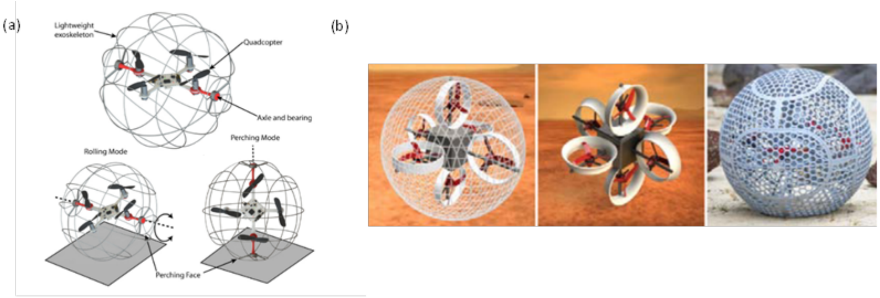

Figure 2.18: (a) Micro spherical rolling and flying robot by C. J. Dudley et al. [36], and (b) Rollcopter by S. Sabet et al. [37].

A novel type of driving system consists in placing a drone inside the spherical structure. This solution allows to exploit the flying capability to enhance the cross-obstacle ability, while protecting the drone with a spherical shell and exploiting the rolling movement for a less power consumption. The main drawback of this system is the complicated control system.

C. J. Dudley et al. [36] presented a prototype of micro spherical rolling and flying robot composed by a "micro-quadcopter encased in a lightweight spherical exoskeleton that can rotate about the quadcopter" (Figure 2.18(a)). The robot takes advantage of both the driving modes, resulting in a more versatile mobile robot which can easily overcome obstacles, navigate through narrow spaces, and exploit the rolling mode for travelling in a more efficient way compared to the flying-only robots. S. Sabet et al. [37] presented another example of flying and rolling spherical mobile robot named Rollcopter (Figure 2.18(b)). Like the other one, it combines the flying capability of a drone with the advantages of a spherical robot. It is based on six reversible propellers placed along three orthogonal axes; this placement allows the robot to fly at any attitude and to produce the torques needed to roll. The results obtained from the simulations show that "the required force for rolling is smaller than the flying forces" but "the advantage of rolling over flying decreases as the translational velocity or slope increases and the forces become equal when the slope is 90°" (which means vertical ascension).

SR For Underwater Applications

Some underwater spherical robots can be found in the literature. For example, a group of researchers from Manchester University (UK) developed two underwater spherical robots named MK-V and MK-VI, whose aim is to monitor nuclear storage tanks and sewage treatment equipment [38]. E. V. Potapov et al. [39] presented a model of spherical underwater robot (SUR IV) whose main characteristic is the possibility of both driving at high-speeds using the propeller thrusters and low-speeds through the water-jet thrusters.

Wind Driven SR

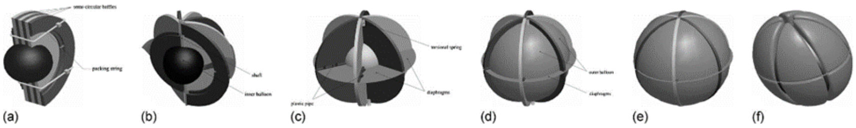

Figure 2.19: Different states of the spherical robot developed by Li T. and Liu W. [40]: (a) folded state; (b) process of deployment; (c) deployed state; (d) inflating process; (e) inflated state; and (f) floating state.

A last class of spherical robots that can be found in the literature is the wind-driven one. This type of mobile robot allows to explore special environments such as deserts, volcanos, polar regions, and the planetary surface. Their main advantages are their low cost, low power consumption, and the simple structure. However, their usage is limited by the atmospheric conditions because they require enough wind to navigate, and it's not possible to control the heading direction. An example of wind-driven spherical robot is the one developed by Li T. and Liu W. [40]. Its most important characteristic is its collapsible structure. It can switch from a folded state to an inflated state(Figure 2.19. It can travel through multiple movement modes: rolling, bouncing, and flying. Depending on the level of inflation it will be more inclined to navigate in a mode or another. Another example is the one presented by S. Xie et al. [8]. It also includes an internal pendulum to navigate also when there is no wind.

Chapter 3

Control Moment Gyroscopes

3.1 Introduction

When the gyroscope's spinning rotor is tilted, a gyroscopic torque perpendicular to the spinning and tilting directions is observed. This principle is at the basis of the Control Moment Gyroscope (CMG), an attitude control device that has been used in several space station, including the International Space Station. CMGs have been also used in some spherical robots (2.2.3) in order to increase the acceleration of the sphere, but they were never the main driving system of the robot.

The purpose of this chapter is to explore the potential applications of CMG groups in spherical robots. As discussed in the introduction section 1, the primary limitation of spherical robots is their limited ability to overcome obstacles. To address this challenge, the possibility of utilizing one or more CMG groups as a solution is examined. This chapter begins by providing a brief overview of the mathematical tools required to understand the concepts discussed. Next, the feasibility of implementing a gyroscope-only propulsion system to control the movements of a spherical robot is investigated. Specifically, the kinematics of a three-gimbal scissored pair CMG is analyzed, and a strategy to generate torque along any desired direction from any configuration is presented. Lastly, the potential use of CMG groups as an auxiliary driving system is evaluated, and the driving system that will be utilized in the prototype of the spherical robot is introduced.

3.2 The Gyroscopic Torque

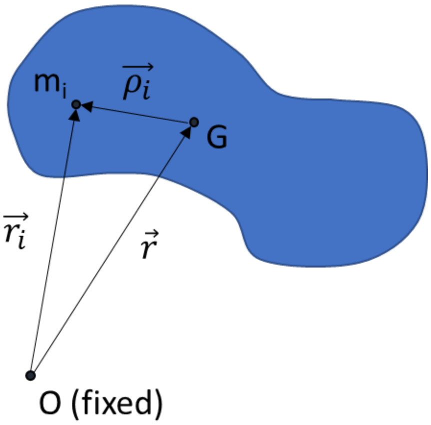

Figure 3.1

This section shows how to compute the gyroscopic torque generated by tilting a spinning rotor.

Consider the generic rigid body of figure 3.1. It is possible to obtain an equivalent equation to the Newton's second law for a rotating rigid body expressed with respect to its barycenter:

$$\sum \vec{M}_e G + \vec{M}_i G = 0$$

The total moment of all the forces acting on a system can be expressed also as:

$$\sum \vec{M}_{eG} = \frac{d\vec{K}_G}{dt}$$

Where $\vec{K}_G$ is the angular momentum (moment of momentum). $\vec{K}_G$ is usually expressed with respect to a reference frame (**RF**) fixed on the rigid body. If the RF is a principal axis system, the inertia tensor will have the form:

$$I = \begin{bmatrix} I_\lambda & 0 & 0 \\ 0 & I_\mu & 0 \\ 0 & 0 & I_\nu \end{bmatrix}$$

Then, the angular momentum will have the following equation:

$$\vec{K}_G = I_\lambda \omega_\lambda \vec{\lambda} + I_\mu \omega_\mu \vec{\mu} + I_\nu \omega_\nu \vec{\nu}$$

Substituting these results into the previous equation we obtain the formula that allows to compute the action of the inertia on the body:

$$\vec{M}_{iG} = -\frac{d\vec{K}_G}{dt} = -\left[\left(I_\lambda \dot{\omega}_\lambda \vec{\lambda} + I_\mu \dot{\omega}_\mu \vec{\mu} + I_\nu \dot{\omega}_\nu \vec{\nu}\right) + \left(I_\lambda \omega_\lambda \frac{d\vec{\lambda}}{dt} + I_\mu \omega_\mu \frac{d\vec{\mu}}{dt} + I_\nu \omega_\nu \frac{d\vec{\nu}}{dt}\right)\right] \tag{3.1}$$

The derivatives of the versors can be also expressed as:

$$\frac{d\vec{\lambda}}{dt} = \vec{\omega_T} \wedge \vec{\lambda} \qquad \frac{d\vec{\mu}}{dt} = \vec{\omega_T} \wedge \vec{\mu} \qquad \frac{d\vec{\nu}}{dt} = \vec{\omega_T} \wedge \vec{\nu}$$

Where $\vec{\omega_T}$ is the angular velocity of the reference system λ, μ, ν.

It's worth noting that this equation has been found considering the RF λ, μ, ν fixed to the rigid body, therefore their angular velocities are the same. However, when the body has a symmetry axis and rotates around it, the equation above remains valid even if the RF is not attached to the body. Hence, it can be used to compute the gyroscopic torque.

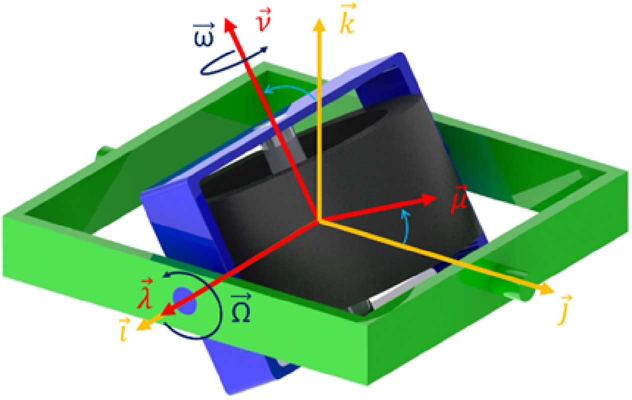

Figure 3.2: One gimbal gyroscope.

Consider now the one-gimbal gyroscope in Figure 3.2. The reference system in yellow (RS1) is fixed, while the red reference system (RS2) is attached to the blue gimbal. The two reference systems are centered at the barycenter of the gyroscope. The RS2 coincides with the RF (λ, μ, ν) used to compute the moment of inertial forces. The total angular velocity of the rotor is:

$$\vec{\omega}_{tot} = \Omega\vec{\lambda} + \omega\vec{\nu}$$

Therefore, the angular velocity components expressed in the mobile reference frame are:

$$\begin{cases} \omega_\lambda = \Omega \\ \omega_\mu = 0 \\ \omega_\nu = \omega \end{cases}$$

The derivative of the angular velocities and the versors are needed to obtain the equation 3.1 for the gyroscope. The angular velocities remain constant, so their derivative is zero; the versor derivatives are computed as follows:

$$\begin{cases} \frac{d\vec{\lambda}}{dt} & = & 0 \\ \\ \frac{d\vec{\mu}}{dt} & = & \Omega\ \vec{\nu} = \Omega \cdot \left[\cos\left(\theta(t)\right)\vec{k} - \sin(\theta(t))\vec{j}\right] \\ \\ \frac{d\vec{\nu}}{dt} & = & -\Omega\ \vec{\mu} = -\Omega \cdot \left[\cos\left(\theta(t)\right)\vec{j} + \sin(\theta(t))\vec{k}\right] \end{cases}$$

Where $\theta(t)$ is the tilting angle with respect to the axis $\vec{k}$ $(\theta\left(t\right) = \Omega \cdot t)$. Substituting these values inside equation 3.1 we obtain:

$$\vec{M}_{iG} = (I_\nu \omega \Omega) = \left[I_\nu \omega \Omega \cdot \left[\cos\theta(t)\vec{j} + \sin\theta(t)\vec{k}\right]\right] = I_\nu \vec{\omega} \wedge \vec{\Omega} \tag{3.2}$$

That is the equation describing the gyroscopic torque action.

3.3 CMG Only-Propelled Spherical Robot

3.3.1 One Scissored Pair CMGs

One important aspect emerges from equation 3.2: the direction of the gyroscopic torque (**GT**) moves with the gyroscope. Therefore, we must restrict the component acting along $\vec{k}$ if, for example, we only want to use the GT component acting along the $\vec{j}$ axis. Furthermore, the torque will not be constant, but its magnitude will follow a sinusoidal function (refer to equation 3.3).

Figure 3.3: CMG anchored to the ground.

As previously stated, a gyroscope used as a source of torque by tilting a spinning momentum wheel is known as Control Moment Gyroscope. In a CMG anchored to the ground, as the one shown in figure 3.3, the unwanted GT component would be canceled out by the reaction forces of the ground. The corresponding GT function is the following one:

$$\vec{M}_{iG} = (I_\nu \omega \Omega) \cdot \cos \Omega t \vec{j} \tag{3.3}$$

If a single one-gimballed-CMG is placed inside a spherical robot it would be necessary to counter the unwanted GT component in another way. A solution can be achieved using a second CMG which is tilted in such a way that the component along the direction of interest is maintained, while the other component is canceled out. When the gyroscopes are used in this configuration, they are also known as **scissored pair control moment gyroscopes**. Let's consider the gyroscope in figure 3.4. The red reference frame moves with the internal gimbal, and it's rotated around the $\vec{k}$ axis of the fixed reference frame about an angle equal to α_1. The

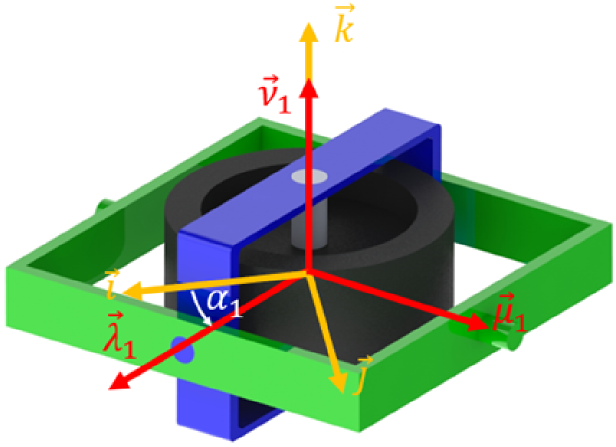

Figure 3.4

transformation matrix from the fixed to the mobile reference frame is the following one:

$$R_1^f(\theta(t)) = \begin{bmatrix} \cos\alpha_1 & -\sin\alpha_1 \cdot \cos(\theta_1(t)) & \sin\alpha_1 \cdot \sin(\theta_1(t)) \\ \sin\alpha_1 & \cos\alpha_1 \cdot \cos(\theta_1(t)) & -\cos\alpha_1 \cdot \sin(\theta_1(t)) \\ 0 & \sin(\theta_1(t)) & \cos(\theta_1(t)) \end{bmatrix} \tag{3.4}$$

Where $\theta(t)$ is the tilting angle with respect to the axis $\vec{k}$ The GT can be computed through the equation 3.2:

$$\vec{\tau}_G = I_\nu\, \vec{\omega} \wedge \vec{\Omega} = M \cdot [(-c_{\theta 1} s_{\alpha_1})\,\vec{i} \; + (c_{\theta_1} c_{\alpha_1})\,\vec{j} + s_{\theta_1}\vec{k}] \tag{3.5}$$

Where M is equal to $I_\nu \omega \Omega$. If we have an identical CMG inside the sphere with opposite ω and Ω, the value of M will be the same, while $\theta_2 = \theta_1 + \pi$. As a result, the components along the $\vec{i}$ and the $\vec{j}$ axis will be added, while the component along the $\vec{k}$ axis will be canceled out:

$$\begin{aligned} \vec{\tau}_{G_1} + \vec{\tau}_{G_2} &= M \left\{ (-c_{\theta_1} s_{\alpha_1})\,\vec{i} + (c_{\theta_1} c_{\alpha_1})\,\vec{j} + s_{\theta_1}\vec{k} + (-c_{\theta_2} s_{\alpha_2})\,\vec{i} + (c_{\theta_2} c_{\alpha_2})\,\vec{j} + s_{\theta_2}\vec{k} \right\} = \\ &= M \left\{ (-c_\theta s_{\alpha_1})\,\vec{i} + (c_\theta c_{\alpha_1})\,\vec{j} + s_\theta \vec{k} + (-c_\theta s_{\alpha_2})\,\vec{i} + (c_\theta c_{\alpha_2})\,\vec{j} + s_\theta \vec{k} \right\} = \\ &= M \left\{ (-s_{\alpha_1} + s_{\alpha_2})\,\vec{i} + (c_{\alpha_1} - c_{\alpha_2})\,\vec{j} \right\} c_\theta \end{aligned} \tag{3.6}$$

Four cases of interest can be found:

- $\alpha_1 = \alpha_2 + \pi$: $\quad \vec{\tau}_{tot} = M \cdot \left(2c_{\theta} s_{\alpha_2} \vec{i} - 2c_{\theta} c_{\alpha_2} \vec{j} \right)$
- $\alpha_1 = \frac{3}{2}\pi,\ \alpha_2 = \frac{\pi}{2}$: $\quad \vec{\tau}_{tot} = 2M\cos(\theta) \cdot \vec{i}$
- $\alpha_1 = 2\pi, \alpha_2 = \pi$ $\quad \vec{\tau}_{tot} = 2M\cos(\theta) \cdot \vec{j}$

- $\alpha_1 = \alpha_2$: $\vec{\tau}_{tot} = 0$

The first three cases describe the configuration with diametrically opposed gyroscopes. This is the most useful and the only possible configuration of a scissored pair of one-gimballed-CMGs inside a spherical robot; otherwise, the barycenter would be displaced from the center of the sphere, generating a moment due to the gravity force.

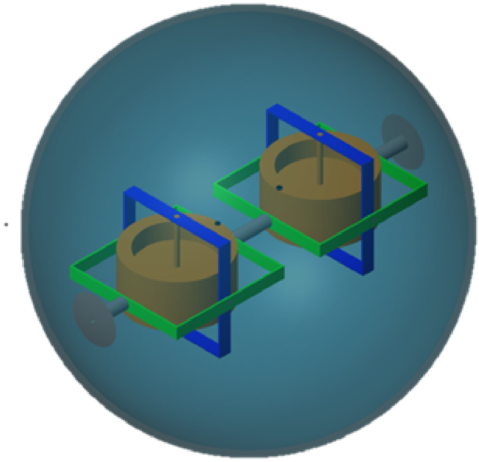

Figure 3.5: SR with two CMGs.

This configuration–two diametrically opposed one-gimballed gyroscopes–has two main limitations:

- The first one is that it allows to generate a torque along a unique direction. It can't be used to completely control the robot movements, but only the rolling of the sphere in one direction.
- The second one, as already highlighted at the beginning of this chapter, is that the torque has an oscillatory behavior due to the sinusoidal function that governs the equation.

Therefore, if the gyroscope is tilted at an angle greater than 90 degrees, a negative torque acts on the robot, decreasing its velocity; if no external forces are present, it stops when the tilting angle reaches 180 degrees. The same behavior can be observed when then gyroscope is tilted back to its original position.

This behavior is caused by the conservation of the angular momentum. When starting spinning the rotors in opposite directions, the total angular momentum of the system is equal to zero. When the gyroscopes are tilted, a torque acts on the sphere to compensate for the total angular momentum of the two gyroscopes, which is now different from zero. For this same reason, if the rotors are stopped after having been tilted, the sphere stops too.

Another way to analyze this behavior is the following. The CMGs can be thought as a propulsion system able to store a certain amount of angular momentum. It can be dispensed to the sphere, but when the whole momentum has been transferred, it is impossible to provide more torque. Eventually, the gyroscopes will need to be charged again, taking back the momentum provided and generating a negative torque that acts on the sphere.

3.3.2 Multiple Scissored Pair CMGs

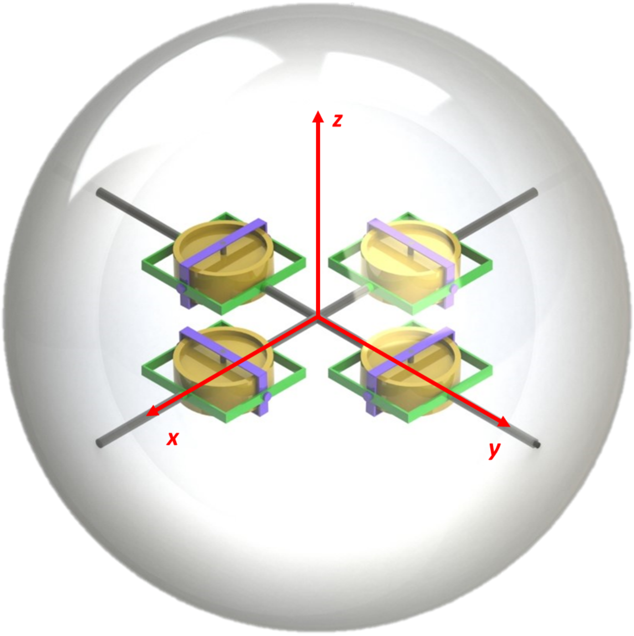

Figure 3.6: SR with 4 CMGs.

A second perpendicular couple of diametrically opposed gyroscopes could be added to overcome the first restriction of a single pair of one-gimballed CMGs (figure 3.6). In this manner, a torque could be generated in any direction in the plane containing the four gyroscopes. For example, if they are positioned along the X and Y axes of the spherical robot RF, the generated gyroscopic torques will be located on the X and Y axis respectively. Their magnitude will be described by the second and the third equations presented in the four cases of interest of the previous chapter. Therefore, tilting the two couple of CMGs with the same Ω and varying the spinning velocity ω, the resultant torque will be described by the equation:

$$\vec{\tau}_{tot} = 2I_\nu\Omega\omega_1 \cos{(\Omega \cdot t)} \cdot \vec{i} + 2I_\nu\Omega\omega_2 \cos{(\Omega \cdot t)} \cdot \vec{i}$$

$$|\vec{\tau}_{tot}| = 2I_\nu\Omega \ \sqrt{\omega_1^2 + \omega_2^2} \ \cdot \cos(\Omega \cdot t)$$

However, after the robot starts rolling, a new problem arises. The only way to change the heading direction consists in stopping in such a way that the plane containing the four gyroscopes will be horizontal. Otherwise, the torque generated when tilting again the rotors will have a vertical component, causing the sphere to follow a curved path. It is clear that, even with a perfect model of the robot, the disturbances coming from an uneven ground and external forces make impossible to control the sphere.

Therefore, a third couple of gyroscopes should be placed along the third axis of the sphere RF. In this manner, the gyroscopic torque could be directed along any direction, making possible to control the rolling motion from any orientation of the three pairs of CMGs. It must be noted that the same torque generated with two pairs of CMGs can be provided through a two-gimballed single pair. In the same way, the 6 gyros needed to control the robot rolling direction can be substituted by a pair of three-gimballed CMGs. This allows to reduce the space needed and the weight of the robot. In the following paragraphs, a scissored pair three-gimbals CMG inside a spherical robot is analyzed, presenting a possible motion strategy, and the kinematic of the system. Finally, the main problems of the system are presented.

3.3.3 Scissored Pair Three Gimballed CMG

In this section, a scissored pair three-gimbals CMG inside a spherical robot is analyzed. This configuration, as explained in the previous paragraphs, allows to generate a gyroscopic torque along any desired direction. Thanks to the 3 DOF-structure it is possible to completely control the orientation of the rotor. A reconfiguration of the three gimbal angles allows to tilt the gyroscope around any direction. Based on the considerations made in the previous chapter, a motion strategy was developed. Here the main steps are listed:

- Positioning of the tilting axis: knowing the desired heading direction of the sphere and the rotation of the sphere RS with respect to the fixed World RS, the motion of the two external joints (first and second gimbals) is computed in order to reposition the tilting axis.
- Spinning and tilting of the rotors: the rotors can start spinning in opposite directions; then, the internal gimbal (the third one) of the two gyroscopes is tilted in opposite directions and a gyroscopic torque is generated.

- Rolling at a constant velocity: the gyroscopes are tilted until the tilting angle reaches 90° As explained in the previous sections, going beyond 90° would generate a negative torque, which would stop the sphere. The sphere is now rolling with a constant velocity.
- Stopping the sphere: when the sphere has covered the desired distance or a change of direction is needed, the third gimbal can be tilted back to a 0° angle. This will generate a new gyroscopic torque in the opposite direction with respect to the previous one and, if no other external forces are present, it will cause the sphere to stop. Finally, the rotors are stopped.

After the fourth step, if the sphere hasn't reached the goal yet, the four points will be repeated. The biggest drawbacks of this strategy are the capability of moving only along straight paths and the need to stop the sphere every time it must change the heading direction.

In the next paragraphs, a more in-depth analysis of the first step is presented. The direct and inverse kinematics of a 3-gimbals gyroscope are needed in order to compute the angular displacement of the gimbals. The analysis is realized assuming that the robot is moving on a horizontal plane and that the angles of the gyroscope pose, and the orientation of the sphere RF are known.

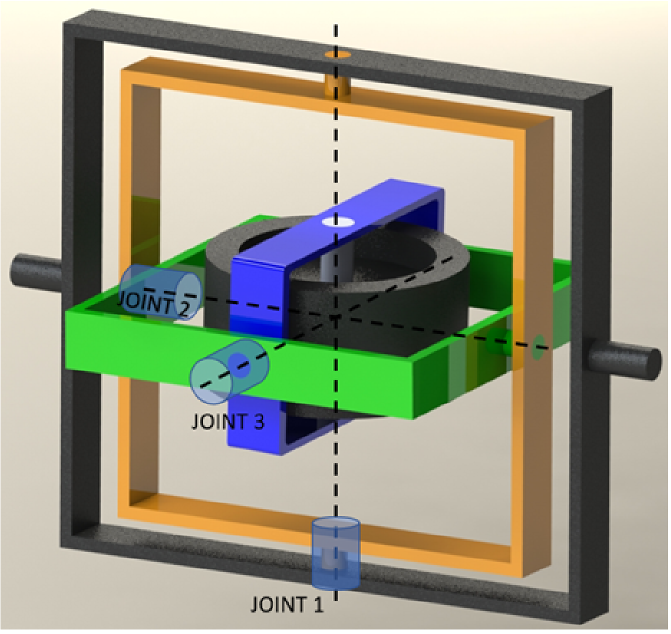

Figure 3.7: 3-gimbal gyroscope.

Positioning of the Tilting Axis: Direct Kinematics

To compute the direct kinematics (DK) of the gyroscope, the matrix of transformation between the sphere (RF0) and the third gimbal reference frame needs to be found: R_3^0.

In order to do that it is necessary to write all the transformation between every single consequential reference frame. Five reference frames can be defined: the ground reference frame (RFw), which is fixed, the sphere reference frame (RF0), which moves with the sphere, and the gimbals reference frames (RF1 – RF3). To develop the DK we are interested in the last four reference frames.

To develop the calculations, the Denavit Hartenberg (DH) convention has been used. A schematic diagram highlighting the joints and links of the device is shown in Figure 5. The Zero Reference Frame describes the sphere pose. Table 1 shows the DH parameters, which are used to describe the transformation between two consequential reference frames.

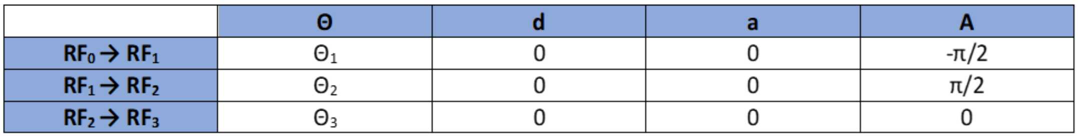

	Θ	**d**	**a**	**A**
$RF_0 \rightarrow RF_1$	Θ_1	0	0	-π/2
$RF_1 \rightarrow RF_2$	Θ_2	0	0	π/2
$RF_2 \rightarrow RF_3$	Θ_3	0	0	0

Figure 3.8: Denavit Hartenberg parameters of the three gimbals gyroscope.

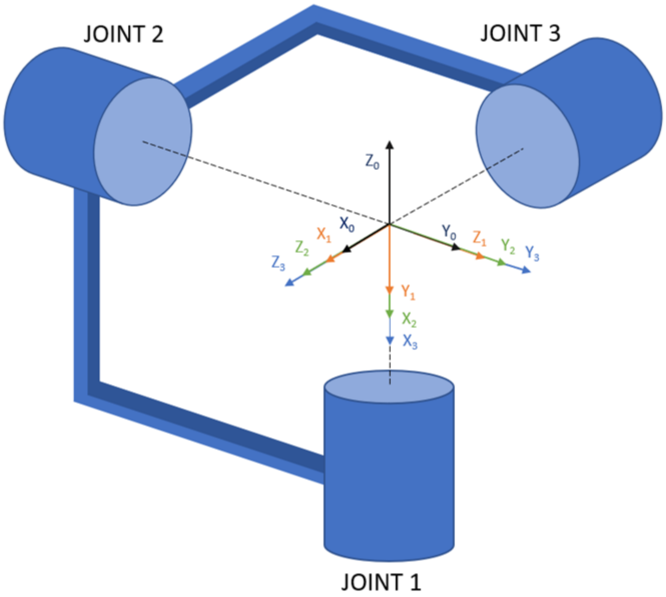

Figure 3.9: Schematic representation of the 3-gimbal gyroscope.

The transformation matrices between consequential reference frames can be obtained by substituting the DH parameters inside the following matrix:

$$A_i^{(i-1)}\left(q_i\right)=\begin{bmatrix} c_{\theta_i} & -s_{\theta_i}c_{\alpha_i} & s_{\theta_i}s_{\alpha_i} & a_i c_{\theta_i} \\ s_{\theta_i} & c_{\theta_i}c_{\alpha_i} & -c_{\theta_i}s_{\alpha_i} & a_i s_{\theta_i} \\ 0 & s_{\alpha_i} & c_{\alpha_i} & d_i \\ 0 & 0 & 0 & 1 \end{bmatrix} \tag{3.7}$$

In this case we have:

$$R_1^0\left(\theta_1\right)=\begin{bmatrix} c_{\theta_1} & 0 & -s_{\theta_1} \\ s_{\theta_1} & 0 & c_{\theta_i} \\ 0 & -1 & 0 \end{bmatrix} \quad R_2^1\left(\theta_2\right)=\begin{bmatrix} c_{\theta_2} & 0 & s_{\theta_2} \\ s_{\theta_2} & 0 & -c_{\theta_2} \\ 0 & 1 & 0 \end{bmatrix} \quad R_3^2\left(\theta_2\right)=\begin{bmatrix} c_{\theta_2} & -s_{\theta_1} & 0 \\ s_{\theta_2} & c_{\theta_i} & 0 \\ 0 & 0 & 1 \end{bmatrix}$$

Multiplying these three matrices we obtain the relation between the sphere and the third gimbal:

$$R_3^0\left(\theta_1,\ \theta_2,\theta_3\right)=\begin{bmatrix} c_1c_2c_3-s_1s_2 & -c_1c_2s_3-s_1c_3 & c_1s_2 \\ s_1c_2c_3+c_1s_3 & -s_1c_2s_3+c_1c_3 & s_1s_2 \\ -s_2c_3 & s_2s_3 & c_2 \end{bmatrix} = \begin{bmatrix} a_x^0 & b_x^0 & c_x^0 \\ a_y^0 & b_y^0 & c_y^0 \\ a_z^0 & b_z^0 & c_z^0 \end{bmatrix} \tag{3.8}$$

Positioning of the Tilting Axis: Inverse Kinematics

The matrix 3.8 can be used to compute the inverse kinematics, which are the equations of the joint angles associated with a specific pose of the third reference frame expressed in relation to RF0:

$$\begin{cases} \theta_1 = Atan2\left(c_y^0, c_x^0\right) \\ \\ \theta_2 = Atan2\left(\sqrt{\left(c_y^0\right)^2+\left(c_x^0\right)^2}\ , c_z^0\right) \\ \\ \theta_3 = Atan2\left(b_z^0, -a_z^0\right) \end{cases} \tag{3.9}$$

These angles correspond to the angular displacement of each one of the motors associated to the three gimbals. The next step consists in defining the new pose of RF3. The heading direction is known with respect to the RFw; the new pose of RF3 is defined aligning the tilting axis to the heading direction. Therefore, the transformation matrix from RFw to the new RF3 can be easily obtained. Finally, knowing the rotation matrix from RFw to RF0 (the orientation of the sphere reference system with respect to the fixed one after the robot movements), it is possible to define the rotation matrix $\widehat{R_3^0}$, which is the rotation matrix from the current sphere orientation to the new pose of the third reference system. The new angles $\widehat{\theta_1}$,$\widehat{\theta_2}$,$\widehat{\theta_3}$ can be computed through the inverse kinematics and can be subtracted to the current ones in order to obtain the needed gimbal movements. A more detailed explanation is presented in the next section.

Positioning of the Tilting Axis: Gimbals Input

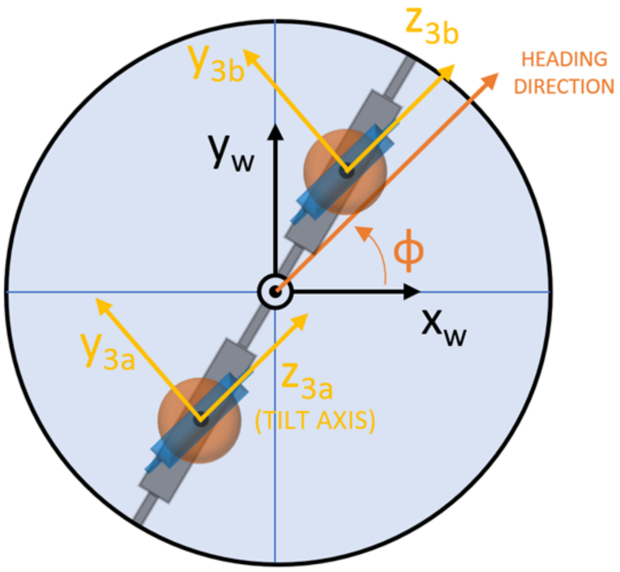

Figure 3.10: Top-view of the spherical robot. The heading direction and the new pose of RF3 are shown.

This section explains how to select the pose of the third gimbal reference frame when the sphere is moving on a horizontal plane. The choice of the RF3 pose can be done knowing that the tilting axis (axis z3 in Figure 3.9) has to be parallel to the heading direction, as shown in Figure 3.10, while the spinning axis (x3 in Figure 3.9) must be perpendicular to the ground. In this way, the torque generated by a single gyroscope will be parallel to y3. It should be noted that the spinning and tilting velocities are opposite in the two gyroscopes; as a result, the spinning and tilting directions of one gyroscope will be opposite to the positive directions of the reference frames. The transformation matrix from the world reference frame and the desired pose of $\widehat{R_3^w}$ will be:

$$\widehat{R_3^w} = \begin{bmatrix} 0 & -sin(\Phi) & cos(\Phi) \\ 0 & cos(\Phi) & sin(\Phi) \\ -1 & 0 & 0 \end{bmatrix} \tag{3.10}$$

Knowing the transformation between RFw and RF0 (R_0^w can be computed through the measurements of an IMU placed in the sphere's center), we can obtain the transformation matrix that relates RF0 with RF3.

$$\widehat{R_3^0} = R_w^0 \widehat{R_3^w} = \left(R_0^w\right)^{-1} \widehat{R_3^w} = \ \left(R_0^w\right)^{-1} \begin{bmatrix} 0 & -sin\left(\Phi\right) & cos\left(\Phi\right) \\ 0 & cos\left(\Phi\right) & sin\left(\Phi\right) \\ -1 & 0 & 0 \end{bmatrix} \tag{3.11}$$

Finally, using the equations 3.9, the joint angles $\widehat{\theta_1}$, $\widehat{\theta_2}$, $\widehat{\theta_3}$ required to achieve the desired position can be computed; subtracting from these the current ones, the angular displacement of each joint can be computed.

3.3.4 Problems of a CMG Only-Propelled SR

Effect of Dissipative Forces

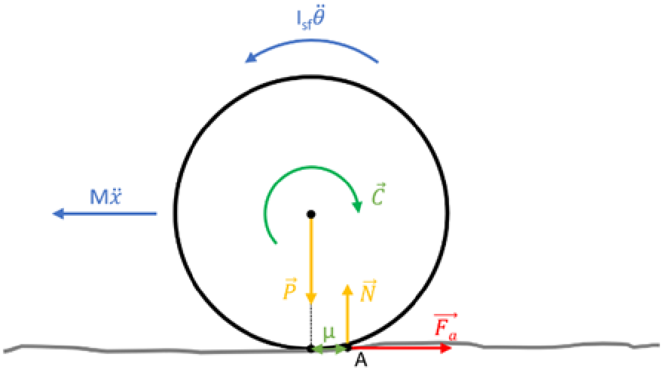

Figure 3.11: 2D scheme of a spherical robot moving on a flat surface.

The study that has been presented so far doesn't account for the impact of external forces on a CMG-only-propelled spherical robot. In this section, a qualitative analysis on the effect of dissipative forces is realized.

It will be shown that the effect of external dissipative forces can lead to undesirable behaviors. If we include, for example, the rolling friction, the total torque acting on the sphere when repositioning the spinning axis will be greater than the one that caused the sphere to accelerate. This means that the sphere will not only stop, but it will also start to roll in the opposite direction. An example is provided below for a more detailed explanation. The problem can be reduced to a 2D problem because the sphere is assumed to roll in a straight path.

Consider the spherical robot on a flat surface as in Figure 3.11. The two rotors are spinning in opposite directions at the same speed ω. At t = 0s, the third gimbal (the green one in figure 3.7) of the two gyroscopes starts moving in opposite directions with a constant velocity Ω until it reaches a 90° angle. This generates a gyroscopic torque $C(\phi)$ (ϕ is the tilting angle), causing the sphere to roll in a specific direction. While moving, the sphere experiences rolling friction with a friction coefficient μ. Its angular acceleration will be:

$$\ddot{\theta} = \frac{2I\omega\Omega\cos(\varphi) - Mg\mu}{MR^2 + I_{sf}}$$

Where I is the inertia of the rotors, M is the total mass of the robot, R is the radius of the robot and I_{sf} is the inertia of the sphere. By integrating the acceleration, we can obtain the speed attained by the robot at the end of the tilting motion:

$$\dot{\theta}\left(\frac{\pi}{2\Omega}\right) = \int_0^{\frac{\pi}{2\Omega}} \frac{2I\omega\Omega\cos(\Omega t) - Mg\mu}{MR^2 + I_{sf}} dt = \frac{2I\omega}{MR^2 + I_{sf}} - \frac{Mg\mu}{MR^2 + I_{sf}}\frac{\pi}{2\Omega}$$

When the tilt angle reaches 90°, we immediately begin tilting the gyroscopes back to 0°. The acceleration will be:

$$\ddot{\theta} = -\frac{2I\omega\Omega\cos(\varphi) + Mg\mu}{MR^2 + I_{sf}}$$

By integrating again the acceleration we obtain:

$$\dot{\theta}\left(t' + \frac{\pi}{2\Omega}\right) = \int -\frac{2I\omega\Omega\cos(\Omega t') + Mg\mu}{MR^2 + I_{sf}} dt' =$$
$$= -\frac{2I\omega}{MR^2 + I_{sf}}\sin(\Omega t') - \frac{Mg\mu}{MR^2 + I_{sf}} t' + K$$

Where $t' = t - \frac{\pi}{2\Omega}$, and K is the constant of integration. K can be computed by equating the value of velocity obtained from the previous calculus at $t' = 0s$:

$$\dot{\theta}(t') = \frac{2I\omega}{MR^2 + I_{sf}}(1 - \sin(\Omega t')) - \frac{Mg\mu}{MR^2 + I_{sf}}\ (t' + \frac{\pi}{2\Omega})$$

Substituting $t' = \frac{\pi}{2\Omega}$, we obtain the velocity attained by the sphere when the tilting angle is once again equal to 0°, which is negative:

$$\dot{\theta}\left(t' = \frac{\pi}{2\Omega}\right) = -\frac{Mg\mu}{MR^2 + I_{sf}}\ \frac{\pi}{\Omega}$$

Actually, the equation of the acceleration changes when the sphere stops, because the rolling friction changes its sign; however, the result obtained is sufficient to demonstrate that the robot stops before reaching a tilting angle of 0°. Therefore, robot will begin to move backwards. A possible solution to this problem would consist in repositioning the rotors with a Ω_1 smaller than the one used when accelerating the sphere. In this manner, the negative gyroscopic torque could be compensated by friction forces,avoiding the robot to start moving backwards.

Uphill Climbing

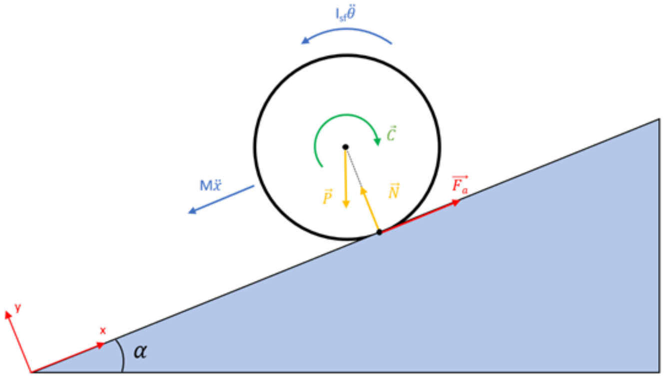

Figure 3.12: Free body diagram of a sphere rolling on a hill in a straight line.

The spherical robot's ability to ascend an inclined plane is a crucial feature. The CMG propulsion system, as explained so far, is able to provide only a limited amount of torque. If the robot is subjected to a constant negative acceleration, the sphere can only be accelerated in the positive direction until the gyroscopes reach the 90° tilting angle. As a result, if the sphere is climbing a slope, it can only be accelerated for a time equal to $\frac{\pi}{2\Omega}$ s. After this period, the gravity force is the only one applied on the robot (other external forces are neglected). If the robot doesn't reach the end of the slope before stopping, it will start rolling backwards. For a better understanding of this problem, an example with numerical data is presented. Consider a spherical robot equipped with a scissored-pair three gimballed CMG. The data are the following:

- $M <_{tot}= 16Kg$
- $M_{sf} = 3.5Kg$
- $R = 0.25\ m$
- $I_{sf} = 0.25\ Kg \cdot m^2$
- $m_g = 2\ Kg$
- $r_g = 0.04\ m$
- $I_g = I = 0.5\ m_g r_g^2 = 0.0016\ Kg \cdot m^2$

The free body diagram of the sphere is shown in Figure 3.12. The sphere starts going uphill at $t = 0s$, with an acceleration that depends on the torque generated by the inner CMG couple. The following equations can be obtained:

$$\begin{cases} Mgsin\left(\alpha\right) + M\ddot{x} = F_a \\ Mgcos\left(\alpha\right) = N \\ C - I_{sf}\ddot{\theta} - F_aR = \left[2I\omega\Omega\cos\left(\Omega \mathrm{t}\right)\right] - I_{sf}\ddot{\theta} - (Mgsin\left(\alpha\right) + M\ddot{x})R = 0 \end{cases} \tag{3.12}$$

Applying the pure rolling constraint: $\ddot{x} = \ddot{\theta}R$, the acceleration of the system will be:

$$\ddot{\theta}(t) = \frac{2I\omega\Omega\cos\left(\Omega t\right) - MgR\sin(\alpha)}{MR^2 + I_{sf}}$$

From this equation, rotational speed and displacement can be obtained:

$$\begin{aligned} \dot{\theta}\left(t\right) &= \int \frac{2I\omega\Omega\cos\left(\Omega t\right) - MgR\sin\left(\alpha\right)}{MR^2 + I_{sf}}dt \\ &= \frac{2I\omega}{MR^2 + I_{sf}}\sin\left(\Omega t\right) - \frac{MgR\sin\left(\alpha\right)}{MR^2 + I_{sf}}t + K_1 \end{aligned}$$

$$\begin{aligned} \theta\left(t\right) &= \int\left(\frac{2I\omega}{MR^2 + I_{sf}}\sin\left(\Omega t\right) - \frac{MgR\sin\left(\alpha\right)}{MR^2 + I_{sf}}t + K_1\right)dt = \\ &= -\frac{2I\omega}{\left(MR^2 + I_{sf}\right)\Omega}\cos\left(\Omega t\right) - \frac{MgR\sin\left(\alpha\right)}{MR^2 + I_{sf}}\frac{t^2}{2} + K_1t + K_2 \end{aligned}$$

Applying the zero initial conditions, the two constants of integration can be obtained:

$$K_1 = 0, \qquad k_2 = \frac{2I\omega}{\left(MR^2 + I_{sf}\right)\Omega}$$

Therefore, the speed and the angular displacement of the sphere while tilting the gyroscopes will be described by the following equations:

$$\dot{\theta}\left(t\right) = \frac{2I\omega}{MR^2 + I_{sf}}\sin\left(\Omega t\right) - \frac{MgR\sin\left(\alpha\right)}{MR^2 + I_{sf}}t$$

$$\theta\left(t\right) = -\frac{2I\omega}{\left(MR^2 + I_{sf}\right)\Omega}\cos\left(\Omega t\right) - \frac{MgR\sin\left(\alpha\right)}{MR^2 + I_{sf}}\frac{t^2}{2} + \frac{2I\omega}{\left(MR^2 + I_{sf}\right)\Omega}$$

When the gyroscope reaches a 90° tilting angle, the gyroscopic torque goes to zero; therefore the only acceleration acting on the robot is the one due to the gravity force:

$$\ddot{\theta}(t) = \frac{-MgR\sin(\alpha)}{MR^2 + I_{sf}}$$

The speed can be described by the following equation:

$$\dot{\theta}\left(t'\right) = \left(\frac{2I\omega}{MR^2 + I_{sf}}\right) - \frac{MgR\sin\left(\alpha\right)}{MR^2 + I_{sf}}\left(t' + \frac{\pi}{2\Omega}\right)$$

Where $t' = t - \frac{\pi}{2\Omega}$. The angular displacement can be obtained by integration of the angular speed:

$$\theta\left(t'\right) = \left(\frac{2I\omega}{MR^2 + I_{sf}}\right)t' - \frac{MgR\sin\left(\alpha\right)}{MR^2 + I_{sf}}\left(t' + \frac{\pi}{\Omega}\right)\frac{t'}{2} + \\ +(-\frac{MgR\sin\left(\alpha\right)}{MR^2 + I_{sf}}\frac{\left(\frac{\pi}{2\Omega}\right)^2}{2} + \frac{2I\omega}{\left(MR^2 + I_{sf}\right)\Omega})$$

It is possible to plot these functions substituting the data listed above. The obtained graphs are the following:

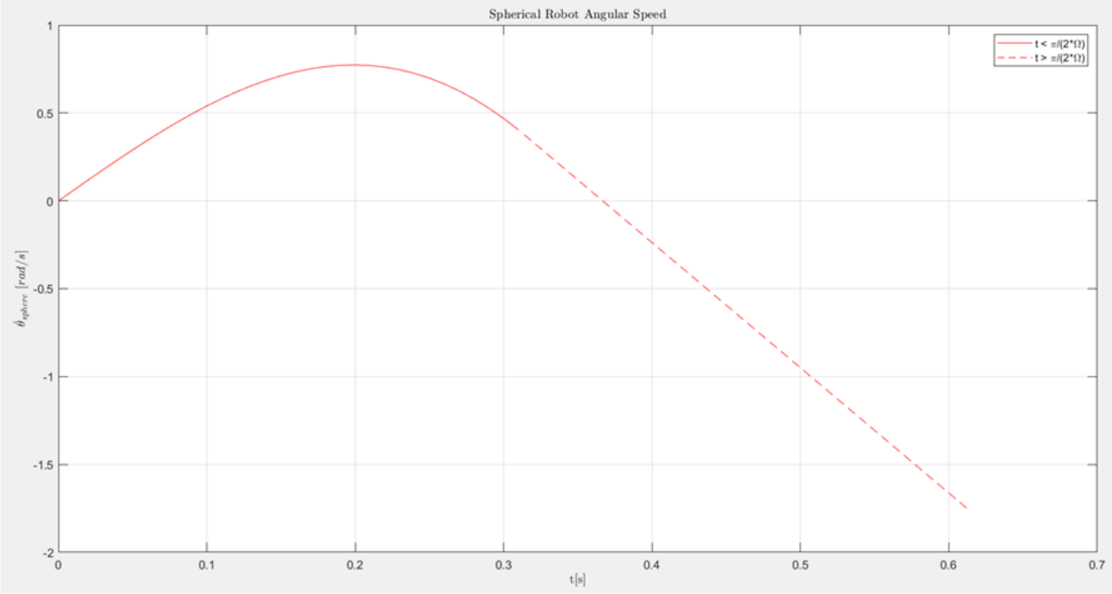

Figure 3.13: Spherical Robot Angular Speed.

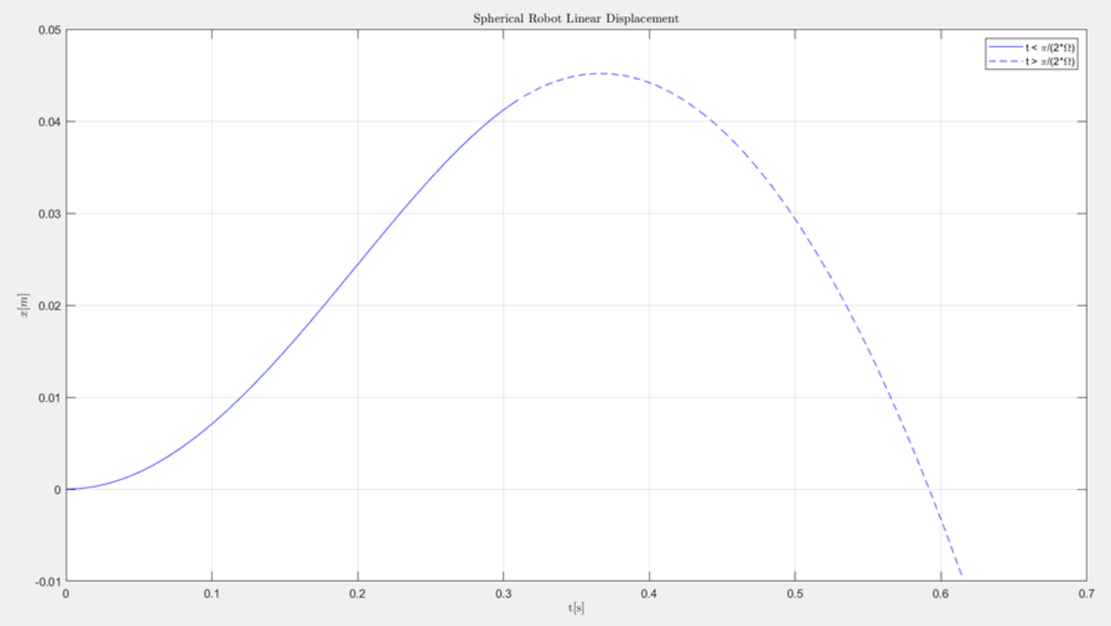

Figure 3.14: Spherical Robot Linear Displacement.

As expected, the robot is able to climb the slope as long as the acceleration due to the gyroscopic torque is greater than the negative acceleration due to gravity. Then, the robot starts to decelerate, and it will eventually reach the starting point, indicating a clear limitation of the system. For this reason, the CMG is usually applied as an auxiliary propulsion system. With the help of a primary propulsion system (such as a BCO), the CMGs can be "recharged" without affecting the robot motion. In the next chapter, the use of a scissored pair as an auxiliary propulsion system is studied, and the driving system that will be used on the spherical robot prototype is presented.

Another approach to overcome this limitation would be to change the shape of the shell. A polyhedral structure, rather than a spherical one, could remain stationary on a slope without requiring a positive torque. It would also allow for a slow recharge of the CMGs: the tilting velocity could be selected to generate a small negative torque that would not be sufficient to tip the robot over.

3.4 CMG as an Auxiliary Driving System

In the previous paragraphs, the use of the CMG as primary driving system of a SR has been studied. The problems with this type of system have been discussed, and it has been concluded that a gyroscope-only driving system can't be realized. This doesn't mean that a CMG group can't be used inside a SR, but that it must be associated with a primary driving unit, such as a pendulum or a hamster ball driving system. Thus, it can serve as an auxiliary driving system to stabilize or boost the robot.

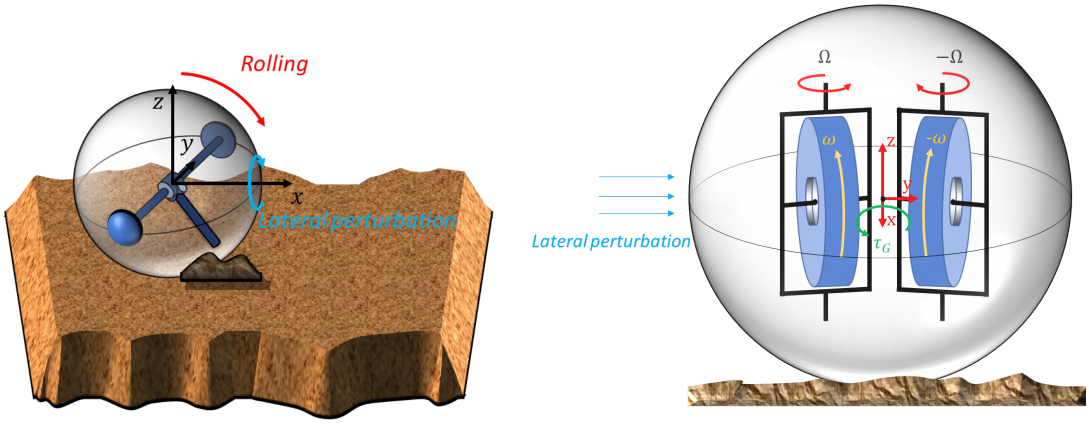

(a) (b)

Figure 3.15: (a) Diagram of the spherical robot encountering an obstacle. (b) CMG group disposition for stabilizing the robot against lateral oscillations (front view).

The first option employs a scissored pair CMG group to stabilize the robot against lateral oscillations. If the sphere is travelling on an uneven terrain, small obstacles could be met along the path (3.15(a)). Consequently, reaction forces acting on a different direction from the heading one may cause the sphere to start oscillating. The twin gyroscopes could be used as shown in fig. 3.15(b): the two rotors spinning in opposite directions are tilted around the z-axis to generate a gyroscopic torque around the x-axis. They could be placed on the pendulum of a pendulum-driven SR. It is important to note that the system's z-axis must always be perpendicular to the ground; otherwise, the CMGs would act on both the roll and yaw axes of the sphere. Therefore, an external gimbal controlling the attitude of the CMG's YZ plane is needed.

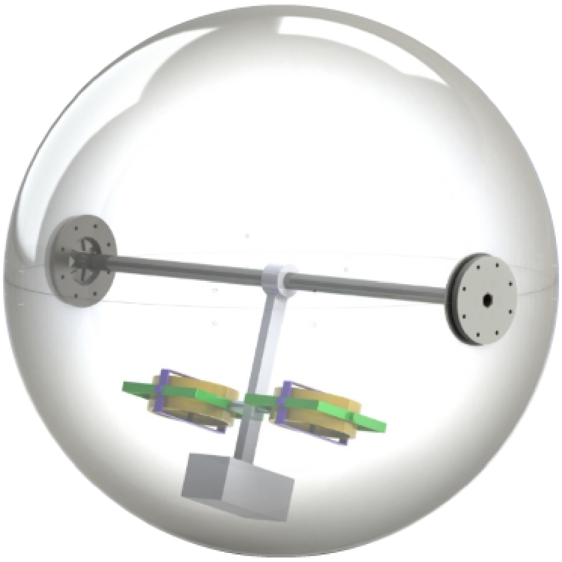

Figure 3.16: Conceptual Design of a SR with a CMG used to provide a temporary boost.

The second option consists of two CMGs used to give a temporary boost to the robot in the forward direction. Consider a SR whose main propulsion system consists of a 2 DoF pendulum. The CMG can be attached to the pendulum to generate a gyroscopic torque that opposes the pendulum's movement when needed (a conceptual representation is shown in figure 3.16). This effect can be seen as a temporary increase in the weight of the pendulum, requiring more torque to lift and resulting in a higher reaction torque on the sphere. This boost can be utilized to enhance the robot's ability to overcome obstacles.

As already explained in the introduction, one of the main disadvantages of the SRs is their limited obstacle climbing performance. For this reason, the aim of this thesis is to present a pendulum driven SR with a CMG group used to increase the available torque. A more detailed explanation is presented in the next paragraph.

3.4.1 CMG to Enhance Obstacle Climbing Capability

The CMG group configuration used inside the sphere is the same that was studied in paragraph 3.3.1: two one-gimballed gyroscopes spinning and tilting in opposite directions. An illustration of the front view of the SR is shown in fig. 3.17. It can be observed that the gyroscopic torque components along the y-axis cancel out, leaving only the ones along the x-axis. The gyroscopic torque must act against the upward movement of the pendulum. A simple free body diagram studying the static equilibrium of the sphere facing a step is shown in fig. 3.18. The problem can be split into two. The analysis of the forces acting on the pendulum (fig. 3.18(a)),

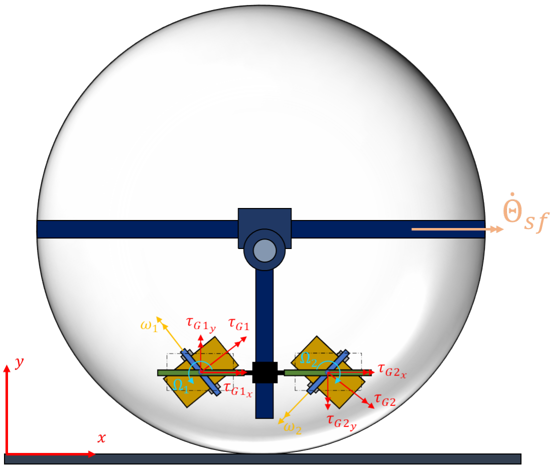

Figure 3.17: Front view of a SR equipped with a CMG group, highlighting the details of the gyroscopic torque action.

and the ones acting on the sphere (fig. 3.18(b)). The equations obtained are as follows:

$$\begin{cases} \tau_M & = & L \cdot m_p g + \tau_G \\ V & = & m_p g \\ b & = & R \cdot \sqrt{1 - (1 - \frac{h}{R})^2} \\ a & = & (L \cdot m_p)/(m_p + M_s) \\ \tau_M & = & b(V + M_s g) \end{cases}$$

Rearranging these equations, it is possible to recalculate the MSH-over-radius curve 1.2 while including the effect of the gyroscopic torque:

$$\frac{h}{R} = 1 - \sqrt{1 - \left(\frac{a + \frac{\tau_G}{(m_p + M_s)g}}{R} \right)^2} \tag{3.13}$$

It can be observed that the barycenter of the sphere is increased by a factor which depends on the gyroscopic torque and the total mass of the system. Therefore, it

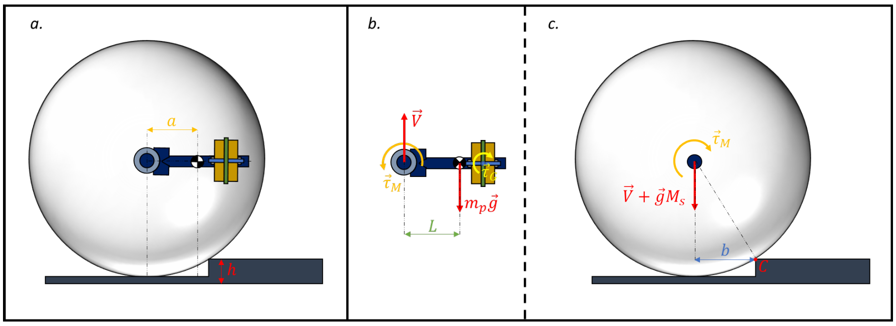

Figure 3.18: Free Body Diagram of the robot while climbing a step (static equilibrium condition).

is possible to define a new variable a^* that is computed as:

$$a^* = a + \frac{\tau_G}{(m_p + M_s)g} \tag{3.14}$$

Substituting this variable inside 3.15, it results:

$$\frac{h}{R} = 1 - \sqrt{1 - \left(\frac{a^*}{R}\right)^2} \tag{3.15}$$

which is the same relation expressed by eq. 1.2. To understand how the maximum step height can vary with the aid of the gyroscopic torque, the relation between

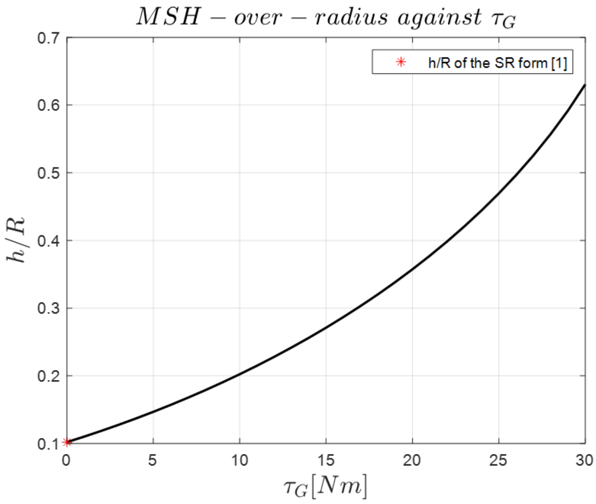

Figure 3.19: MSH-over-radius curve against Maximum Gyroscopic Torque. Total mass and barycenter position of the robot from [1].

the step over radius and the maximum gyroscopic torque expressed by eq. 3.15 is represented in fig. 3.19. To plot the curve, the values of the SR from [1] were used. It can be observed that if the gyroscopes aren't used, the step height is one tenth of the radius, which was the MSH of the SR from [1].

Note that the gyroscopic torque is not constant, therefore, while tilting the gyroscopes the value of a^* will decrease until it returns to be equal to a. However, the torque needed to overcome a step decreases while climbing it, therefore it was considered sufficient to refer to the the maximum gyroscopic torque to asses the MSH that the robot was able to climb.

Finally, observe that the value of a^* doesn't depend only on the gyroscopic torque, but also on the total mass of the system.

In the next chapter, the design process of the robot is presented, which was carried out trying to maximize the MSH parameter, while respecting the other constraints.

Chapter 4

Design Process

In this chapter, the design process of the robot is presented. The first paragraph describes the design of the SR by M. Melchiorre et al. [1]. The subsequent sections discuss the new design, highlighting the CMG group, the dimensioning of the main motors, and the pendulum structure design. Finally, the chapter concludes by presenting the final design of the robot.

4.1 Previous Work

This Section presents the SR that was developed by M. Melchiorre et al. [1]. As previously stated, this SR uses a BCO propulsion system consisting of a 2 DOF pendulum. Unlike traditional designs, the pendulum actuators are not attached to the central shaft. Instead, they have been placed at the bottom of the pendulum structure to lower the robot barycenter. Motion is transferred to a differential driving system located at the center of the shaft through two transmission belts. This differential driving system is similar to the one used in cars and is composed of one planet gear that is attached to the central shaft and two sun gears that are connected to the motors through the timing belts (fig. 4.2 (a)). The angular speed of the main shaft can be related to the speed of the sun gears and the pendulum through two cinematic relation. Consider the fig. 4.1: let's define an x and y axis passing through the sun gear centers, and the central shaft respectively. It is possible to obtain the following equations:

$$\omega_3 = \frac{\omega_1 - \omega_2}{2} - \omega_p \tag{4.1}$$

$$\Omega = \frac{\omega_1 + \omega_2}{2} - \Omega_p \tag{4.2}$$

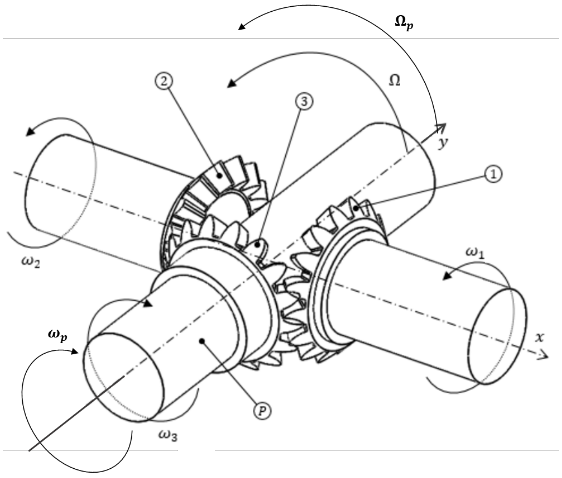

Figure 4.1: Differential gear used on the SR by [1].

Where ω_1 and ω_2 are the velocity of the sun gears around the x axis, ω_3 and ω_p are the sphere and pendulum velocity around the y axis, and Ω and Ω_p are the main shaft and pendulum angular speeds around the x axis.

The spherical shell consists of two layers, namely the inner layer made of harmonic steel sheets bent to assume a spherical shape and the outer layer made of impermeable rubber. The combined mass of the spherical shell and the differential mechanism was approximately 5.7 kg. This value was used to determine the pendulum mass and the barycenter distance form the sphere center.

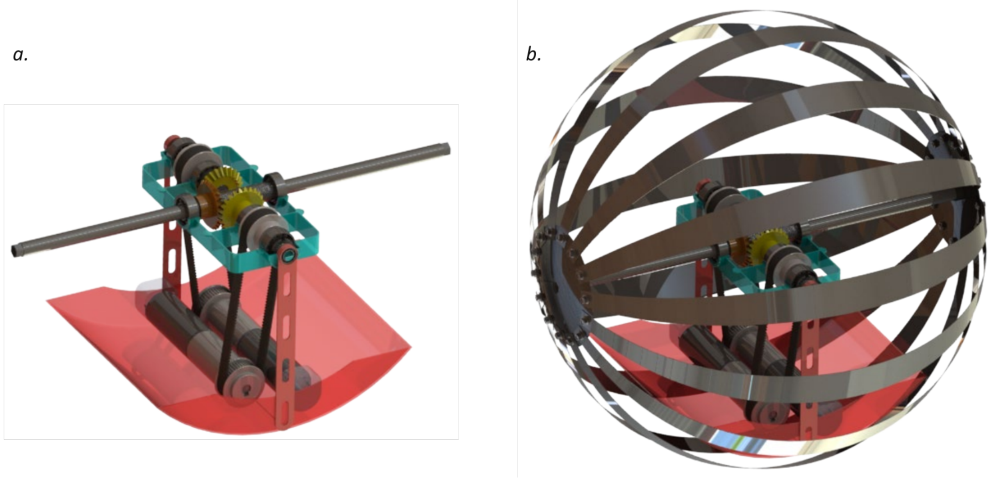

Figure 4.2: (a) Driving mechanism and pendulum. (b) Assembly of the SR. Images from [1].

4.2 New Project

4.2.1 Design of the CMG Group

In the following paragraphs, the design of the components of the CMG group is presented. The discussion begins with the dimensioning of the flywheel, highlighting the procedure that was followed to define its size based on the design specifications. This is followed by the presentation of the selection process for the spinning motors. Finally, the gyroscope design is shown.

Flywheel Dimensioning

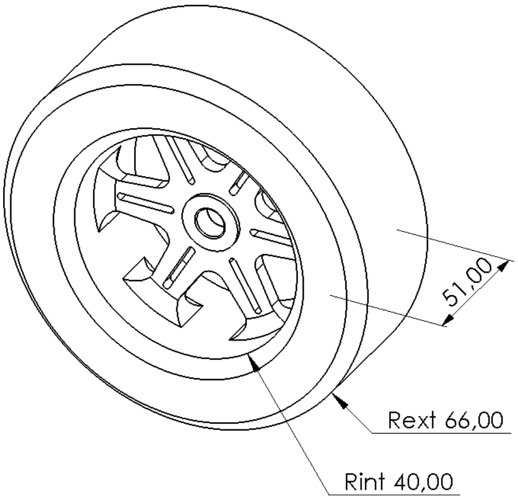

Figure 4.3: Drawing of the flywheel. Measures from CAD.

As already stated in section 1.1, the design of the gyroscope has been realized in order to improve the MSH performance parameter. The relation described by eq. 3.13 was used to compute eq. 4.3. The maximum gyroscopic torque was then used to compute the size of the flywheel.

$$\tau_{G,MAX} = \left(\sqrt{R^2 - 2Rh} - a\right) g M_{tot} \tag{4.3}$$

To compute the maximum gyroscopic torque some values had to be fixed: the step height, the radius of the robot, the barycenter position, and the total mass of the system. The MSH value was chosen to be 10% greater than the one of table 1.2: MSH $= 110$ mm. The spherical radius and the barycenter position were computed from the design specifications: $R = 250$ mm and $a = R \cdot sin(\varphi) \approx 87.5mm$. The effect of the system mass on the gyroscopic torque was then studied. As explained in the previous chapter, reducing the weight of the system leads to a decrease in the required gyroscopic torque. Multiple options were examined, and it was determined that the minimum achievable weight was $22kg$. The pendulum accounted for 16 kg of the weight, while the sphere and differential mechanism weighed a combined 6 kg. The resulting maximum gyroscopic torque was equal to: $\tau_{G,MAX} = 25.82\ N \cdot m$.

This value was then used to compute the inertia of the gyroscope flywheel. It can be obtained from equation 3.3 imposing $t = 0s$.The spinning and tilting velocities were taken equal to $\omega = 8000\ rpm$ and $\Omega = 15\ rpm$ respectively. The flywheel inertia resulted to be: $I = 0.0098\ kg \cdot m^2$.

An approximation was made for the shape of the flywheel, assuming it to be a hollow cylinder. Thanks to this assumption, two equations can be used to compute its size:

$$I_{fl} = 0.5 \cdot m_{fl} \left(r_{ext}^2 + r_{int}^2 \right) \tag{4.4}$$

$$m_{fl} = \rho \pi h_{fl} \left(r_{ext}^2 - r_{int}^2 \right) \tag{4.5}$$

The mass of the flywheel was fixed to $m_{fl} = 3.2\ kg$. This two equations are not sufficient to compute the three variables defining the size of the flywheel: external and internal radius, and its thickness. A first solution can be achieved by fixing one of the three variables, but this result doesn't guarantee an optimal use of the internal space. Therefore a non-linear optimization problem aiming at reducing the overall dimensions of the flywheel was solved. The variables of the problem are: $x_1 = R_{int},\ x_2 = (R_{ext} - R_{int}),\ x_3 = h$. The distance from the edge of the cylinder and its center was selected as auxiliary function to minimize:

$$f\left(x_1, x_2, x_3\right) = \sqrt{\left(x_1 + x_2\right)^2 + \frac{x_3^2}{4}} \tag{4.6}$$

The equations 4.5 and 4.4 can be used to obtain the two nonlinear equality constraints of the problem:

$$0.5 \cdot m_{fl} \left(x_1^2 + \left(x_1 + x_2\right)^2 \right) - I_{fl} = 0 \tag{4.7}$$

$$\rho \pi x_3 \left(\left(x_1 + x_2\right)^2 - x_1^2 \right) - m_{fl} = 0 \tag{4.8}$$

Finally, a linear inequality constraint can be defined, which limits the external radius to 70 mm:

$$x_1 + x_2 \leq 0.07 \tag{4.9}$$

The sizes of the flywheel obtained by solving this problem are listed in the first column of table 4.1. When designing the flywheel on Solidworks, these values were used as a reference but they were slightly changed due to the approximation made at the beginning of the problem considering the flywheel as a hollow cylinder.

	Theory	Real
m_{fl}	3.2 kg	3.35 kg
I_{fl}	$9.75 \cdot 10^{-3} kg \cdot m^2$	$9.8 \cdot 10^{-3}\ kg \cdot m^2$
R_{ext}	66 mm	66 mm
R_{int}	42 mm	40 mm
h	51	51 mm

Table 4.1: Sizes of the flywheel.

Drag Forces on a High-Speed Spinning Flywheel

To dimension the motors responsible for the flywheel spinning motion, it was crucial to assess the potential sources of loss in a high-speed spinning rotor. More specifically, a comprehensive analysis of the air resistance acting on the flywheel's surface was conducted.

The main factor responsible for an increase of the drag are the surface area of the flywheel, speed, and viscosity of the medium surrounding the disk. The viscosity of a fluid increases with the pressure, therefore, the most common solution adapted to minimize the drag moment consists of placing the flywheel inside a housing and reduce the inner pressure through a vacuum pump. Because this solution cannot be implemented inside the spherical rover, it is critical to quantify the drag torque acting on the rotor.

For this reason, several analytical models from the literature are introduced and subsequently applied to the present scenario. The objective is not to perform an exhaustive theoretical investigation, but rather to estimate the impact of air friction, allowing for its consideration during the selection of the spinning motors.

A first theoretical model is the one developed by Von Karman and Cochran, which allow to compute the drag moment on a disk rotating in the free space. The drag moment is caused by the flow on the disk plates, while the drag on the edges

$C_M = 3{,}87\ Re^{-\frac{1}{2}}$	$Re < 5 \cdot 10^4$
$C_M = 0{,}146\ Re^{-\frac{1}{5}}$	$Re \geq 5 \cdot 10^4$

Table 4.2: Moment coefficient equations used in equation 4.10.

was considered to be negligible because of the thin thickness of the used disk. The moment is described through a dimensionless parameter called moment coefficient C_M and the equation of the drag acting on one face is:

$$M = C_M \ \rho_a \ \omega^2 R^5 \cdot 0{,}5 \tag{4.10}$$

where ρ_a is the air friction, ω is the spinning velocity of the disk, and R is the disk radius. The moment coefficients depend on the Reynolds number, which is a dimensionless parameter that is used to describe the behavior of the flow (laminar or turbulent). Von Karman and Cochran obtained two possible empirical equation describing the C_M that can be read in table 4.2. The Reynolds number is computed through equation 4.11:

$$Re = \frac{\rho_a \ \omega \ R^2}{\mu} \tag{4.11}$$

where μ is the dynamic viscosity of the air.

In the case of a flywheel, the thickness can't be considered to be thin; therefore it is necessary to account for the drag moment acting on the lateral surfaces. A solution is presented in [41]: the moment coefficient must be corrected as shown in equation 4.12:

$$C'_M = C_M \cdot \frac{R + \frac{5}{2}l}{R} \tag{4.12}$$

where l is the thickness of the rotor.

When considering a flywheel placed inside an enclosure, other models have been developed. J. Abrahamsson et al. [42] analyzed the drag losses approximating the flywheel as a disc enclosed in a cylindrical container (figure 4.4). They consider an annulus with outer radius r_2 (radius of the disk) and inner radius r_1 (the shaft radius). The drag moment is considered to act only on the two flat faces of the annulus.

The moment acting on the disk (both surfaces) can be computed through

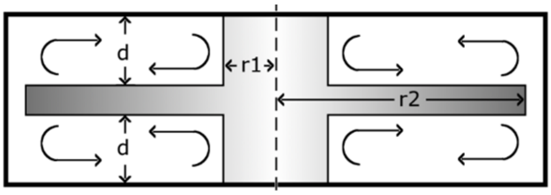

Figure 4.4: Schematic picture of a disc rotating inside a cylindrical enclosure. Image from [42]

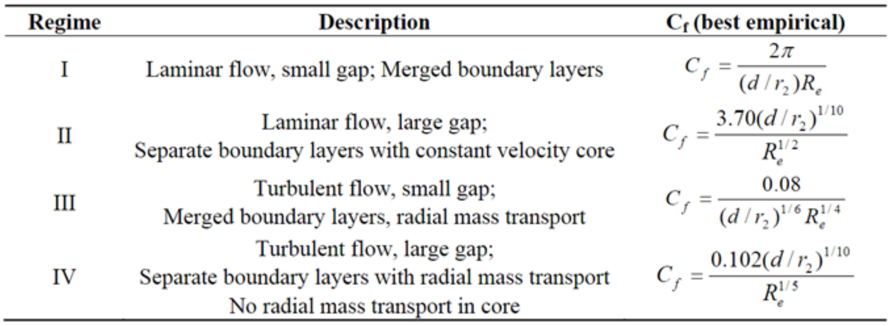

Regime	Description	C_f (best empirical)
I	Laminar flow, small gap; Merged boundary layers	$C_f = \frac{2\pi}{(d/r_2)R_e}$
II	Laminar flow, large gap; Separate boundary layers with constant velocity core	$C_f = \frac{3.70(d/r_2)^{1/10}}{R_e^{1/2}}$
III	Turbulent flow, small gap; Merged boundary layers, radial mass transport	$C_f = \frac{0.08}{(d/r_2)^{1/6} R_e^{1/4}}$
IV	Turbulent flow, large gap; Separate boundary layers with radial mass transport No radial mass transport in core	$C_f = \frac{0.102(d/r_2)^{1/10}}{R_e^{1/5}}$

Figure 4.5: Overview of the possible flow configurations that may occur when a disc rotates inside a cylindrical enclosure. The Reynolds number can be computed through equation 4.11. Image from [42].

equation 4.13:

$$M = C_M \; \rho_a \; \omega^2 \; \left(r_2^5 - r_1^5\right) \cdot 0{,}5 \tag{4.13}$$

Here, the moment coefficient is computed through four different empirical equations, each one referring to a specific air flow regime (figure 4.5). The flow regimes depend on the ratio between the gap and the outer disk radius ($G = \frac{d}{r_2}$), and on the Reynolds number, as shown in figure 4.6.

This model is one of the most used to estimate the drag moment acting on the flywheel. However, it was developed for a thin disk rotating inside an enclosure, and it doesn't consider the losses due to the friction acting on the edge (cylindrical surface).

Another model used to compute the drag acting on a spinning flywheel placed inside an enclosure is presented by Antonello S. S. et al. [43]. They considered the overall drag moment as the result of two contributions:

- An axial contribution, due to the air flow between the case and rotor cylindrical surfaces (the annulus gap);
- A transversal contribution.

The flow inside the annulus gap is laminar at low angular speeds; when the spinning velocity exceeds a critical value, the flow becomes unstable and the so-called Taylor vortices appear. These are due the centrifugal forces acting on the fluid particles. The flow regimes inside the annulus can be described through the Taylor number:

$$Ta = \frac{R\omega d}{\nu}\sqrt{\frac{d}{R}}$$

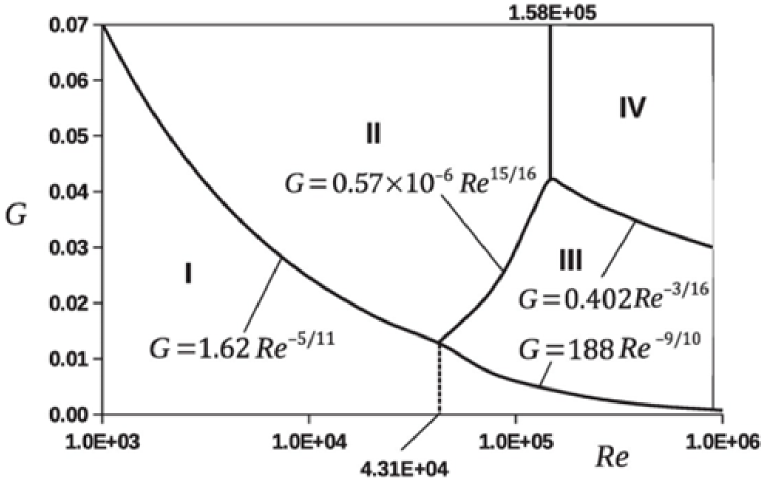

Figure 4.6: Flow regimes according to Daily and Nece [44].

where ν is the kinematic viscosity. The Taylor vortices appears starting from a value of $Ta_{cr} = 41.3$, while, for Taylor numbers greater than 400 the fluid is considered fully turbulent. This is usually the case of a fast-spinning flywheel. The air friction moment operating on the cylindrical surface, like the drag acting on the disk plates, is described by equation 4.14:

$$M = C_M \rho_a \, \pi \, l \, \omega^2 \, R^4 \cdot 0.5 \tag{4.14}$$

The moment coefficient for the axial contribution can be computed through the equations showed in table 4.3. $Re_{\phi m}$ is the Couette Reynolds number and is defined as:

$$Re_{\phi m} = \frac{R \, \omega \, d}{\nu}$$

The transversal contribution is computed through equation 4.10, but the moment coefficient is calculated through the equations listed in table 4.4.

Low Turbulent	$Re_{\phi m} \leq 10^4$	$C_M^a = 1.03 \left(\frac{d}{R}\right)^{0.3} Re_{\phi m}^{-0.5}$
High Turbulent	$Re_{\phi m} > 10^4$	$C_M^a = 0.065 \left(\frac{d}{R}\right)^{0.3} Re_{\phi m}^{-0.2}$

Table 4.3: Moment coefficients for the axial contribution of the drag computed through equation 4.14.

Laminar	$Re < 10^4$	$C_M = \frac{\pi}{s}\frac{R_1}{Re}$
Low Turbulent	$10^4 < Re < 2 \cdot 10^5$	$C_M = \frac{1.334}{\sqrt{Re}}$
High Turbulent	$Re > 2 \cdot 10^5$	$C_M = \frac{0.0311}{Re^{1/5}}$

Table 4.4: Moment coefficients for the transversal contribution of the drag computed through equation 4.10.

These models were applied to the specific case of the flywheel designed in the previous section, operating at the nominal speed divided by a safety factor of 0.95 and at room temperature. The data used to compute the drag moment are listed in table 4.5, while the results can be read in table 4.6.

Although the flywheels of the gyroscopic group are enclosed in a casing, the drag considered for designing the spinning motors is that of a rotor rotating in free space. The corresponding value can be found in table 4.6, and it's equal to 42 mNm. For motor design purposes, this value was divided by a safety factor of 0.8, resulting in a final drag value of 52 mNm.

DATA		
ρ_a	1.204 kg/m^3	air density at 20°C
ω	8420 rpm	angular speed
l	0,051 m	thickness of the rotor
R	0,066 m	external radius
b	0,005 m	air gap thickness between the rotor and the case
μ	$1.81 \cdot 10^{-5}$ kg/ms	dynamic viscosity of air at 20°C
R_{int}	0,005 m	radius of the flywheel shaft

Table 4.5: Data used to compute the Drag Moment.

Model	**Transversal**	**Circumferential**	**Drag**
Von Karman	14 mNm	-	14 mNm
Von Karman Corrected [41]	-	-	42 mNm
J. Abrahamsson et al. [42]	3.8 mNm	-	3.8 mNm
Antonello S. S. et al. [43]	4.9 mNm	2.6 mNm	10.1 mNm

Table 4.6: Data used to compute the drag moment on the flywheel when spinning at 8000 rpm.

Spinning Motors

The selection of the motors responsible for the spinning of the flywheels was made considering three parameters: the nominal torque, speed and voltage. The nominal torque needs to be greater than the air friction torque at the maximum spinning velocity. This value was found at the end of the previous paragraph and it was then divided by a safety factor of 0.8. The obtained result was 52 mNm. The nominal speed was fixed when designing the flywheel at 8000 rpm. As for the nominal torque, the value used for the motor choice has been divided by a safety factor of 0.95, obtaining a speed of approximately 8420 rpm. Finally, the nominal voltage was requested to be as close as possible to 12V.

The motor that satisfied these requirements was found in the Maxon catalogue. Its specifications can be read in figure 4.7. The Maxon website allows the customers to verify that the requested nominal working point is found inside the motor continuous operating area. Thanks to this tool it is possible to know also the voltage and current requested by the motor, which are $V_{nom} \approx 12.6\ V$ and $I_{nom} \approx 4.1\ A$.

A concise analysis of the motor's step response, considering its coupling with the flywheel, was conducted to determine the time required to reach the nominal speed.

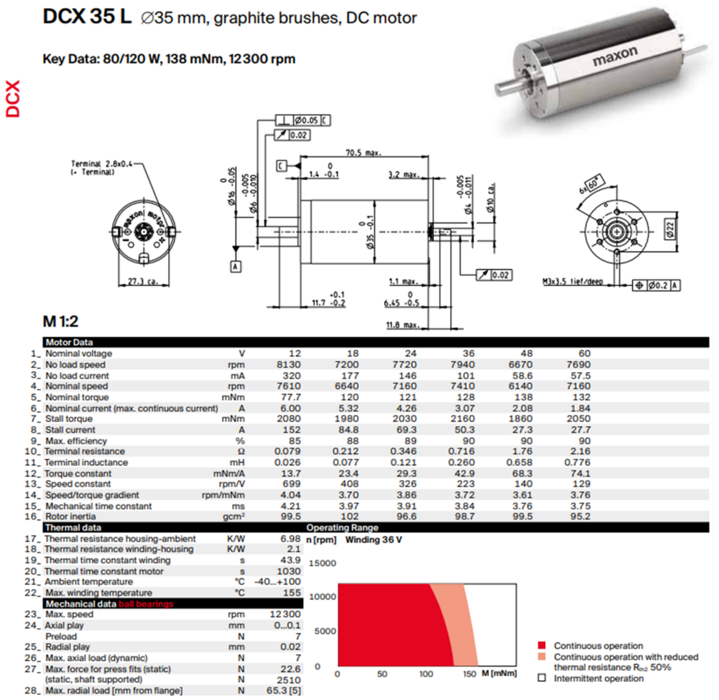

DCX 35 L Ø35 mm, graphite brushes, DC motor

Key Data: 80/120 W, 138 mNm, 12300 rpm

M 1:2

	Motor Data							
1	Nominal voltage	V	12	18	24	36	48	60
2	No load speed	rpm	8130	7200	7720	7940	6670	7690
3	No load current	mA	320	177	146	101	58.6	57.5
4	Nominal speed	rpm	7610	6640	7160	7410	6140	7160
5	Nominal torque	mNm	77.7	120	121	128	138	132
6	Nominal current (max. continuous current)	A	6.00	5.32	4.26	3.07	2.08	1.84
7	Stall torque	mNm	2080	1980	2030	2160	1860	2050
8	Stall current	A	152	84.8	69.3	50.3	27.3	27.7
9	Max. efficiency	%	85	88	89	90	90	90
10	Terminal resistance	Ω	0.079	0.212	0.346	0.716	1.76	2.16
11	Terminal inductance	mH	0.026	0.077	0.121	0.260	0.658	0.776
12	Torque constant	mNm/A	13.7	23.4	29.3	42.9	68.3	74.1
13	Speed constant	rpm/V	699	408	326	223	140	129
14	Speed/torque gradient	rpm/mNm	4.04	3.70	3.86	3.72	3.61	3.76
15	Mechanical time constant	ms	4.21	3.97	3.91	3.84	3.76	3.75
16	Rotor inertia	gcm²	99.5	102	96.6	98.7	99.5	95.2

	Thermal data		
17	Thermal resistance housing-ambient	K/W	6.98
18	Thermal resistance winding-housing	K/W	2.1
19	Thermal time constant winding	s	43.9
20	Thermal time constant motor	s	1030
21	Ambient temperature	°C	-40...+100
22	Max. winding temperature	°C	155
	Mechanical data ball bearings		
23	Max. speed	rpm	12300
24	Axial play	mm	0...0.1
	Preload	N	7
25	Radial play	mm	0.02
26	Max. axial load (dynamic)	N	7
27	Max. force for press fits (static)	N	22.6
	(static, shaft supported)	N	2510
28	Max. radial load [mm from flange]	N	65.3 [5]

Operating Range

🟥 Continuous operation
🟧 Continuous operation with reduced thermal resistance R_{th2} 50%
☐ Intermittent operation

Figure 4.7: Data sheet of the selected motor for the spinning motion.

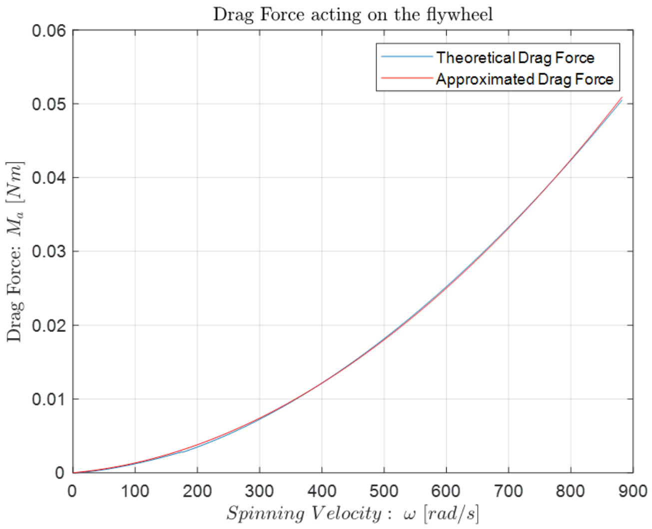

Figure 4.8: Drag force evolution against spinning velocity. In blue the theoretical curve, in red the approximation.

The dynamic model of the system was studied. The differential equation is the following one:

$$I\ddot{\theta} + \tau_a = \tau_m \tag{4.15}$$

where τ_a is the drag moment, while τ_m is the motor torque. The equation of the motor is the following one:

$$\dot{\theta} = k_v V_{mot} - k_\tau \tau_m \qquad \rightarrow \qquad \tau_m = \frac{k_v V_{mot} - \dot{\theta}}{k_\tau} \tag{4.16}$$

where k_v and k_τ are the speed constant and speed/torque gradient, respectively (these values are written in the motor catalogue). Substituting this equation into the first one, the differential equation becomes:

$$I\ddot{\theta} + \tau_a + \frac{\dot{\theta}}{k_\tau} = \frac{k_v V_{mot}}{k_\tau} \tag{4.17}$$

The drag moment equation is 4.10, where the moment coefficient was computed through the equations of table 4.2 and corrected as shown in equation 4.12. To simplify the problem, this function was approximated to a second order equation of the type:

$$\tau_{air} = k_{a1}\dot{\theta} + k_{a2}\dot{\theta}^2 \tag{4.18}$$

where $k_{a1} = 0.11 \cdot 10^{-4}$ and $k_{a2} = 0.8 \cdot 10^{-7}$. Image 4.8 depicts the variation of air friction as a function of the spinning velocity for both the real and the approximated models.

The dynamic model of the system after substituting the approximation of the drag moment is described by the following equation:

$$I\ddot{\theta} + (k_{a1}\dot{\theta} + k_{a2}\dot{\theta}^2) + \frac{\dot{\theta}}{k_\tau} = \frac{k_v V_{mot}}{k_\tau} \tag{4.19}$$

Having defined the state variable $x = [x_1;\ x_2]$, the state space representation of the problem has the following form:

$$\begin{cases} \dot{x}_1 &= x_2 \\ \dot{x}_2 &= \frac{k_v V - x_2}{I k_\tau} - \frac{k_{a1}x_2 + k_{a2}x_2^2}{I} \end{cases} \tag{4.20}$$

The non-linear differential problem can be effectively solved through numerical integration methods. In this case, the second-order Runge-Kutta method was selected. The step response of the system is illustrated in figure 4.9, which shows the time required to reach the nominal speed is approximately $T_{w_{nom}} = 16\ s$.

This result provides valuable insights into the system’s behavior. In scenarios where a “boost” effect is required, the flywheel needs to reach its nominal speed before its application. The 16-seconds "charging time" is a reasonable duration, but it can be further reduced by developing a dedicated controller.

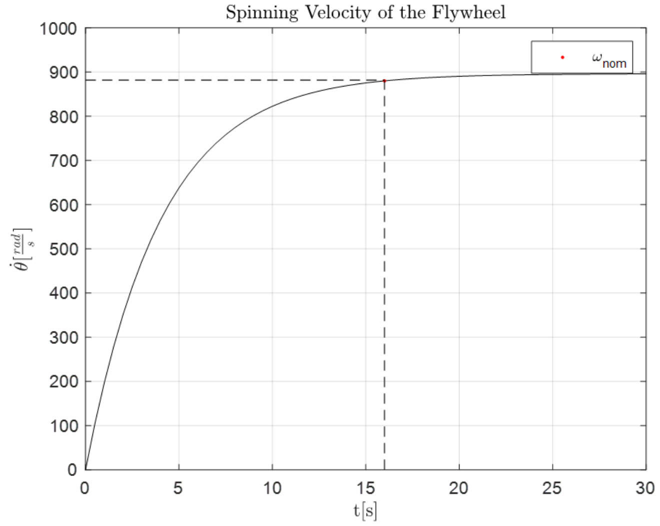

Figure 4.9: Step response of the motor coupled with the flywheel.

Gyroscope Design

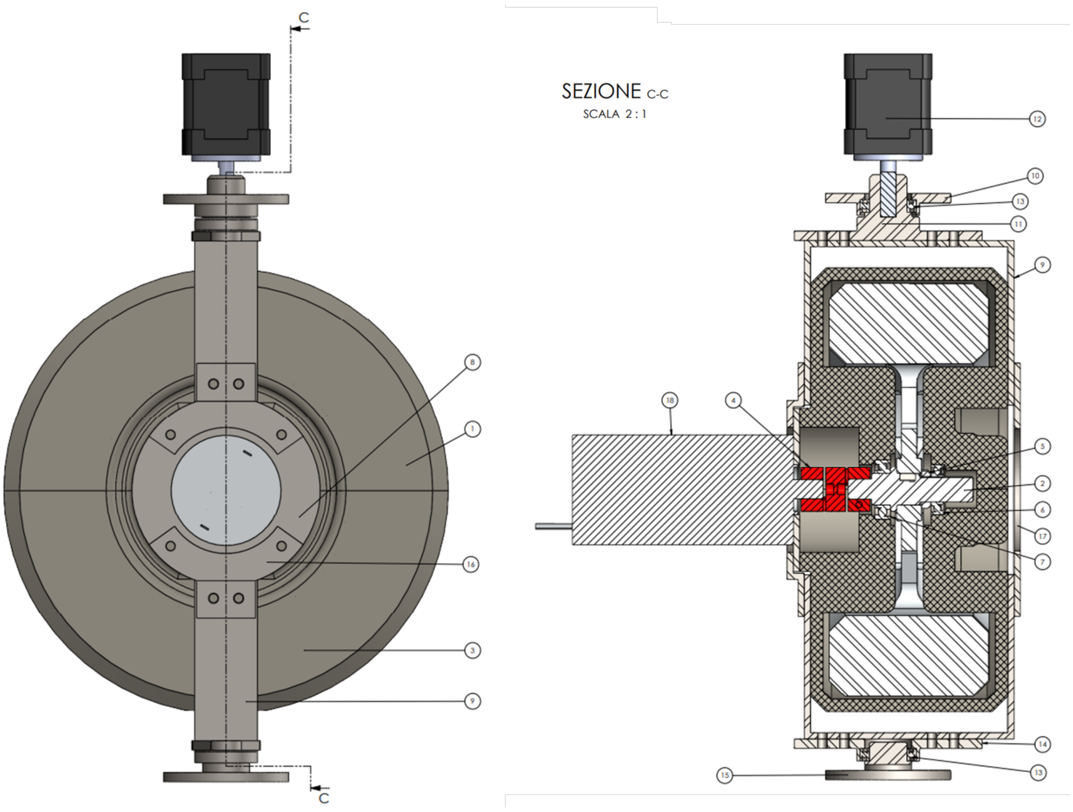

Figure 4.10: Front view and lateral cross-section of the gyroscope. The components are: 1) first half of the case, 2) shaft, 3) second half of the case, 4) Jaw coupling, 5) Spacer, 6) Small angular contact ball bearing, 7) Big angular contact ball bearing, 8) Motor plate, 9) C-plate for tilting motor connection, 10) Flange$_1$ for main structure connection, 11) Flange$_1$ for tilting motor-gyroscope connection, 12) Tilting motor, 13) Angular contact ball bearings for tilting axis positioning, 14) Flange$_2$ for tilting motor-gyroscope connection, 15) Flange$_2$ for main structure connection, 16) Motor-to-C-plate connection plate, 17) Closing Plate, 18) Spinning Motor.

In the preceding paragraphs, the design of the flywheel and the motors responsible for its spinning motion was presented. These components constitute the main elements of the gyroscopic group. Here, a concise explanation of the overall design is provided.

In figure 4.10, a front view and a lateral cross-section of the system are illustrated. All the components are listed in the image caption. The motor is connected to the shaft through a jaw coupling, which was selected from the MIKI PULLEY STARFLEX catalogue (figure 4.11).

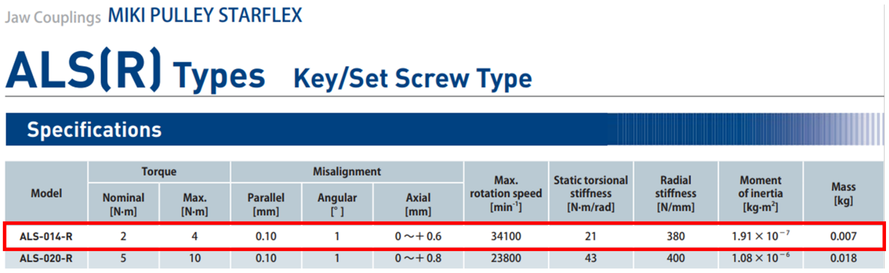

Jaw Couplings **MIKI PULLEY STARFLEX**

ALS(R) Types Key/Set Screw Type

Specifications

Model	Torque		Misalignment			Max. rotation speed [min⁻¹]	Static torsional stiffness [N·m/rad]	Radial stiffness [N/mm]	Moment of inertia [kg·m²]	Mass [kg]
	Nominal [N·m]	Max. [N·m]	Parallel [mm]	Angular [°]	Axial [mm]					
ALS-014-R	2	4	0.10	1	0 ∼ + 0.6	34100	21	380	1.91×10^{-7}	0.007
ALS-020-R	5	10	0.10	1	0 ∼ + 0.8	23800	43	400	1.08×10^{-6}	0.018

Figure 4.11: ALS-014-R jaw coupling from the MIKI PULLEY STARFLEX catalogue.

A static load analysis was performed to determine the minimum shaft diameter. The equation used is the following one:

$$d = \sqrt[3]{\frac{16}{\pi \ \sigma_{adm}} \sqrt{4M_f^2 + 3M_t^2}} \tag{4.21}$$

where M_f and M_t are the bending and torsional moment, respectively; σ_{adm} is the admissible stress, and it is computed as R/n, which is the tensile strength (a mean value of 600 MPa is usually used for steel) divided by a safety factor (for this application, a value of 8 was chosen). For a beam of 50 mm of length, a value of 6.2 mm was obtained. The designed shaft doesn't have a constant cross section, but its minimum diameter is equal to 8 mm.

The gyro case (figure 4.10, numbers 1 and 3) was designed not only to provide structural support for the entire system but also to enhance user safety during operation and minimize drag friction. To allow the system assembling operations, it was divided into two halves that are then held together through screws and connecting plates.

The tilting motor axis was vertically aligned with the barycenter of the system. This measure allowed to select a smaller motor[1].The TRINAMIC Motion Control catalogue was used to select a suitable stepper motor (QMot QSH2818) for the system. Elements 10 and 15 serve as connectors between the system and the pendulum structure, bearing the entire weight of the system. As a result, there is no shear load exerted on the shaft of the stepper motor.

Finally, a rendering of the gyroscope system can be seen in figure 4.12.

---

[1]: The moment arm of the gyroscope weight is zero, meaning that the motor torque does not need to overcome the weight of the system when tilting the gyroscope

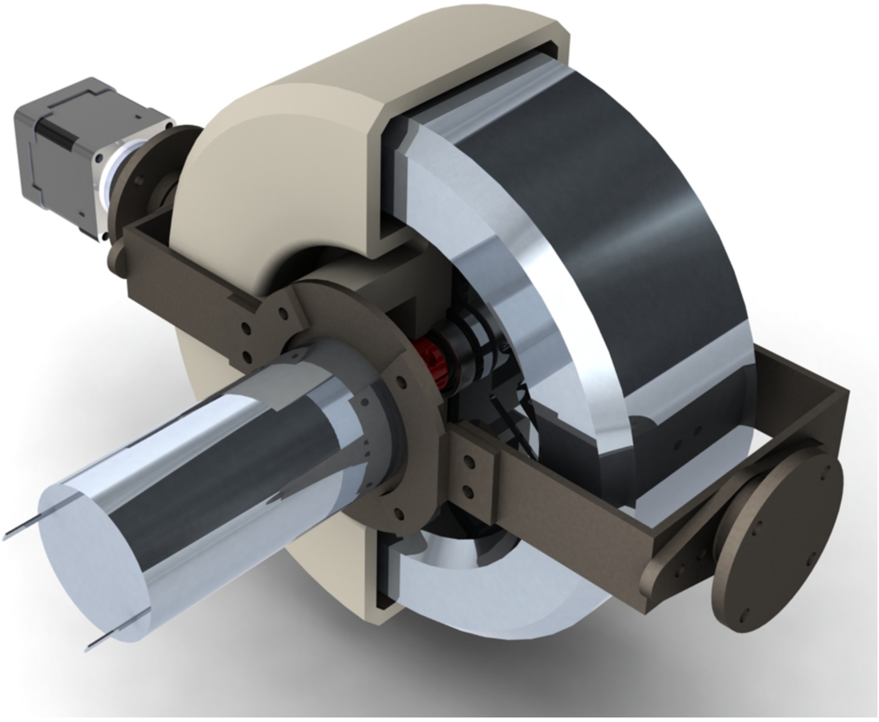

Figure 4.12: Rendering of the gyroscope (the lower half of the case was removed).

4.2.2 Main Motors Dimensioning

As already explained in the previous sections, the 2-DOF pendulum from [1] was adopted as the main driving system. However, the originally selected motors from [1] couldn't be used due to changes in weight distribution and power requirements. This paragraph outlines the design process of the new gearbox and motor.

One of the design specifications outlined in table 1.2 is the required nominal speed for the robot to maintain while climbing a 15° slope. This requirement was used to compute the design specifications of the gearbox and the motor. First, the angle of the pendulum necessary to maintain an equilibrium condition was computed. It was observed that a static condition is achieved when the barycenter of the robot is vertically aligned with the contact point between the shell and the ground (see figure 4.13). Therefore, the pendulum angle can be computed as:

$$\theta_{eq} = \arcsin\left(\frac{R_s}{a}\sin\alpha\right) \tag{4.22}$$

Next, the nominal torque needed to maintain still the pendulum can be calculated

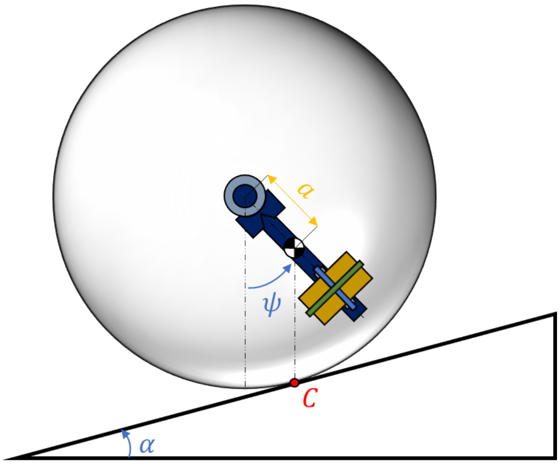

Figure 4.13: SR in equilibrium condition while climbing a slope of 15°.

through equation 4.23:

$$\tau_{nom,s} = m_p \; g \; l \; \sin\theta \tag{4.23}$$

where l is the distance from the sphere center of the barycenter to the pendulum and it is computed as $l = \frac{M}{M+m_p} \cdot a$.

The power transmitted to the main shaft of the robot can be calculated by multiplying the torque by the angular speed of the sphere. Dividing this result by two and including the efficiencies of the differential system (η_D) and the toothed belt transmission (η_B), the power coming out of the gearbox is obtained:

$$P_r = \frac{\tau_{nom,s} \; \omega_{nom}}{2 \; \eta_D \; \eta_B} \tag{4.24}$$

From this result, the nominal torque the gearbox must withstand can be computed:

$$\tau_{nom,r} = \frac{P_r}{\omega_{nom}} \tag{4.25}$$

Finally, another important requirement that must be considered when selecting a gearbox is the maximum torque that it can withstand ($\tau_{max,r}$). The minimum value can be computed by dividing by two the sum of the torque needed to raise the pendulum at a 90° angle and the maximum gyroscopic torque.

The used data and the obtained results can be read in table 4.7. The efficiencies are the same that were used in [1].

Once all the design specification were collected, first the gearbox was chosen, then a compatible motor was selected. The two main requirements for the gearbox were the nominal and the maximum torque. The gear ratio was selected to be as close as possible to the maximum admissible ratio, which can be determined by dividing the maximum continuous input speed of the gearbox by the desired output speed (ω_{nom}). By doing so, the torque required for the coupled motor is minimized.

Finally, the selection of the motor was carried out computing its minimum output power, the nominal speed, and the nominal torque. These three values are calculated through the following equations:

$$P_m = \frac{P_r}{\eta_r} \tag{4.26}$$

$$\omega_{nom,m} = n_{nom,r}\ i_r \cdot \frac{\pi}{30} \tag{4.27}$$

$$\tau_{nom,m} = \frac{P_m}{\omega_{nom,m}} \tag{4.28}$$

The gearbox that was chosen is the Planetary Gearhead GP 42 C, while the motor is the RE 40; both were selected from the Maxon catalogue. Their technical data are shown in figures 4.14 and 4.15.

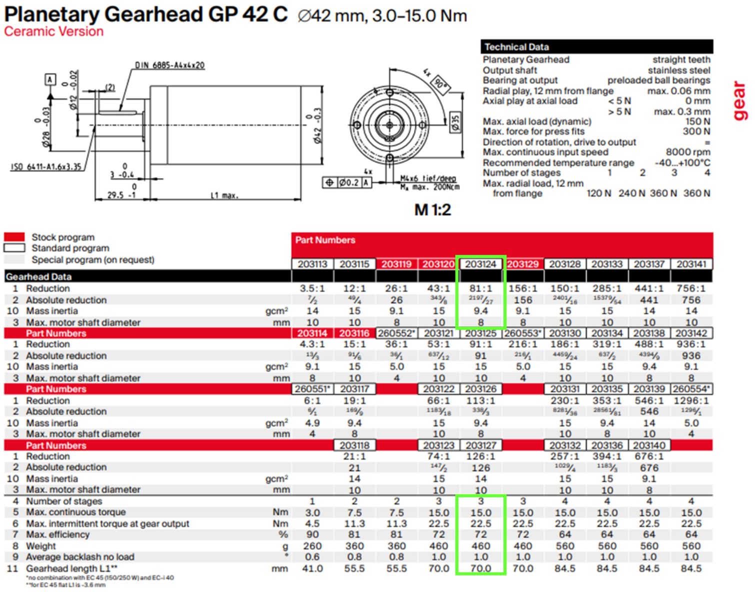

Planetary Gearhead GP 42 C ∅42 mm, 3.0–15.0 Nm
Ceramic Version

Technical Data		
Planetary Gearhead		straight teeth
Output shaft		stainless steel
Bearing at output		preloaded ball bearings
Radial play, 12 mm from flange		max. 0.06 mm
Axial play at axial load	< 5 N	0 mm
	> 5 N	max. 0.3 mm
Max. axial load (dynamic)		150 N
Max. force for press fits		300 N
Direction of rotation, drive to output		=
Max. continuous input speed		8000 rpm
Recommended temperature range		-40...+100°C

Number of stages	1	2	3	4
Max. radial load, 12 mm from flange	120 N	240 N	360 N	360 N

🟥 Stock program
☐ Standard program
▨ Special program (on request)

			Part Numbers									
			203113	203115	203119	203120	203124	203129	203128	203133	203137	203141
	Gearhead Data											
1	Reduction		3.5 : 1	12 : 1	26 : 1	43 : 1	81 : 1	156 : 1	150 : 1	285 : 1	441 : 1	756 : 1
2	Absolute reduction		$^{7}/_{2}$	$^{49}/_{4}$	26	$^{343}/_{8}$	$^{2197}/_{27}$	156	$^{2401}/_{16}$	$^{15379}/_{54}$	441	756
10	Mass inertia	gcm²	14	15	9.1	15	9.4	9.1	15	15	14	14
3	Max. motor shaft diameter	mm	10	10	8	10	8	8	10	10	10	10
	Part Numbers		203114	203116	260552*	203121	203125	260553*	203130	203134	203138	203142
1	Reduction		4.3 : 1	15 : 1	36 : 1	53 : 1	91 : 1	216 : 1	186 : 1	319 : 1	488 : 1	936 : 1
2	Absolute reduction		$^{13}/_{3}$	$^{91}/_{6}$	$^{36}/_{1}$	$^{637}/_{12}$	91	$^{216}/_{1}$	$^{4459}/_{24}$	$^{637}/_{2}$	$^{4394}/_{9}$	936
10	Mass inertia	gcm²	9.1	15	5.0	15	15	5.0	15	15	9.4	9.1
3	Max. motor shaft diameter	mm	8	10	4	10	10	4	10	10	8	8
	Part Numbers		260551*	203117		203122	203126		203131	203135	203139	260554*
1	Reduction		6 : 1	19 : 1		66 : 1	113 : 1		230 : 1	353 : 1	546 : 1	1296 : 1
2	Absolute reduction		$^{6}/_{1}$	$^{169}/_{9}$		$^{1183}/_{18}$	$^{338}/_{3}$		$^{8281}/_{36}$	$^{28561}/_{81}$	546	$^{1296}/_{1}$
10	Mass inertia	gcm²	4.9	9.4		15	9.4		15	9.4	14	5.0
3	Max. motor shaft diameter	mm	4	8		10	8		10	8	10	4
	Part Numbers			203118		203123	203127		203132	203136	203140	
1	Reduction			21 : 1		74 : 1	126 : 1		257 : 1	394 : 1	676 : 1	
2	Absolute reduction			21		$^{147}/_{2}$	126		$^{1029}/_{4}$	$^{1183}/_{3}$	676	
10	Mass inertia	gcm²		14		15	14		15	15	9.1	
3	Max. motor shaft diameter	mm		10		10	10		10	10	8	
4	Number of stages		1	2	2	3	3	3	4	4	4	4
5	Max. continuous torque	Nm	3.0	7.5	7.5	15.0	15.0	15.0	15.0	15.0	15.0	15.0
6	Max. intermittent torque at gear output	Nm	4.5	11.3	11.3	22.5	22.5	22.5	22.5	22.5	22.5	22.5
7	Max. efficiency	%	90	81	81	72	72	72	64	64	64	64
8	Weight	g	260	360	360	460	460	460	560	560	560	560
9	Average backlash no load	°	0.6	0.8	0.8	1.0	1.0	1.0	1.0	1.0	1.0	1.0
11	Gearhead length L1**	mm	41.0	55.5	55.5	70.0	70.0	70.0	84.5	84.5	84.5	84.5

*no combination with EC 45 (150/250 W) and EC-i 40
**for EC 45 flat L1 is -3.6 mm

Figure 4.14: Technical data of the selected Gearbox.

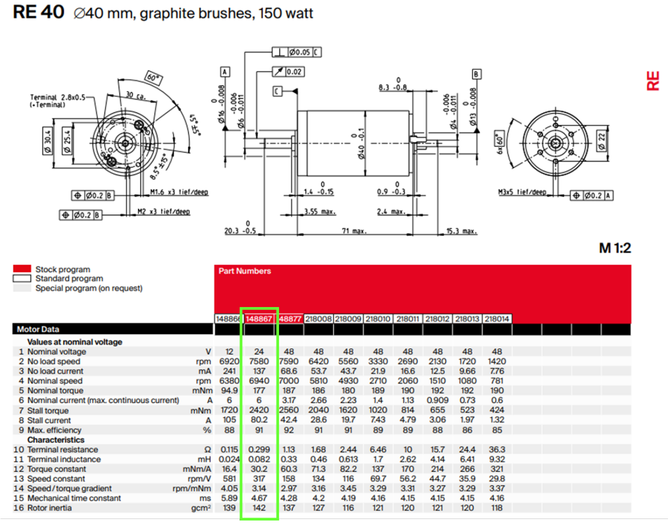

RE 40 ⌀40 mm, graphite brushes, 150 watt

🟥 Stock program
☐ Standard program
▨ Special program (on request)

Part Numbers		148866	148867	48877	218008	218009	218010	218011	218012	218013	218014
Motor Data											
Values at nominal voltage											
1 Nominal voltage	V	12	24	48	48	48	48	48	48	48	48
2 No load speed	rpm	6920	7580	7590	6420	5560	3330	2690	2130	1720	1420
3 No load current	mA	241	137	68.6	53.7	43.7	21.9	16.6	12.5	9.66	7.76
4 Nominal speed	rpm	6380	6940	7000	5810	4930	2710	2060	1510	1080	781
5 Nominal torque	mNm	94.9	177	187	186	180	189	190	192	192	190
6 Nominal current (max. continuous current)	A	6	6	3.17	2.66	2.23	1.4	1.13	0.909	0.73	0.6
7 Stall torque	mNm	1720	2420	2560	2040	1620	1020	814	655	523	424
8 Stall current	A	105	80.2	42.4	28.6	19.7	7.43	4.79	3.06	1.97	1.32
9 Max. efficiency	%	88	91	92	91	91	89	89	88	86	85
Characteristics											
10 Terminal resistance	Ω	0.115	0.299	1.13	1.68	2.44	6.46	10	15.7	24.4	36.3
11 Terminal inductance	mH	0.024	0.082	0.33	0.46	0.613	1.7	2.62	4.14	6.41	9.32
12 Torque constant	mNm/A	16.4	30.2	60.3	71.3	82.2	137	170	214	266	321
13 Speed constant	rpm/V	581	317	158	134	116	69.7	56.2	44.7	35.9	29.8
14 Speed/torque gradient	rpm/mNm	4.05	3.14	2.97	3.16	3.45	3.29	3.31	3.27	3.29	3.37
15 Mechanical time constant	ms	5.89	4.67	4.28	4.2	4.19	4.16	4.15	4.15	4.15	4.16
16 Rotor inertia	gcm²	139	142	137	127	116	121	120	121	120	118

Figure 4.15: Technical data of the selected Motor.

	DATA	
M	$6\ kg$	Shell + differential system weight
m_p	$16\ kg$	Pendulum weight
a	$87.5\ mm$	Barycenter position of the SR
α	$15°$	Angle of the slope
η_D	0.98	Efficiency of the differential sys.
η_B	0.95	Efficiency of the toothed belt
	RESULTS	
θ_{eq}	$48°$	Angle of the pendulum
l	0.12	Baryenter of the pendulum
ω_{nom}	$10\ rad/s$	Nominal angular speed of the SR
$\tau_{nom,s}$	$13.96\ Nm$	Nominal torque at the shaft
i_r	$81:1$	Gear ratio
P_r	$75\ W$	Output power of motor + gearbox
$\tau_{nom,r}$	$7.5\ Nm$	Nominal torque at the gearbox
$\tau_{max,r}$	$22\ Nm$	Maximum torque at the gearbox
P_m	$104\ W$	Output power of the motor
$\tau_{nom,m}$	$0.129\ Nm$	Nominal torque of the motor
$\tau_{max,m}$	$0.276\ Nm$	Maximum torque of the motor

Table 4.7: Data used to design the main motors and results of the equation presented in the paragraph. The results are divided in three: the first group are general results, the second one is relative to the gearbox, while the third one to the motor. The motor results have been obtained after the gearbox selection

4.2.3 Pendulum Structure Design

The pendulum structure of the spherical robot plays a crucial role in its overall functionality and stability. It was designed to support the CMG group, the main motors, the batteries and the hardware components. Its design focuses on achieving a balance between structural integrity, weight optimization, and compactness. To meet these requirements, a combination of steel and aluminum alloy plates was chosen as the primary construction materials.

One of the main obstacles encountered during the design process was accommodating the space limitations imposed by the spherical shape of the robot. The CMG group had to be able to rotate around its tilting axis without hitting any other components. Another significant challenge to overcome was meeting the requirements for the barycenter placement. The final result is a light structure of less than 0,425 *kg* which leaves the possibility for future upgrades thanks to its modularity. Figure 4.16 shows an isometric view of the structure outlining all the components.

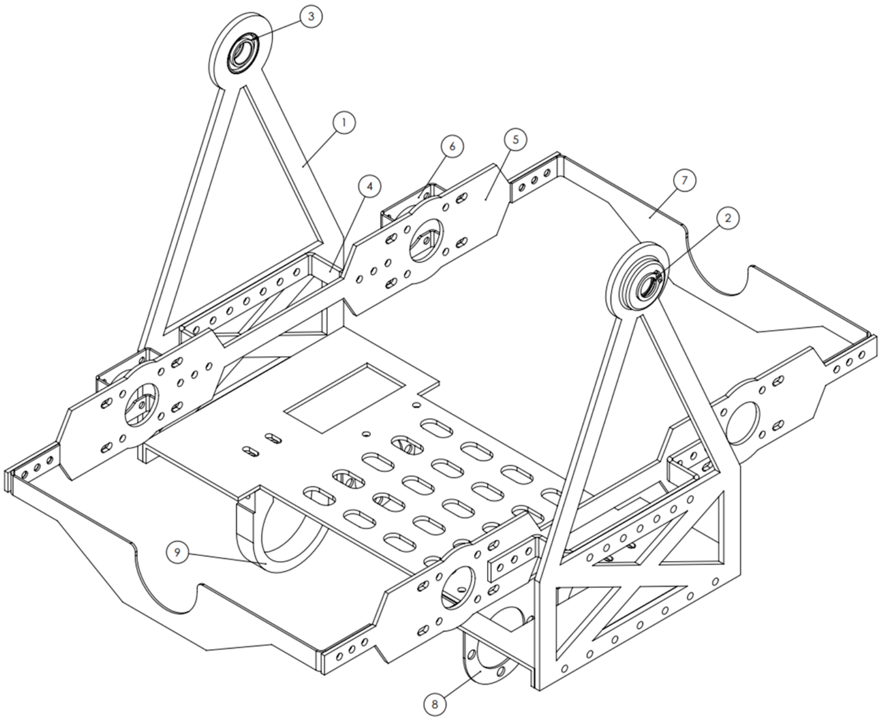

Figure 4.16: Isometric view of the Pendulum structure. The main components are: 1) Swinging rod, 2) Seeger, 3) Angular contact ball bearing, 4) Connecting plate, 5) CMG-holding plate, 6) Tilting motor plates, 7) Plate with spinning motor positioning hole, 8) Main motor positioning plate, 9) Main motor holding ring.

When placing the main motors and the CMG group, the total weight of the system is about 12 kg, with 4 kg still available for batteries and hardware components. A rendering of the pendulum is shown in figure 4.17.

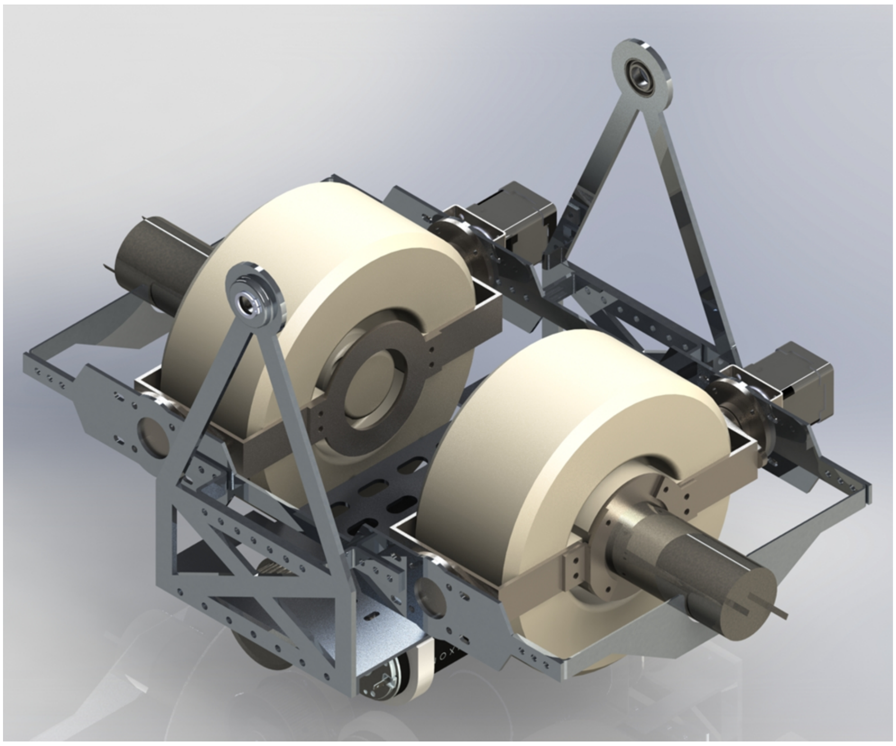

Figure 4.17: Rendering of the Pendulum Structure holding the two CMG groups and the main motors.

4.2.4 Toothed Belt Design

The power transmission from the main motors to the differential system is achieved through two toothed belts. Due to changes in the arrangement of internal components, the original sizing from [1] could not be used, necessitating a redesign of the belts. To select the most suitable transmission belts, the procedure outlined in the "POGGI Catalog 3315X" was followed.

The GT3 belt type was chosen. The theoretical pitch length of the belt was computed through the following equation:

$$L_t = 2 \cdot i + 1.57 \cdot (D_p + d_p) + \frac{(D_p + d_p)^2}{4 \cdot i} \tag{4.29}$$

where i is the interaxis of the two pulleys, and D_p and d_p are their diameters. The pulleys were selected from the Misumi catalogue (code GPT44GT3150-A-N12) and they have 44 teeth both. This value was used to compute their diameters:

$$D_p = \frac{p \cdot z}{\pi} \tag{4.30}$$

Once the theoretical pitch length was computed, the closest value was selected from the catalogue.

Finally the maximum transmitted power was computed through the following equation:

$$P_t = P_b \cdot C_L \cdot C_d \cdot L_f \tag{4.31}$$

where P_b is the transmitted power rating, L_f is the length factor and depends on the belt pitch and the belt length, C_D is the teeth-in-mesh factor and it depends on the number of teeth in mesh, and C_L is the belt width factor. The values of these parameters were obtained from the catalogue and are summarized in table 4.8. It is evident that the maximum transmitted power significantly exceeds the nominal output power of the gearbox.

TOOTHED BELT DESIGN		
i	203 mm	Pulleys interaxis
D_p	42.02 mm	Pulley$_1$ diameter
d_p	42.02 mm	Pulley$_2$ diameter
L_t	549 mm	Theoretical pitch length
L_r	552 mm	Pitch length from catalogue
P_b	87 W	Transmitted power rating
C_L	1.89	Belt width factor.
C_d	1 W	Teeth-in-mesh factor
L_f	1.1 W	Length factor
P_t	181 W	Maximum transmitted power

Table 4.8: Data used to compute the Drag Moment.

4.2.5 Electrical Integration

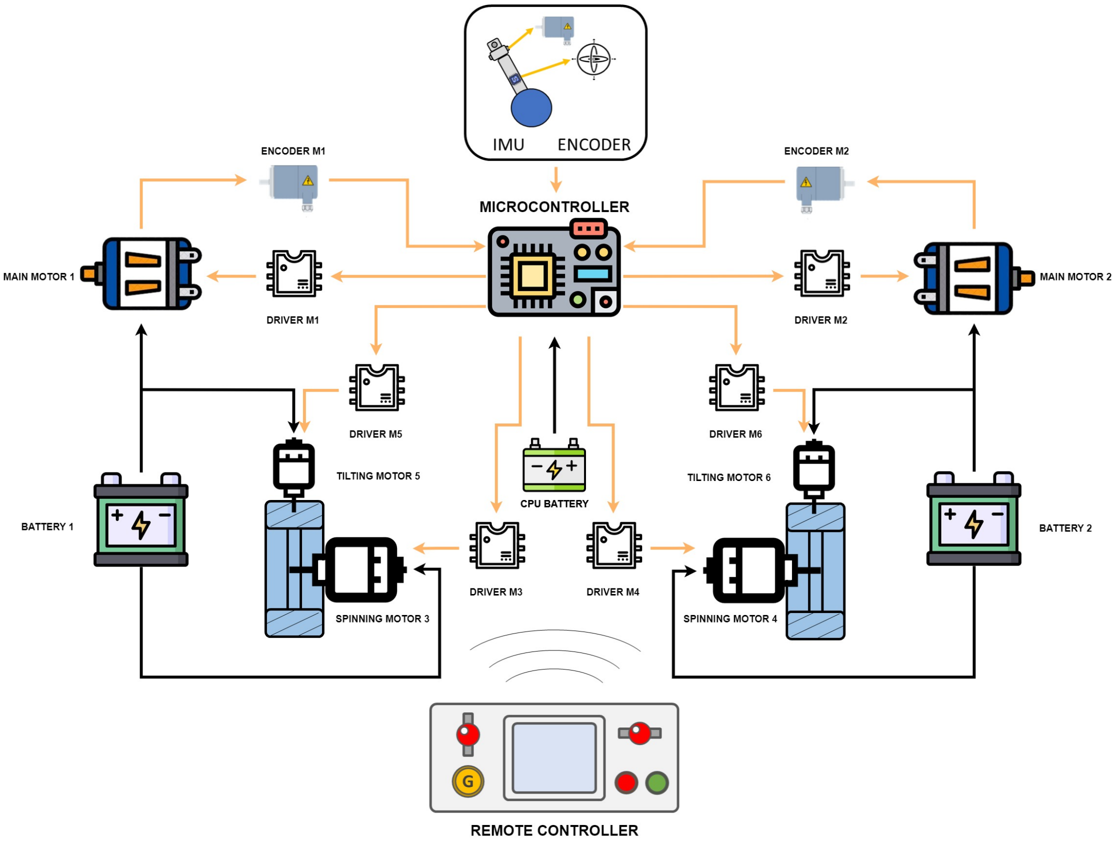

Figure 4.18: Diagram of the hardware configuration.

The hardware configuration of the SR encompasses a comprehensive set of components that work in harmony to enable its functionality and control. In figure 4.18, a diagram illustrating the layout is presented. Serving as the central processing unit, a microcontroller assumes the role of the robot's brain, orchestrating the execution of tasks and coordinating the interplay between different hardware modules.

"Main motor 1" and "Main motor 2" are the two motors responsible for controlling the orientation of pendulum. Motors 3 and 4 are the ones responsible for the spinning motion of the gyroscope flywheels, while motors 5 and 6 are the ones used to perform the tilting movement. To ensure efficient operation and control of the motors, all of them are equipped with dedicated drivers

For a simple teleoperated functioning, four sensors are needed. The two main motors are equipped with encoders, which enable real-time measurement and feedback of their rotational speed. The pendulum structure includes an Inertia Measurement Unit (IMU), that enables the tracking of angular displacements and velocities relative to the world frame. Additionally, an encoder is used to measure the angle between the pendulum and the central shaft longitudinal axes. These measurements provide a crucial feedback for control algorithms.

Power supply is a critical aspect of the robot's operation, and thus, it relies on two larger batteries to provide power to the six motors. These batteries were carefully selected to meet the demands of the system in terms of space, weight, and desired runtime of the robot. In addition to the larger batteries, a smaller battery is dedicated to powering the microcontroller and the various sensors integrated into the system, ensuring their independent and reliable operation.

Finally, to allow the user interaction with the robot, a remote controller communicating via radio or Wi-Fi is adopted

Battery Dimensioning

The dimensioning of the batteries was carried out to meet the runtime requirement of a minimum of 1 h while working at the nominal operating point (climbing a slope of 15° at a speed of 2.5 m/s). To select the most suitable batteries, it was necessary to compute the nominal current and voltage requested by the motors. These can be calculated knowing the nominal torque and speed. The first one is outlined in table 4.7, while the second one can be computed multiplying the gearbox output speed by the gear ratio i_r. The results obtained are: $\tau_{nom,m} = 0.129\ Nm$ and $n_{nom,m} = 7735$.

The nominal voltage is then calculated using eq. 4.16, where k_v and k_τ are outlined in the motor catalogue (speed constant and speed/torque gradient from fig. 4.15). The nominal current is obtained multiplying the torque constant by the nominal torque. The results are: $V_{nom} = 25.7\ V$ and $I_{nom} = 4.3\ A$. Therefore, to ensure a runtime of 1 h, a battery with a minimum nominal capacity of 4300 mAh must be selected. Currently, the most suitable option on the market is the Li-Ion battery, with a nominal voltage of 3.6 V and a capacity around 2500 mAh. To obtain a capacity equal or greater than the one needed, two batteries must be placed in a parallel configuration, while the requested voltage is achieved with a minimum of 8 batteries placed in a series configuration. Therefore, a 8s2p Li-Ion battery pack, such as the one offered by MaxAmps with a capacity of 5200 mAh and a nominal voltage of 28.8 V, should satisfy the project requirements.

Gyroscope impact on Battery Life

The influence of the gyroscope's operation on battery life can't be ignored.The primary power-consuming component of the gyroscope is the motor responsible for spinning the flywheel. Therefore, the power requested to spin the flywheel at its maximum velocity (8000 rpm) was evaluated.

Consider the motor supplied with a step input voltage of 12 V, following the approach outlined in paragraph 4.2.1. By solving the differential equation described in equation 4.20, the torque of the motor can be determined using equation 4.16. Dividing this result by the torque motor constant (from the catalogue), the current as a function of time can be derived. The integral of this curve provides the total charge consumed by the motor over a specific time period. It was estimated that spinning the flywheel from a standstill for one minute would consume approximately 4.3 % of the total charge of a battery with a capacity of 5200 mAh.

During a gyroscope-assisted maneuver, the primary motors are responsible for counterbalancing the gyroscopic torque in order to stabilize the pendulum and transfer the torque to the sphere. The maximum torque that can be requested to the motors is the amount necessary to sustain the pendulum in a raised position at a 90° angle throughout the entire maneuver. In paragraph 4.2.1, the maximum gyroscopic torque was evaluated and it resulted $\tau_{G,MAX} = 25.82\ N \cdot m$. The torque needed to raise the pendulum at a 90° angle can be computed through equation 4.23 and it's equal to $\tau_{90^\circ} = 18.88\ N\ m$. Therefore, the total torque requested to each one of the main motors results:

$$\tau_M = \frac{18.88 + 25.82 \cdot sin\left(\Omega\ t\right)}{2} \tag{4.32}$$

where $t \in \left[0, \frac{pi}{2\Omega}\right]$, while Ω is the tilting velocity of the gyroscope and it's equal to $\Omega = 15\ rpm$. Integrating this equation over the time interval the total charge consumed is computed. The obtained result is approximately the 3.1 % of the total charge of a 5200 mAh battery.

Therefore, the total amount of charge consumed when the gyroscope are used can reach up to a 7.4 % of the total charge of a 5200 mAh battery.

4.3 Design Result and Considerations

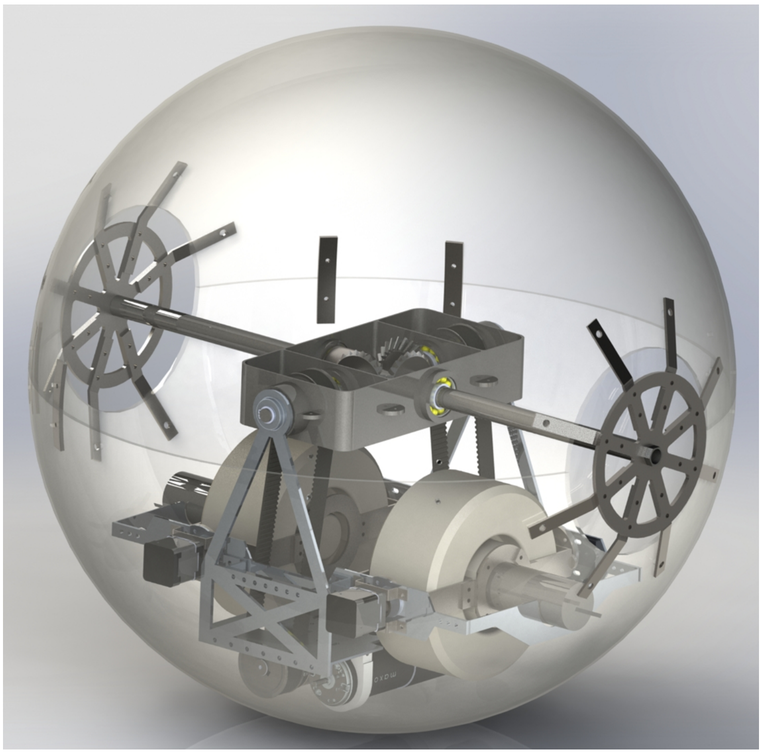

Figure 4.19: Rendering of the CAD model of the Spherical Robot.

In this chapter, a comprehensive overview of the key considerations and decision-making processes involved in creating a functional and efficient robot were presented. By carefully analyzing the requirements and constraints, various design elements such as the CMG group, pendulum structure, motors of the robot, and hardware layout have been addressed. The final result of this process is shown in figure 4.19. In this CAD model, the hardware components weren't included, but the design was implemented to accommodate the space they require.

A PMMA shell was used instead of the harmonic steel sheets of the SR from [1] because they were considered too flexible. A second layer made of impermeable rubber is needed to enhance the static friction of the shell on the ground, like in [1].

The total weight of the model is approximately 18 kg, where the pendulum accounts for 12 kg. The motors and the CMG group were designed to work with a pendulum of 16 kg. Consequently, the hardware components can weigh up to 4 kg and still respect the project requirements.

In the next chapter, the analytical model of the robot will be studied and the multybody simulation will be introduced.

Chapter 5

Modeling of the Spherical Robot

5.1 Introduction

In the preceding chapter, a comprehensive presentation of the design of the spherical robot was provided, highlighting the principal considerations and processes employed to achieve a functional and efficient robotic system. The subsequent chapter focuses on the analysis of the models that accurately represents the behavior and dynamics of the robot. These models play a pivotal role in investigating the robot's response to varying inputs and external forces, as well as facilitating the design of the control system.

Within this chapter, various mathematical frameworks will be examined. Firstly, the dynamic model of the robot within a two-dimensional (2D) environment is thoroughly investigated. Subsequently, a Simulink Simscape-based multi-body model is introduced. Although the multibody simulation provides a more comprehensive representation of the robot's behavior, the 2D analytical model played a pivotal role in the development of the control system for the robot's forward movements. It facilitated the adoption of classical control techniques that rely on the mathematical description of the system. Furthermore, the analytical simulation needs much less computing power than the multibody simulation, resulting in significantly reduced execution time.

5.2 Two-Dimensional Analytical Model

The analytical model of the spherical robot was initially realized in two dimensions. This allowed to study the SR forward and backward movements on an inclined pane. This model was then exploited to tune the parameters of the control system responsible for the straight line motion control of the robot.

5.2.1 Two-Dimensional Kinematics

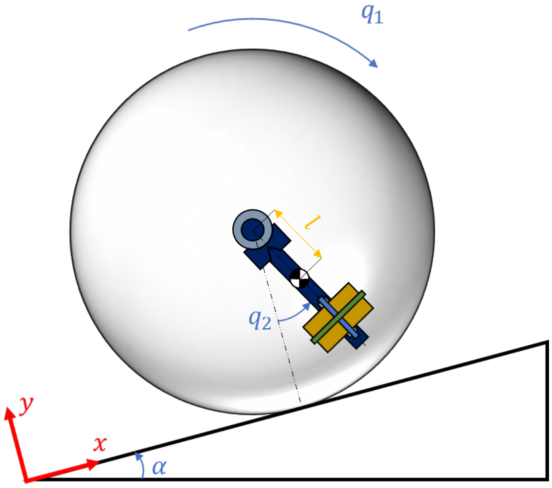

Figure 5.1: Two-dimensional representation of the robot climbing a slope. q_1 and q_2 are the generalized variables

The problem of the robot moving in a straight line motion on an inclined plane is represented through a schematic illustration in fig. 5.1. the problem can be easily described through two generalized variables: the angle of rotation of the sphere computed from the starting position (q_1), and the lifting angle of the pendulum measured from the line perpendicular to the inclined plane (q_2). Considering a fixed reference system wit the x-axis parallel to the inclined plane, the robot's x-coordinate can be defined under the assumption of pure rolling as:

$$x = R \cdot \theta$$

where R is the radius of the sphere. Therefore, the position and linear velocity, as well as the rotational velocity of the sphere can be described as:

$$\vec{r}_1 = \begin{bmatrix} q_1 R \\ R \\ 0 \end{bmatrix} \rightarrow \vec{v}_1 = \begin{bmatrix} \dot{q}_1 R \\ 0 \\ 0 \end{bmatrix}, \quad \vec{w}_1 = \begin{bmatrix} 0 \\ 0 \\ \dot{q}_1 \end{bmatrix} \tag{5.1}$$

The pendulum is attached to the center of the sphere and it can be approximated as a point mass with a constant distance from the sphere center equal to l. Its position depends on the sphere center position and on the lifting angle described by q_2. The equation describing the pendulum kinematics are the following ones:

$$\vec{r}_2 = \begin{bmatrix} q_1 R + l s_2 \\ R - l c_2 \\ 0 \end{bmatrix} \rightarrow \vec{v}_2 = \begin{bmatrix} \dot{q}_1 R + l c_2 \dot{q}_2 \\ l s_2 \dot{q}_2 \\ 0 \end{bmatrix}, \quad \vec{w}_2 = \begin{bmatrix} 0 \\ 0 \\ \dot{q}_2 \end{bmatrix} \tag{5.2}$$

where l is the distance of the pendulum barycenter from the sphere center, c_i and s_i are the cosine and the sine of the generalized variable q_i, respectively.

5.2.2 Two-Dimensional Dynamics

The dynamic model was obtained through the Lagrangian Approach. The Lagrangian function is defined as:

$$L(q, \dot{q}) = K(q, \dot{q}) - P(q) \tag{5.3}$$

where K and P are the total kinetic and potential energy of the system, respectively. This function is used to obtain the n differential equations describing the problem, where n is the number of generalized coordinates. In this case, two generalized coordinates have been used, therefore two differential equations are sufficient to describe the problem. Their form is the following one:

$$\frac{d}{dt}\left(\frac{\partial L(q, \dot{q})}{\partial \dot{q}_i}\right) - \frac{\partial L(q, \dot{q})}{\partial q_i} = F_i^{nc}(q) \tag{5.4}$$

where $F_i^{nc}(q)$ are called generalized forces, and they are the non conservative forces acting along the i-th coordinate.

The total kinetic energy of the system composed by the sphere and the pendulum is computed as:

$$K = \frac{1}{2} M v_1^2 + \frac{1}{2} m v_2^2 + \frac{1}{2} I \omega_1^2 + \frac{1}{2} I_p \omega^2 \tag{5.5}$$

where m and M are the pendulum and sphere masses respectively; I is the total inertia of the sphere, while I_p is the total inertia of the pendulum. Substituting the vectors describing the kinematics of the problem obtained in 5.1 and 5.2, the total kinetic energy has the form:

$$K = \frac{1}{2}\dot{q}_1^2\left(mR^2 + MR^2 + I\right) + \frac{1}{2}\dot{q}_2^2(ml^2 + I_p) + mRl\dot{q}_1\dot{q}_2\ c_2 \tag{5.6}$$

The potential energy of the system is described by the following equation:

$$P = -m\vec{g}\cdot\vec{r_1} - m\vec{g}\cdot\vec{r_2} \tag{5.7}$$

Where $\vec{g}$ is the gravitational acceleration vector expressed in the fixed reference system of fig. 5.1:

$$\vec{g} = -g\begin{bmatrix} sin(\alpha) \\ cos(\alpha) \\ 0 \end{bmatrix} \tag{5.8}$$

Substituting the position vectors of the sphere and the pendulum, the potential energy of the system results:

$$P = g\left[M\left(q_1Rs_\alpha + Rc_\alpha\right) + m\left(q_1Rs_\alpha + Rc_\alpha + ls_2s_\alpha - lc_2c_\alpha\right)\right] \tag{5.9}$$

Replacing the equations 5.6 and 5.9 in 5.3, the Lagrangian function is obtained and it is written down as follows:

$$\begin{aligned} L &= \tfrac{1}{2}\dot{q}_1^2\left(mR^2 + MR^2 + I\right) + \tfrac{1}{2}\dot{q}_2^2(ml^2 + I_p) + mRl\dot{q}_1\dot{q}_2\ c_2 + \\ &\quad + g\left[M\left(q_1Rs_\alpha + Rc_\alpha\right) + m\left(q_1Rs_\alpha + Rc_\alpha + ls_2s_\alpha - lc_2c_\alpha\right)\right] \end{aligned} \tag{5.10}$$

This function is finally used to calculate the two differential equations describing the system using eq. 5.4:

$$\begin{cases} \ddot{q}_1\left(I_n\right) + \ddot{q}_2\left(mRlc_2\right) - \dot{q}_2^2\ mRls_2 + \beta_1\dot{q}_1 + Rs_\alpha g\left(M + m\right) = \tau_M - \tau_{ext,1}^{nc} \\ \\ \ddot{q}_1\left(mRlc_2\right) + \ddot{q}_2\left(ml^2 + I_p\right) + mgl\left(s_\alpha c_2 + \beta_2\dot{q}_2 + c_\alpha s_2\right) = \tau_M - \tau_{ext,2}^{nc} \end{cases} \tag{5.11}$$

where τ_M is the motor torque, τ_{ext}^{nc} are the torques due to external non-conservative forces, I_n is equal to $I_n = mR^2 + MR^2 + I$, and β_1 and β_2 are the viscous friction coefficients used to account for the friction dissipation.

These equations don't account for the effect of the gyroscopic torque because they were used to study the straight-line-movement of the robot, but it could be included subtracting the gyroscopic torque in the right hand side of the second equation.

5.3 Multibody Model in Simscape Simulink

Before assembling a prototype, it is crucial to conduct a comprehensive evaluation of the design and overall performance of the system. This evaluation aims to minimize the potential issues that may arise during the prototype realization phase. For this reason, a detailed model that is able to faithfully describe the behavior of the system needs to be developed. An analytical model could predict a well approximated response to certain inputs. However, it is challenging to realize an accurate mathematical description of a complex system. To obtain a more comprehensive representation, multibody dynamical simulations can be employed. Consequently, a multybody model of the SR was realized. For this purpose, the CAD files of the SR components designed in Solidworks were used to develop a simulation of the system in the Simscape Simulink environment. By using this approach, an accurate depiction of the robot is achieved, allowing to simulate the motion, forces, and torques experienced by the SR during its operation. By setting up the appropriate physical parameters of each component, such as mass and inertia, it is possible to accurately replicate the robot's behavior in a virtual environment. Stability, energy consumption, and control system effectiveness can be studied, aiding in the refinement and optimization of its design.

5.3.1 Description of the block scheme

A screenshot of the SR assembled in the Simscape environment is presented in figure 5.2. Each element (body) of the robot was imported in the Simulink environment as a STEP file. Each component possesses a default reference system, though additional reference systems can be generated as needed to establish connections

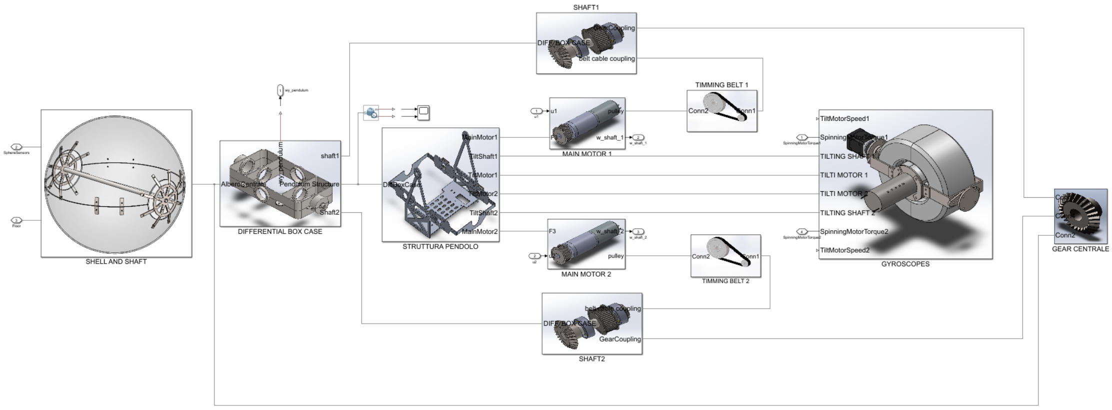

Figure 5.2: Screenshot of the Simscape environment with the SR.

between elements within the system. A simple connection between two reference systems will arrange the two components in such a way that the frame axes coincide and no relative motion is allowed. If joint connections are needed, specific blocks must be placed in between the reference systems of the two elements. The joint block must be chosen depending on the number of DOFs that the adjoining bodies share. An example is shown in figure 5.3. Here, the blue lines represents simple connections between the components, while the block framed in yellow is an example of "revolute joint", which allows one rotational degree of freedom between the two connected blocks (the motor gearbox and the pulley). If the two connected blocks represent an actuated component and a motor, like in fig. 5.3, the torque provided by the actuator must be input to the specific torque port of the joint block.

All the Simscape simulations need three main blocks from which all the connections branch off: the "Solver Configuration", where the simulation parameters are specified, the "Mechanism Configuration", where the gravity vector is defined, and the "World Frame".

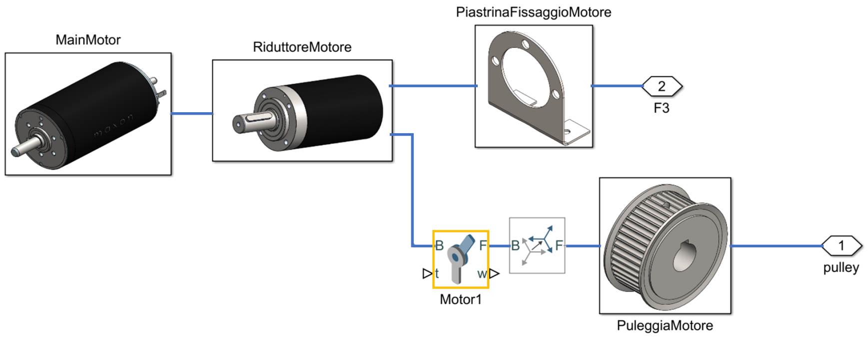

Figure 5.3: Screenshot of the Simscape environment: detail of the connections between components. Simple connections in blue and the kinematic constraint block in yellow.

5.3.2 Interaction between the ground and the sphere

In order to allow the sphere to move freely in the space, it must be connected to the world frame with a six DOFs joint block. To simulate the interaction between the floor and the spherical shell of the robot, two possible solutions can be adopted. The first one consists of using the built-in block responsible to compute the spatial contact forces. It doesn't require to specify anything, and the stiffness and damping, as well as the friction coefficients, can be modified from the block interface.

A second possible solution exploits the external library developed by Steve Miller [45], which was the same one used in [1]. A "sphere-to-plane force" block is responsible for computing the interaction forces between the spherical shell and the plane. In this block, the sphere radius and the plane dimension must be specified. The coefficients used to determined the forces at play can be modified as in the built-in bock.

Both options are valuable; however, the Spatial Contact Force provides a simpler approach for simulating contact forces, particularly with more complex surfaces, without the need for any additional downloads. For Simulink versions that don't support the Spatial Contact Force block, the library from reference [45] offers a suitable solution.

An example of the blocks needed to simulate a sphere on the plane is shown in fig. 5.4. A two-DOF joint was used to allow the tilting of the plane around the x and y axes.

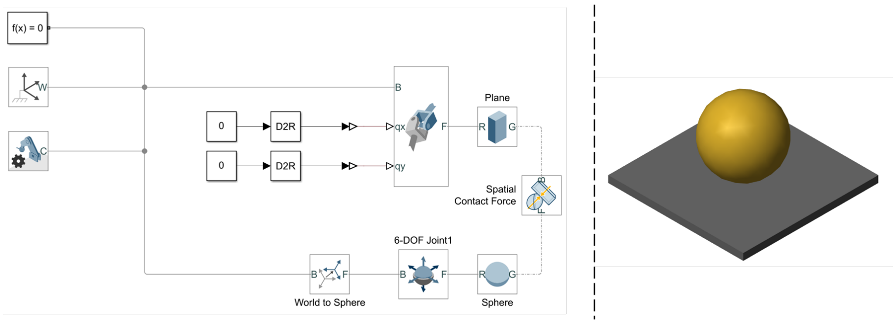

Figure 5.4: Screenshot of the Simscape environment: on the left the blocks used to simulate the sphere on the plane; on the right, the visual representation of the system.

5.3.3 Step obstacle

To implement a step in the simulated environment, it can be accomplished by adding a solid object on the top of the floor and establishing a connection between it and the sphere using a new spatial contact force block. This approach enables the simulation to accurately replicate the interaction between the sphere and the step, allowing for a realistic representation of the scenario.

If an older version of Simulink is used and this block is not supported, a solution is presented in [1]. The step can be simulated through a cylinder with a very small radius and two parallelepipeds, as shown in fig. 5.5. A "sphere-to-tube force" block from the library [45] needs to be used to simulate the contact at the edge of the step, while another "sphere-to-plane force" block is used to simulate the contact between the sphere and the plane at the top of the step.

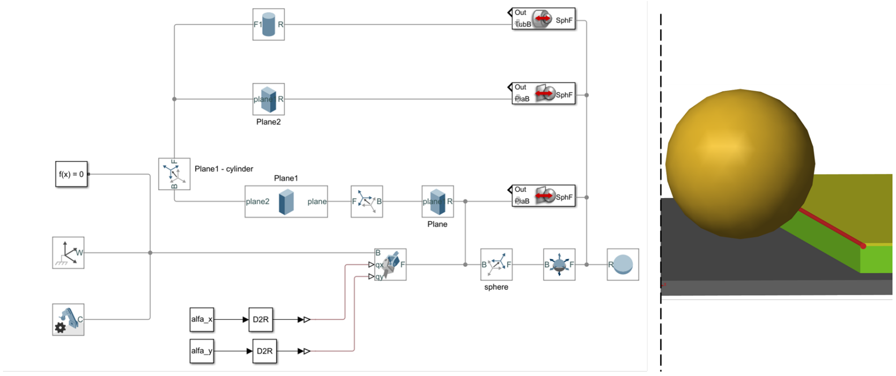

Figure 5.5: Screenshot of the Simscape environment: on the left the blocks used to simulate the sphere on a plane with a step; on the right, the visual representation of the system.

5.3.4 Model of the DC motors

As previously discussed, the "File Solid" blocks offer the ability to define the inertia and geometric properties of the bodies. However, if the block represents a motor, it is not possible to directly specify the output torque within its "File Solid" block. In such cases, it is necessary to create a dedicated model for the motor, wherein the output torque is generated. This torque is then inputted into the torque port of the revolute joint that is associated with the motor. In the next paragraphs it will be explained how to realize the model of a dc-brushed motor.

Motor torque

Consider a single coil pivoted about its vertical axis and run by current, as show in fig. 5.6. If the coil is placed inside a magnetic field, it will start to spin around its vertical axis. This phenomenon is described by the Ampère's law and the torque

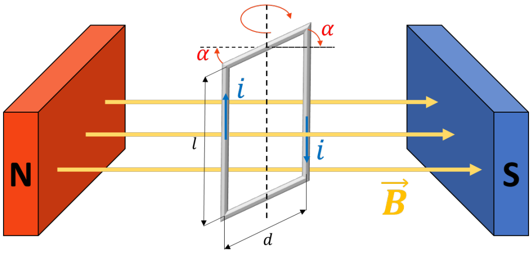

Figure 5.6: Coil run by current in a magnetic field.

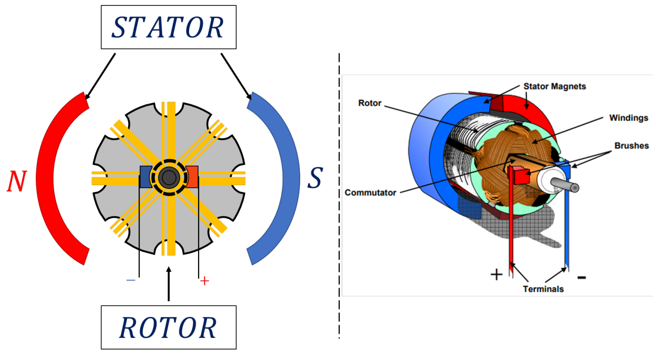

Figure 5.7: Stator and rotor scheme of a DC motor.

acting on the coil is described by the following equation:

$$\tau = ilB\ d\ cos(\alpha) \tag{5.12}$$

where i is the current going through the coil, B is the magnetic field intensity, l is the length of the vertical branch of the coil, d is the length of the horizontal branch of the coil, and α is the rotation angle between the coil and the magnetic field as depicted in fig. 5.6.

Looking at equation 5.12, it can be noted that the torque is not constant and it depends on the position of the coil: between $-\frac{\pi}{2}$ and $\frac{\pi}{2}$ it is positive, while it is negative from $\frac{\pi}{2}$ to $-\frac{\pi}{2}$. To develop a torque with a constant sign the current flowing through the coil must change its direction when α is equal to a multiple of 90°. This can be done connecting the coil to a commutator, which is a device composed by 2 separate segments attached to the loop. Spring-loaded brushes sit on each side of the commutator and make contact with the commutator as it turns, supplying the coil with voltage. This solution allows only to have a torque with a constant sign, but not with a constant value. This issue can be solved by increasing the number of coils in such a way that the loop supplied with voltage is the one with the α closest to $\pm\frac{\pi}{2}$.

This structure is at the basis of the brushed DC motors. Here, the coils are wounded around what is called the armature core 5.7. The armature is also known as the rotor, which is the rotating part of the motor, while the stator or field identifies the stationary part of the motor.

The magnetic field is usually generated through an electromagnet, which is a solenoid supplied with current. The intensity of the magnetic field inside a solenoid can be calculated though the equation 5.13:

$$B = \mu\ n\ I_{sol} \tag{5.13}$$

where μ is the magnetic permeability of the dielectric inside the solenoid, n is the coil density and it is calculated as the number of loops over the length of the solenoid N/L, while I_{sol} is the current flowing through the solenoid.

With this information, the equation 5.12 can be rewritten as follows:

$$\tau_M = i_a l d \left(\mu \frac{N}{L_{sol}} i_f \right) \tag{5.14}$$

where i_a and i_f are the armature and field current, respectively. This equation is usually written in another form, which exploits the equation of the flux of a solenoid:

$$\Phi = \frac{\mu \cdot A_{sol}}{L_{sol}} N \ i_f = K_0 \ N i_f \tag{5.15}$$

where $K_0 = \mu \cdot A_{sol}/L_{sol}$.

By replacing this last equation in 5.14, the motor torque results:

$$\tau_M = \left(\frac{ld}{A_{sol}} K_0 N \right) i_a i_f = K \ i_a i_f \tag{5.16}$$

Electric equations of the motor

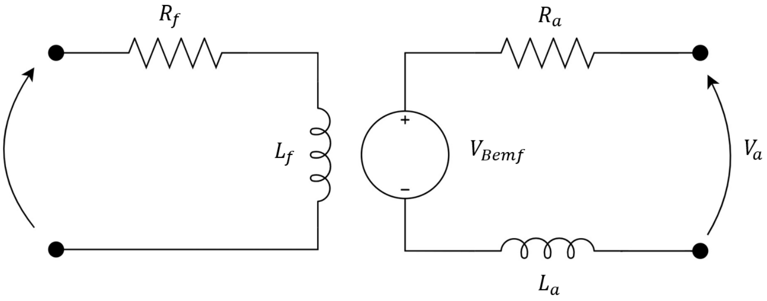

Figure 5.8: Electrical diagram of the motor.

Consider a brushed-dc motor where the stationary magnetic field is generated by an electromagnetic windings. The electrical circuit of the motor is depicted in fig. 5.8. The left part of the circuit represents the stator (field). The transfer function of the stator can be written down as:

$$\frac{I_f(s)}{V_f(s)} = \frac{1/R_f}{1 + s \cdot L_f/R_f} \tag{5.17}$$

The rotor (armature) circuit is the one on the right of fig. 5.8. The V_{Bemf} is the voltage generated by the back electromotive force (EMF), which opposes the change in the flux due to rotor movement. It is computed as:

$$V_{Bemf} = -\frac{d\Phi}{dt} = -\frac{d}{dt}\left(BA\ cos\left(\theta(t)\right)\right) = BA\ sin\left(\theta(t)\right)\omega \tag{5.18}$$

where ω is the angular speed of the rotor, and θ is equal to $\alpha + \frac{\pi}{2}$. In the precious paragraph it was stated that α can be approximated to zero; consequently, θ results to be always $\frac{\pi}{2}$. Substituting eq. 5.13 and 5.15 in the V_{Bemf}, the back EMF voltage can be written down as:

$$V_{Bemf} = Ki_f\omega \tag{5.19}$$

where K is the same used to compute the motor torque.

Finally, the transfer function of the armature circuit can be computed and it results:

$$\frac{I_a(s)}{V_a(s) - V_{Bemf}(s)} = \frac{1/R_a}{1 + s \cdot L_a/R_a} \tag{5.20}$$

Mechanical equations of the motor

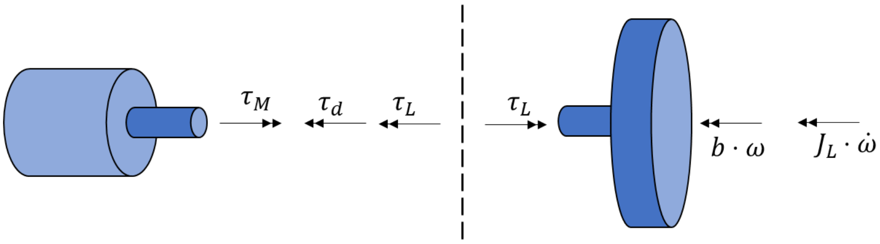

Figure 5.9: Mechanical diagram of the motor.

The mechanical equations of the motor attached to the load can be obtained from the diagram of fig. 5.9. In particular, the transfer function of the motor angular speed is the following one:

$$\frac{\omega(s)}{\tau_M(s) - \tau_d(s)} = \frac{1/b}{1 + s \cdot J_L/b} \tag{5.21}$$

Diagram of a DC-brushed motor

From the equations 5.17, 5.20, and 5.21, the block diagram of fig. 5.10 is obtained. This diagram models the functioning of a general brushed DC motor. A common adopted solution to control the motors is the armature current control. This control technique consists in maintaining constant the flux of the magnetic field inside the motor, and control the motor torque through the armature current. To keep the flux constant, the stator voltage V_f, and therefore the stator current i_f, are kept constant. This control technique changes the block diagram of the motor as shown in fig. 5.11. It can be noted that the non linearity introduced by the product of the two currents (i_a and i_f) here is eliminated.

This model is the one that was implemented in the Simscape Simulink model. The values used were taken from the catalogues of the selected motors.

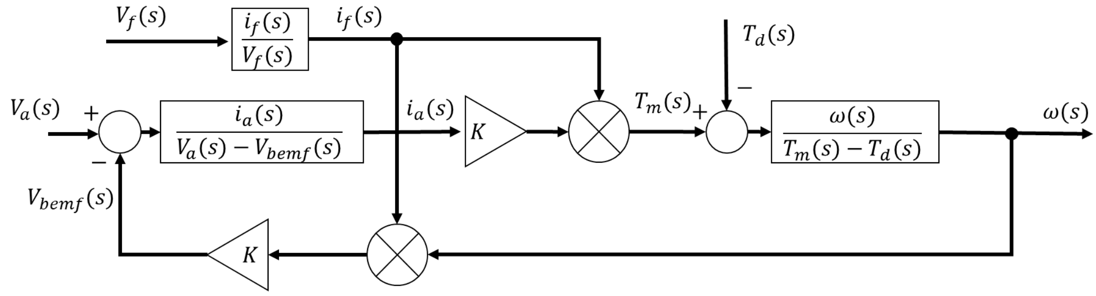

Figure 5.10: Block diagram of a general brushed-DC motor.

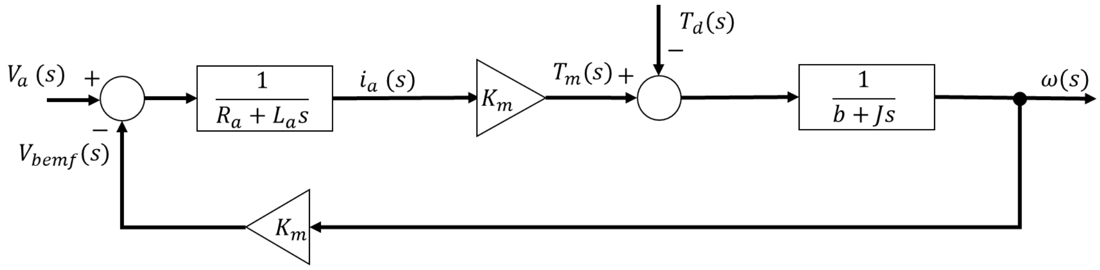

Figure 5.11: Block diagram of an armature current controlled brushed-DC motor.

Chapter 6

Testing of the Simulations

6.1 Introduction

The modeling of a robotic system is crucial because it allows to study the robot dynamics, evaluate the overall performance of the system, and minimize the potential issues that may arise during the prototype realization phase. In the previous chapter, the analytic two dimensional model and the multibody simulation of the robot were presented, outlining the process involved in their creation. In the subsequent sections, the simulation environments will undergo testing and verification to ensure their accuracy and reliability. Specifically, the behavior of the robot will be compared to the one that was theorized in the previous chapters, verifying the kinematic relations and the robot dynamics when using the gyroscopes.

6.2 Testing the Differential System Kinematics

To test the correct assembling of the pendulum in the simulation environment, the functioning of the differential driving system was assessed, ensuring the validity of the kinematic equations 4.1 and 4.2. For clarity and improved comprehension, the equations are restated below:

$$\omega_3 = \frac{\omega_1 - \omega_2}{2} - \omega_p$$

$$\Omega = \frac{\omega_1 + \omega_2}{2} - \Omega_p$$

The tests were performed inputting precise speed and torque curves in the motor joints of the multibody simulation.

6.2.1 Rolling in the Forward Direction

The first test consisted in verifying that the robot follows a straight path when the speed of the main motors is the same. In fact, the relative speed between the pendulum and the main shaft about the x-axis[1] can be computed through eq. 4.2, and it results equal to zero:

$$\Omega + \Omega_p = 0 \tag{6.1}$$

The relative speed between the pendulum and the central shaft about the y-axis can be computed through eq. 4.1 and it's equal to the reduced angular velocity of the motors:

$$\omega_3 + \omega_p = |\omega_1| \tag{6.2}$$

Note that ω_3 coincides with the angular velocity of the spherical shell. The graphs below depict the reduced angular speeds of the motors (fig. 6.1 on the left), the sphere velocity measured about the Y-axis of the world frame and computed through eq. 4.1 (fig. 6.1 on the right), and the path followed by the SR (fig. 6.2).

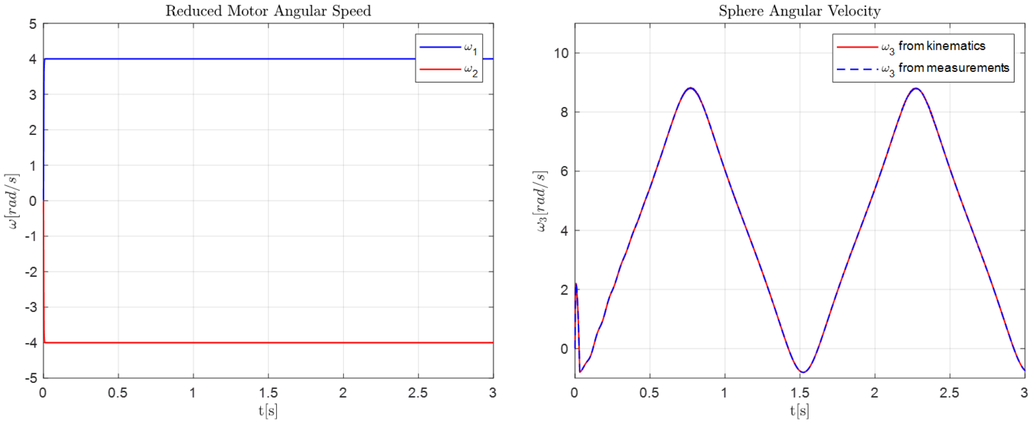

Figure 6.1: On the left: angular speeds of the motors. On the right: the sphere velocity measured about the Y-axis of the world frame and computed through eq. 4.1.

---

[1]: to have a better understanding refer to fig. 4.1. Note that the x and y axis of the figure are not the ones of the World frame, therefore the velocities ω_3, ω_p, Ω, and Ω_p aren't refereed to the World frame, except for particular cases, like the one of the first test performed.

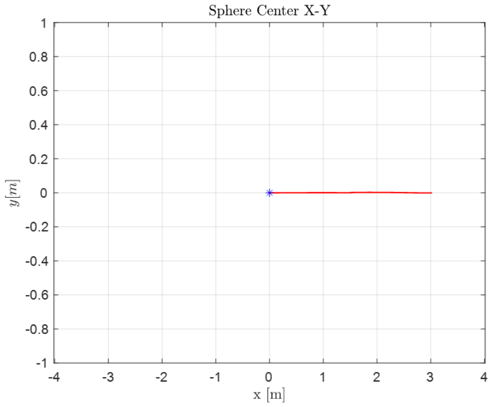

Figure 6.2: Path followed by the SR.

6.2.2 Providing Different Torque to the Motors

In the second test, two constant torques with values 1 Nm and 2 Nm were provided to the two motor joints. This time, the relations 4.1 and 4.2 were verified measuring directly the relative angular velocities between the pendulum and the main shaft about the x and y axes, which are equal to $\omega_3 + \omega_p$ and $\Omega + \Omega_p$, respectively. This can be done through the joint blocks inside the simulation, which allow to measure the relative speed of the reference systems connected.

In fig. 6.3 the graphics of the path followed by the sphere (left), and the reduced angular speeds of the motors (right) are shown. Figure 6.4 shows the validity of the two kinematic equations, where the measured and computed values perfectly overlap. Specifically, the red lines represent the relative velocities computed through the motors speeds, while the dashed blue lines represent the measured relative velocities.

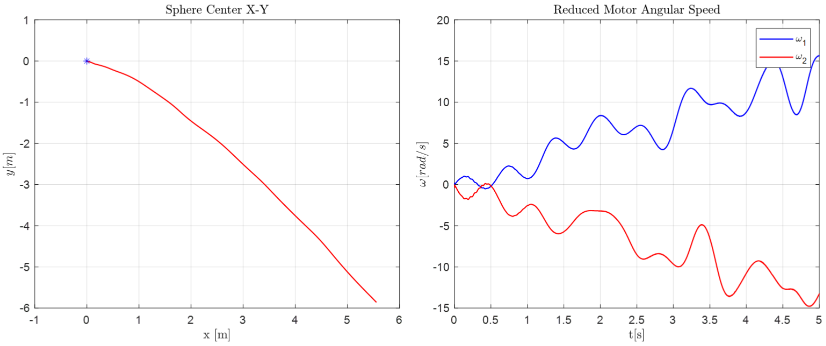

Figure 6.3: Graphics of the path followed by the sphere (left), and the reduced angular speeds of the motors (right).

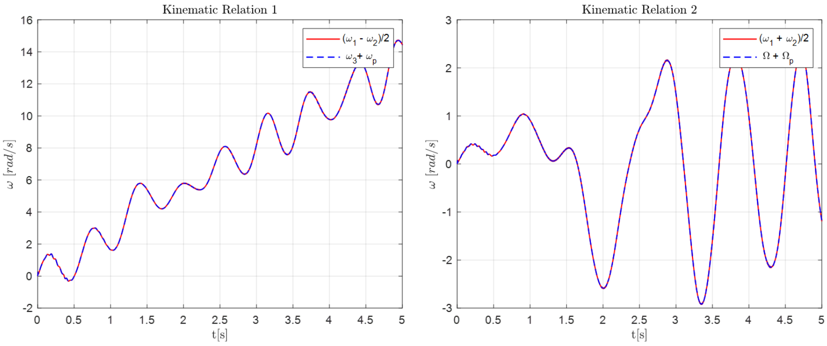

Figure 6.4: On the left: relative velocities about y-axis computed through the motors speeds (red) and measured (blue). On the right: relative velocities about x-axis computed through the motors speeds (red) and measured (blue).

6.3 Tuning the Analytical Model Parameters

After confirming the proper functioning of the differential driving system in the multibody simulation, a simulation of the 2D analytical model was realized (fig. 6.5). During this simulation, careful parameter tuning was performed by comparing the obtained results with those derived from the multibody simulation when providing to each motor joint a constant 1 Nm torque. This step was crucial because the control of the forward motion of the system was developed on the basis of this analytical model.

The obtained results are listed in table 6.1. In figure 6.6 the angular displacement (left) and velocity (right) of the pendulum in the multibody (red curve) and in the analytical model (blue dashed curve) are shown. Fig. 6.7 represents the same variables referred to the sphere. The curves do not perfectly overlap, but this is due to the simplifications made in the analytical model, in which the system is described as a sphere and a simple pendulum with no friction with the plane.

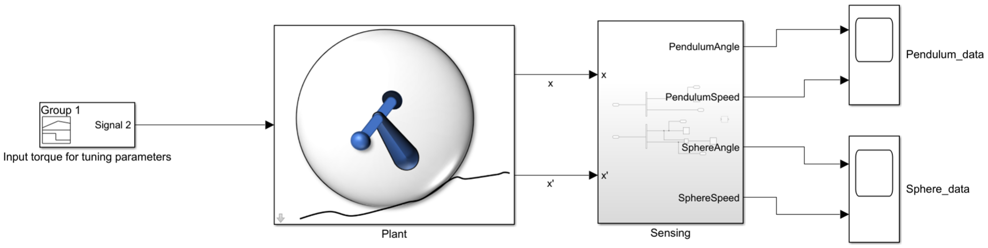

Figure 6.5: Simulink simulation of the 2D analytical model of the pendulum.

2D ANALYTICAL MODEL PARAMETERS		
M	$5\ kg$	Sphere mass
m	$13.2\ kg$	Pendulum mass
l	$0.12\ m$	Pendulum barycenter from the sphere center
R	$0.25\ m$	Sphere radius
I_p	$0.07\ kg\ m^2$	Pendulum inertia
I_{sf}	$0.11\ kg\ m^2$	Sphere inertia

Table 6.1: 2D analytical model parameters.

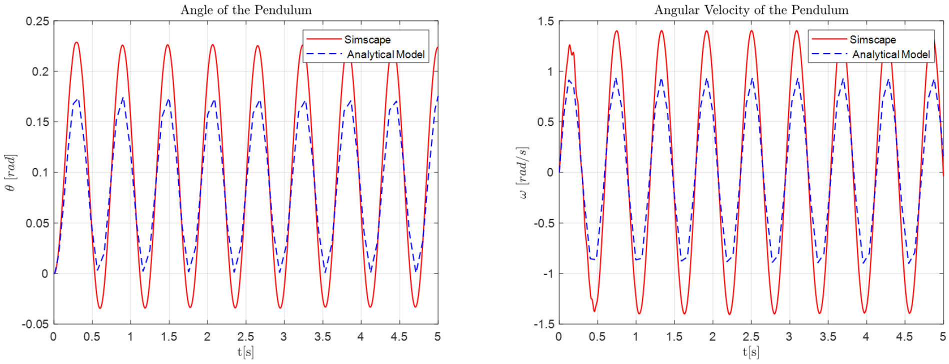

Figure 6.6: Angular displacement (left) and velocity (right) of the pendulum in the multibody (red curve) and in the analytical model (blue dashed curve). Total input torque: 2 Nm. Angle of the plane: 0°.

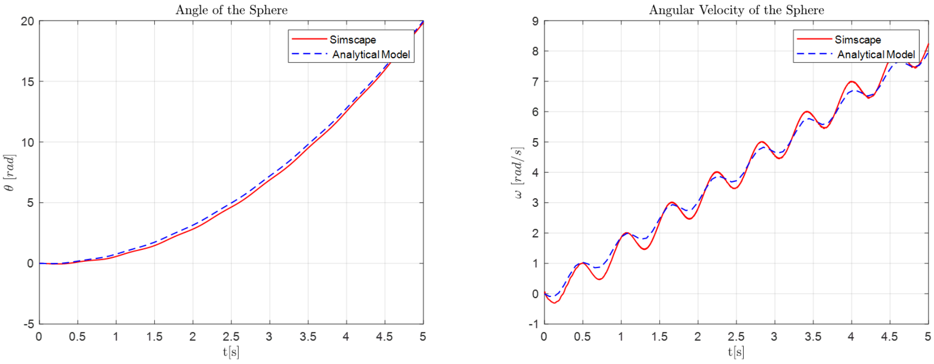

Figure 6.7: Angular displacement (left) and velocity (right) of the sphere in the multibody (red curve) and in the analytical model (blue dashed curve). Total input torque: 2 Nm. Angle of the plane: 0°.

The model was verified also for the case of a SR rolling on an inclined plane. The graphics from fig. 6.8 and 6.9 represent the same curves of fig. 6.6 and 6.7 obtained when the plane has an inclination of 5° and a constant torque of 1 Nm is provided to each motor joint.

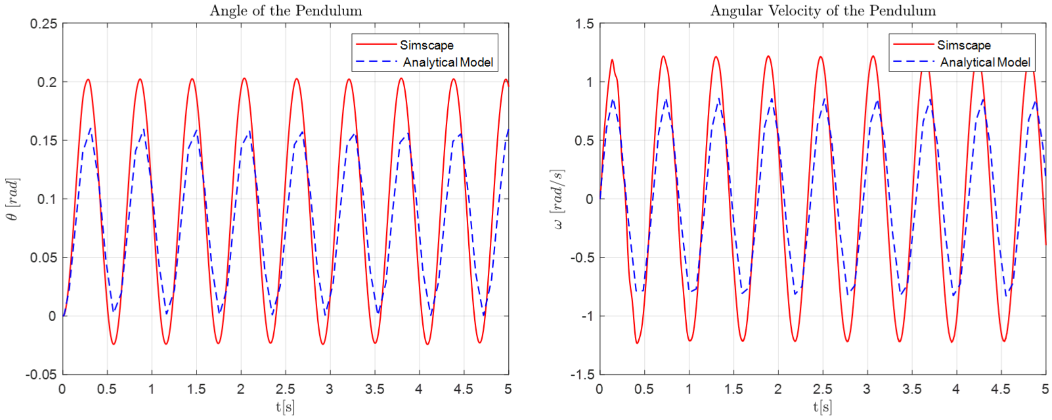

Figure 6.8: Angular displacement (left) and velocity (right) of the pendulum in the multibody (red curve) and in the analytical model (blue dashed curve). Total input torque: 2 Nm. Angle of the plane: 5°.

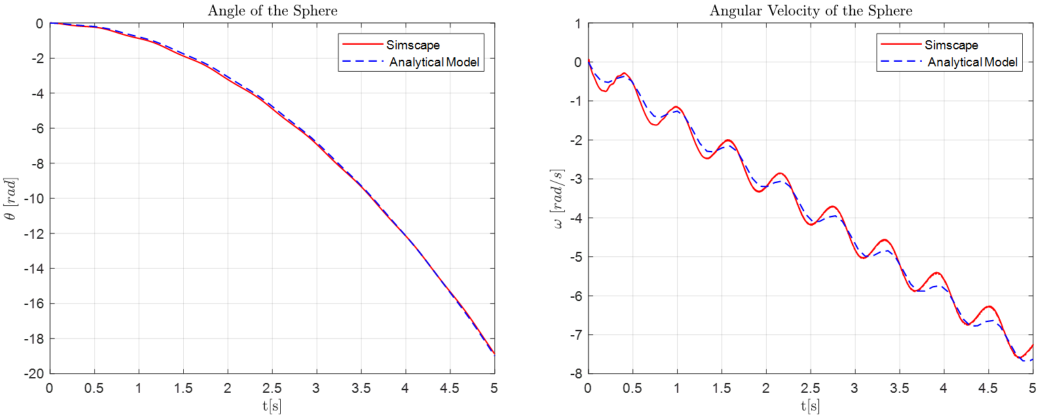

Figure 6.9: Angular displacement (left) and velocity (right) of the sphere in the multibody (red curve) and in the analytical model (blue dashed curve). Total input torque: 2 Nm. Angle of the plane: 5°.

6.4 Testing the CMG group

After verifying the correct functioning of the differential mechanism in the multibody simulation, and tuning the analytical model parameters, the CMG was tested to ensure that the robot would behaves as expected when using the gyroscopes. Specifically, another simulation was created to compare the dynamics of the multibody simulations with the one expected from the differential equations 5.11. As already mentioned, those equations don't account for the effect of the gyroscopic torque, but it can be included by subtracting the gyroscopic torque to the right hand side of the second equation:

$$\begin{cases} \ddot{q}_1\left(mR^2+MR^2+I\right)+\ddot{q}_2\left(mRlc_2\right)-\dot{q}_2^2\,mRls_2+Rs_\alpha g\left(M+m\right)=\tau_M \\ \\ \ddot{q}_1\left(mRlc_2\right)+\ddot{q}_2\left(ml^2+I_p\right)+mgl\left(s_\alpha c_2+c_\alpha s_2\right)=\tau_M-\tau_G \end{cases} \tag{6.3}$$

In these tests, the effect of external and dissipative forces wasn't considered.

To perform the tests, it was provided a torque curve to each motor joint of the Simscape simulation equal to half the gyroscopic torque generated when spinning the flywheels at 1000 rpm and tilteing them at speed of 15 rpm. In such a way, τ_M results equal to τ_G, and the gyroscopic torque is directly transferred to the sphere. A graphic representing the total input torque is shown in fig. 6.10. To simulate the analytical model, the differential equations were written in Matlab and were solved through the numerical integration "4^{th} Order Runge-Kutta" algorithm. As it was done for the previous tests, the curves from the two simulations were overlapped to highlight the differences (fig. 6.11 and 6.12). As already noticed for the results

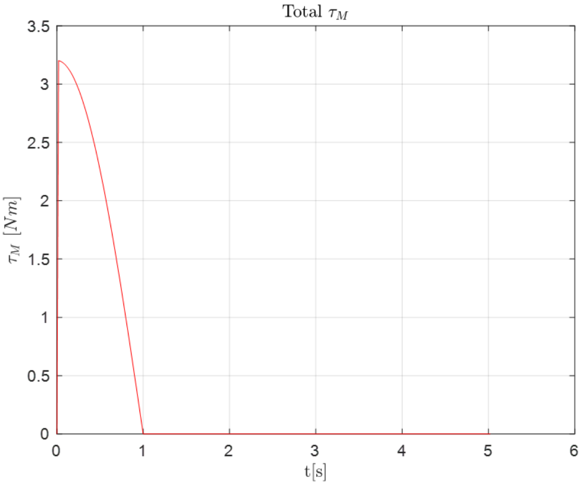

Figure 6.10: Total torque provided by the motors τ_M.

of the previous tests, the curves do not perfectly overlap due to the simplifications made in the analytical model, but it can be observed that the behavior of the robot is well described by the analytical equations and the gyroscopes work as expected.

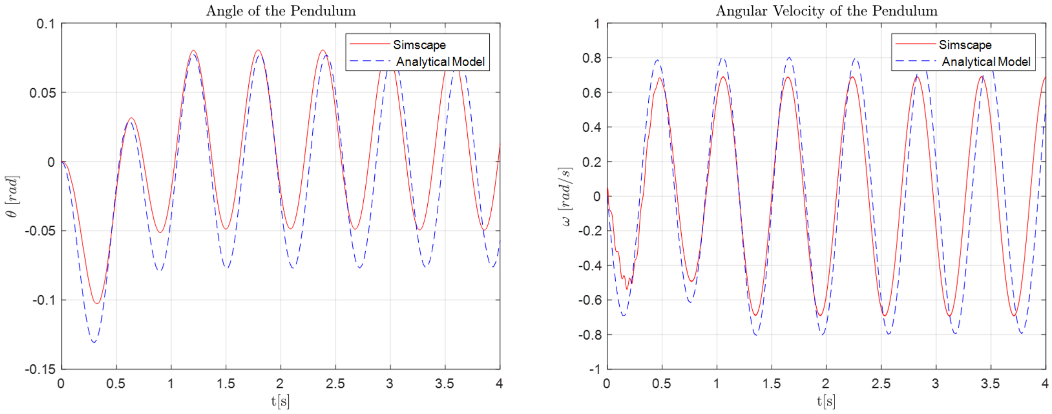

Figure 6.11: Angular displacement (left) and velocity (right) of the pendulum in the multibody (red curve) and in the analytical model (blue dashed curve). Total input torque: 2 Nm. Angle of the plane: 5°.

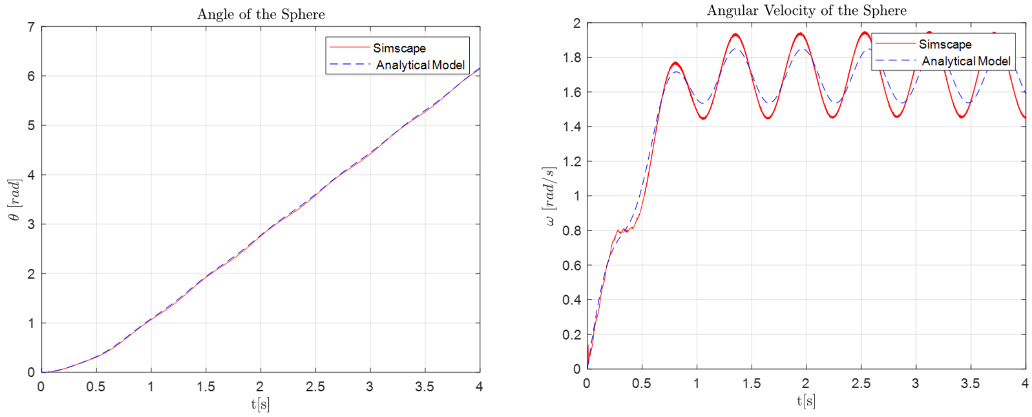

Figure 6.12: Angular displacement (left) and velocity (right) of the sphere in the multibody (red curve) and in the analytical model (blue dashed curve). Total input torque: 2 Nm. Angle of the plane: 5°.

Chapter 7

Control System Design

7.1 Introduction

In the last two chapters, the models used to simulate the robot were presented and tested. A more comprehensive and accurate model of the SR was achieved through the multibody simulation. The correct functioning of the differential driving system and the CMG group in the simulation environment were assessed, showing that the system behaves as expected from the theory. A second model was developed based upon the analytical equations that were obtained through the Lagrangian approach in chapter 5. This analytical model was fine-tuned to yield consistent simulation results with the multibody model.

In this chapter, two control architectures are presented. Their aim consists in ensuring an accurate tracking of the input speed of the spherical robot along a straight path on an inclined plane. The first control system was designed based on the analytical model of the robot, which was linearized to enable the utilization of classical control techniques. It was subsequently applied on the multibody model and tested within the multibody simulation environment.

The second control system was directly designed and tested on the multibody simulation.

7.2 Linearization of the Analytical Model

This paragraph provides an explanation of the methodology employed to obtain the linearization of the analytical model. The result will be used in the next sections to study the behavior of the SR system for control purposes.

To linearize the analytical model, first the equilibria points must be found. To obtain them, it is sufficient to impose all the derivatives of the generalized coordinates equal to zero and substitute them in the equations 5.11:

$$\begin{cases} Rs_\alpha \left(M+m\right) g = \tau_0 \\ \\ mgls_\alpha c_{2,0} + mglc_\alpha s_{2,0} = \tau_0 \end{cases} \tag{7.1}$$

The external forces are considered to be equal to zero. From this equations, the angle of the pendulum and the torque needed to maintain the system in equilibrium can be computed:

$$\begin{aligned} \tau_0 &= Rs_\alpha \left(M+m\right) g \\ \\ q_{2,0} &= asin\left(Rs_\alpha \tfrac{M+m}{ml}\right) - \alpha \end{aligned} \tag{7.2}$$

From this result it can be observed that infinite equilibrium points can be found, but the angle of interest for this specific application belongs to the $[-\frac{\pi}{2}, \frac{\pi}{2}]$ interval. To simplify the final linearized expression, deviation variables are defined as:

$$\hat{q}_2 = q_2 - q_{2,0} \quad , \quad \dot{\hat{q}}_2 = \dot{q}_2 \quad , \quad \ddot{\hat{q}}_2 = \ddot{q}_2 \quad , \quad \hat{\tau} = \tau - \tau_0 \tag{7.3}$$

This change of variables allow to linearize the system around the origin ($\hat{q}_2 = 0$ and $\hat{\tau} = 0$). These variables were substituted inside equations 5.11. The linearization was realized through Taylor series expansion and the obtained equations are written down below:

$$\begin{cases} \ddot{\hat{q}}_1 \left(mR^2 + MR^2 + I\right) + \ddot{\hat{q}}_2 \left(mRlc_{2,0}\right) + \beta_1 \dot{\hat{q}}_1 = \hat{\tau} \\ \\ \ddot{\hat{q}}_1 \left(mRlc_{2,0}\right) + \ddot{\hat{q}}_2 \left(ml^2 + I_p\right) + \beta_2 \dot{\hat{q}}_2 + mglc_\alpha c_{2,0} \hat{q}_2 = \hat{\tau} \end{cases} \tag{7.4}$$

This equations can be written in matrix form as:

$$\mathbf{H}_l(\mathbf{q})\ddot{\hat{\mathbf{q}}} + \mathbf{C}_l(\mathbf{q}, \dot{\mathbf{q}})\dot{\hat{\mathbf{q}}} + \mathbf{G}_l(\mathbf{q}) = \boldsymbol{M}_l \hat{\boldsymbol{\tau}} \tag{7.5}$$

where

$$\mathbf{H}_l = \begin{bmatrix} mR^2 + MR^2 + I & mRlc_{2,0} \\ mRlc_{2,0} & ml^2 + I_p \end{bmatrix} \quad , \quad \mathbf{C}_l = \begin{bmatrix} \beta_1 & 0 \\ 0 & \beta_2 \end{bmatrix},$$

$$\mathbf{G}_l = \begin{bmatrix} 0 & 0 \\ 0 & mglc_\alpha c_{2,0} \end{bmatrix} \quad , \quad \boldsymbol{M}_l = \begin{bmatrix} 1 \\ 1 \end{bmatrix}.$$

From this equation, the state space representation is obtained and it has the following form:

$$\begin{cases} \dot{\mathbf{x}} & = & \mathbf{Ax} + \mathbf{Bu} \\ \mathbf{y} & = & \mathbf{Cx} + \mathbf{Du} \end{cases} \tag{7.6}$$

where the state variables are

$$\mathbf{x} = \begin{bmatrix} \hat{q}_1 \\ \hat{q}_2 \\ \dot{\hat{q}}_1 \\ \dot{\hat{q}}_2 \end{bmatrix} \quad , \quad \dot{\mathbf{x}} = \begin{bmatrix} \dot{\hat{q}}_1 \\ \dot{\hat{q}}_2 \\ \ddot{\hat{q}}_1 \\ \ddot{\hat{q}}_2 \end{bmatrix} \quad , \quad \mathbf{u} = \hat{\tau}.$$

while the matrices are

$$\mathbf{A} = \begin{bmatrix} \mathbf{0}_{2\times 2} & \mathbf{I}_{2\times 2} \\ & \\ -\mathbf{H}_l^{-1}\mathbf{G}_l & -\mathbf{H}_l^{-1}\mathbf{C}_l \end{bmatrix} \quad , \quad \mathbf{B} = \begin{bmatrix} \mathbf{0}_{2\times 1} \\ \\ \mathbf{H}_l^{-1}\mathbf{M}_l \end{bmatrix}$$

$$\mathbf{C} = \begin{bmatrix} 0 & 0 & 1 & 0 \end{bmatrix} \quad , \quad \mathbf{D} = 0$$

This representation is used in the next sections to study the behavior of the system and realize the control architecture. The block scheme that depicts the linearized plant is shown in fig. 7.1. The transfer function of the linearized plant will be:

$$\frac{Y(s)}{U(s)} = C(sI - A)^{-1}B \tag{7.7}$$

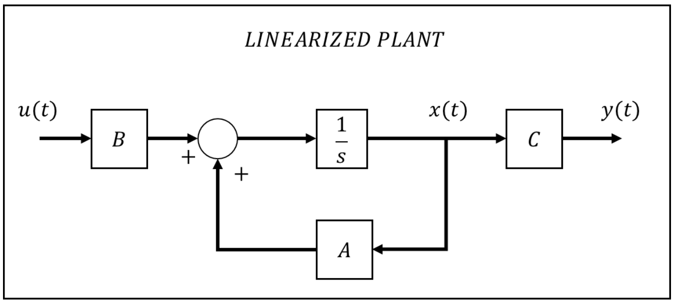

Figure 7.1: Block scheme of the linearized plant.

7.3 Linear Speed Controller with Fuzzy Gain Scheduler

In this section, the first control architecture used to control the SR speed along a straight path is presented. The reference signal is the desired SR rolling speed, which is the angular velocity around the main shaft, and it can be easily computed from the desired linear speed:

$$\omega_s^* = \frac{v_{linear}^*}{R} \tag{7.8}$$

As explained in the previous chapter, to move along a straight path the main motors need to operate at equal and opposite speeds, as deduced from the kinematic equations 4.1 and 4.2. For this reason, a single external speed control loop computes the current reference that will be sent to the two motors. Then, two internal current control loops, one for each motor, are used to track the current reference. By

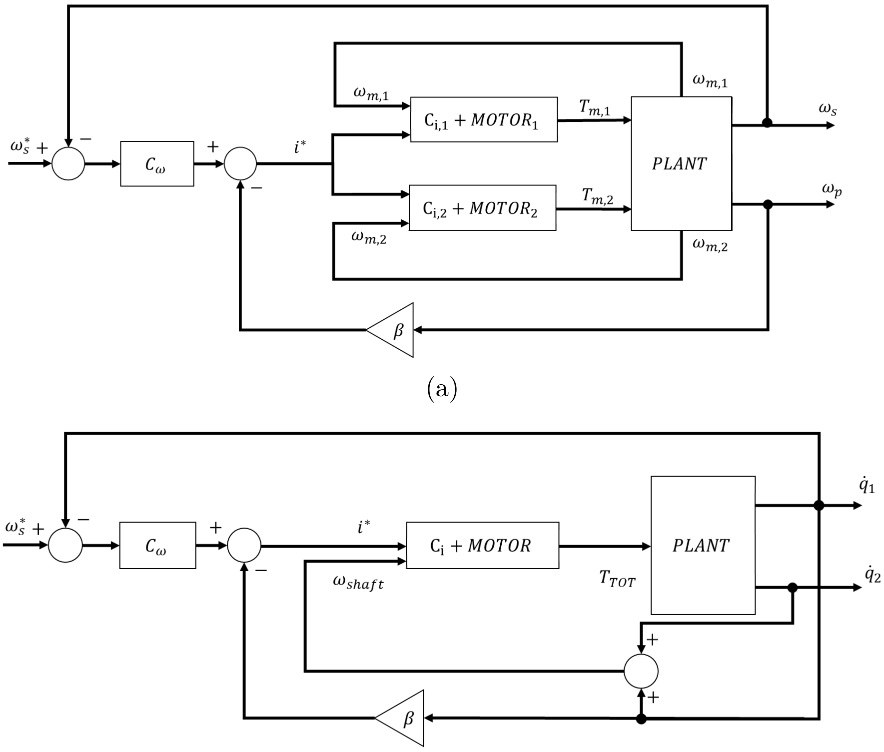

(a)

(b)

Figure 7.2: Block scheme of the system: (a) multibody simulation, (b) analytic simulation.

designing the internal control loops to exhibit faster dynamics compared to the external loop, the motor dynamics have minimal influence on the overall system.

Figure 7.2(a) depicts the block diagram scheme of the system simulated in the multibody simulation. However, the control architecture was designed using the analytic model, where only one motor was simulate and its output was then doubled. This simplification was justified by the fact that the two motors output are expected to be the same. The block diagram scheme depicting the analytical model is shown in fig. 7.2(b). Note that, to calculate the motor speed (ω_{shaft}), the eq. 4.1 is used, and therefore the sphere and the pendulum angular velocities ($\dot{q}_1$ and $\dot{q}_2$ respectively) are summed.

In the next paragraphs, first the internal control loop will be presented, showing that a proper controller makes the transfer function $\frac{i_a(s)}{i_a^*(s)}$ a simple low pass filter with a magnitude of 0 dB. Then, the external control loop is described, explaining its structure and the solution adopted to stabilize the system.

7.3.1 Internal Control Loop

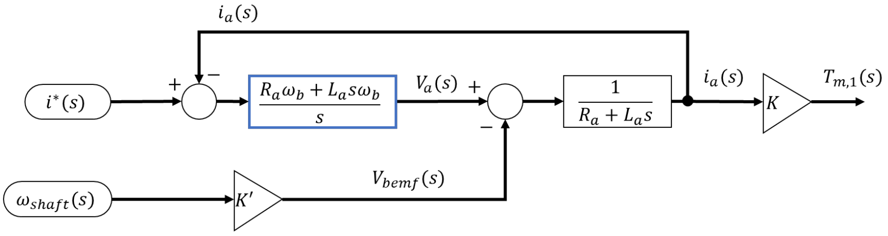

Figure 7.3: Block scheme of the internal control loop.

The internal control loop is responsible for the tracking of the input reference current coming from the external control loop. In fig. 7.3 the current loop block diagram is illustrated. The controller transfer function is the one written inside the blue framed box, while the other one contains the transfer function of the motor. It can be observed that a PI (Proportional-Integrative) controller is used, where the proportional and the integral gain are equal to the armature motor resistance and inductance, respectively, multiplied by a frequency ω_b. The higher this value, the grater the bandwidth of the current loop, which corresponds to a faster response to a step input. The correct values of R_a and L_a can be found in the motor data sheet.

To demonstrate the aforementioned concept, the transfer function of the block scheme depicted in figure 7.3 can be obtained and its Bode representation can be studied. To calculate the transfer function, refer to image 7.4. The plant is described through its linerized transfer function. The gain K is equal to $K = 2K_mK_r\varepsilon$, where

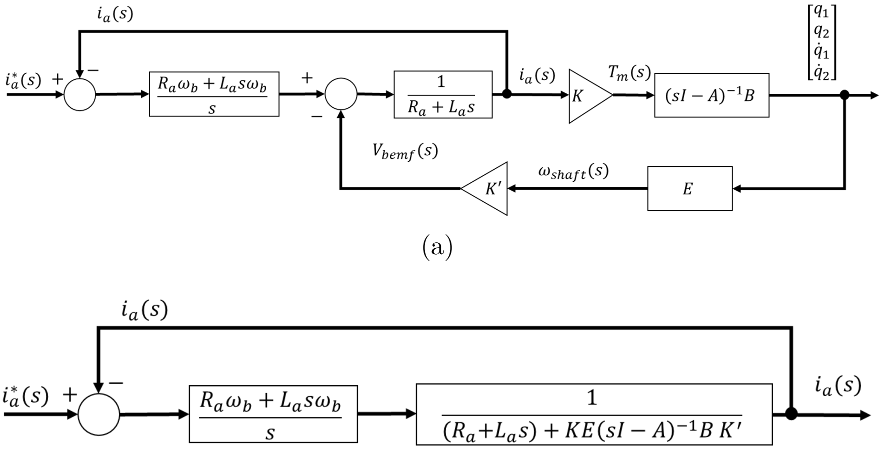

(a)

(b)

Figure 7.4: Block scheme of the internal control loop before reduction (a) and after reduction (b).

K_m is the motor constant, while K_r and ε are the ratio and the efficiency of the gearbox, respectively. The constant K' is equal to $K' = K_m K_r$. The vector E is used to compute the motor shaft speed and it's equal to [0 0 1 1].

The block diagram can be reduced as shown in image 7.4(b). Having defined the block transfer functions as:

$$G_m(s) = \frac{1}{R_a + L_a s + KE(sI - A)^{-1}K'} \tag{7.9}$$

$$C_i(s) = \frac{\omega_b(R_a + L_a s)}{s} \tag{7.10}$$

the negative feedback loop of fig. 7.4(b) can be rewritten as:

$$\frac{i_a(s)}{i_a^*(s)} = \frac{C_i(s)G_m(s)}{1 + C_i(s)G_m(s)} \tag{7.11}$$

In fig. 7.5, the bode plot of transfer function 7.11 is depicted. Observe that, as it was mentioned in the introduction to this chapter, the shape of the magnitude and phase curves are similar to the ones of a low pass filter with a pole in ω_b. The value chosen for the transfer function bandwidth was $\omega_b = \pi \cdot 10^3\ rad/s$. To obtain this plot, a value of 5 $kg\frac{m^2}{s^2}$ was assigned to the viscous friction coefficient β_2.

Thanks to this result, in the next paragraphs the dynamics of the overall system will be studied ignoring the influence of the motors, which it has been shown that starts to be relevant at higher frequencies.

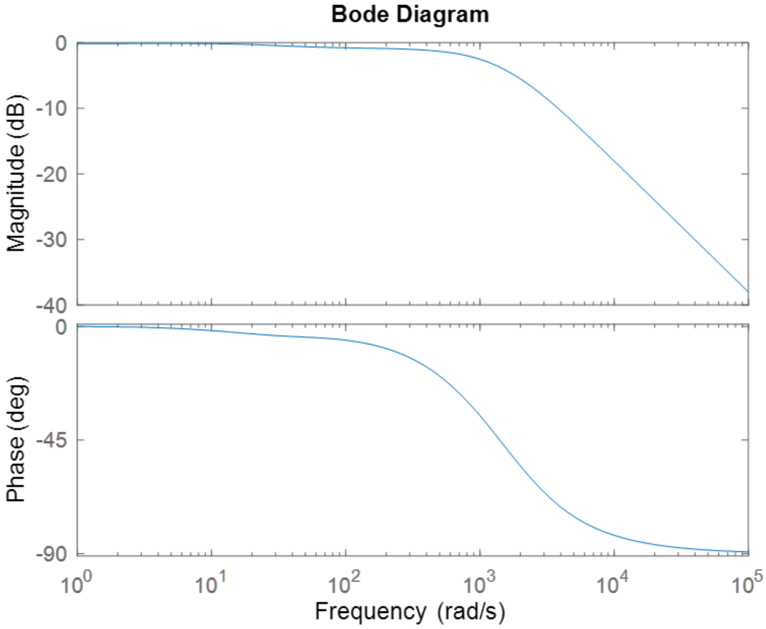

Figure 7.5: Bode plot of the current loop.

7.3.2 External Control Loop

The external control loop is responsible for the SR rolling speed control, which is deduced from the desired linear speed through eq. 7.8. From the previous paragraph conclusions, a new block scheme (fig. 7.6) which represents the system ignoring the motor dynamics can be drawn. It can be noted that the reference armature current is calculated subtracting to the output of the $C_\omega(s)$ block, which in the following is referred as the Speed Controller, the pendulum angular velocity $\dot{q}_2$ multiplied by a constant term β. In the next paragraphs, first this negative feedback is studied, then the Speed Controller block is described.

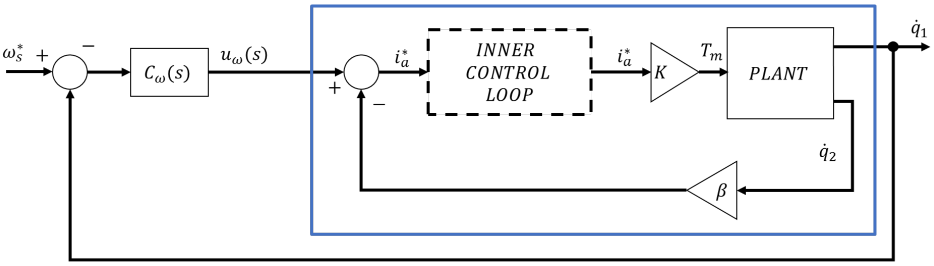

Figure 7.6: Block diagram of the system ignoring the motor dynamics.

The Viscous Friction Problem

The analytical system that has been developed includes the effects of the viscous friction of the pendulum joint and the sphere. The viscous friction is always present in real applications and contributes to the damping of the system. However, it is very difficult to determine the real values of the viscous coefficients β_1 and β_2. A possible solution consists in introducing the viscous friction, along with the Static and the Coulomb ones, as a non-conservative force in the right hand side of the Lagrangian equations 5.11. Anyway, the absence of a damping term causes the model to be unstable. The problem has been solved including the damping effect in the control input, where the pendulum angular speed is multiplied by a constant term β and subtracted to the speed control output. This solution allowed to stabilize the system regardless of the presence of the viscous friction in the plant model.

Referring to fig. 7.6, the input to the plant results equal to:

$$\tau_m = \left(u_\omega - \beta \dot{q}_2\right) K \tag{7.12}$$

The linearized Lagrangian eq. 7.13 of a SR rolling on a flat plane without the viscous friction component can be rewritten as:

$$\begin{cases} \ddot{q}_1 \left(mR^2 + MR^2 + I\right) + \ddot{q}_2 \left(mRl\right) = \left(u_\omega - \beta \dot{q}_2\right) K \\ \\ \ddot{q}_1 \left(mRl\right) + \ddot{q}_2 \left(ml^2 + I_p\right) + mglq_2 = \left(u_\omega - \beta \dot{q}_2\right) K \end{cases} \tag{7.13}$$

It can be observed that through this input, a damping effect similar to the one caused by the viscous friction has been introduced. The only element that really changed is the C_l matrix of the linearized Lagrangian equation written in matrix form (eq. 7.5):

$$\mathbf{C}_l = \begin{bmatrix} 0 & \beta K \\ 0 & \beta K \end{bmatrix}$$

The transfer function of the blocks contained in the blue square of fig. 7.6 can be written down as:

$$G(s) = \frac{2K\mathbf{C}(s\mathbf{I} - \mathbf{A})^{-1}\mathbf{B}}{1 + 2K\beta\mathbf{E}(s\mathbf{I} - \mathbf{A})^{-1}\mathbf{B}} \tag{7.14}$$

where the vector $\mathbf{E} = [0\ 0\ 0\ 1]$ was defined to select the pendulum angular speed from the state vector. The evolution of the closed loop system poles by varying the value of β and without using the speed controller can be studied analyzing the roots of the equation: $1 + G(s, \beta) = 0$. Figure 7.7 presents a graph illustrating the variation of the three roots as the β value is varied from 0 to 5. It can be observed that the closed-loop system becomes stable for values of β greater than 0.32. This finding indicates that a minimum value of β is required to ensure the stability of the system.

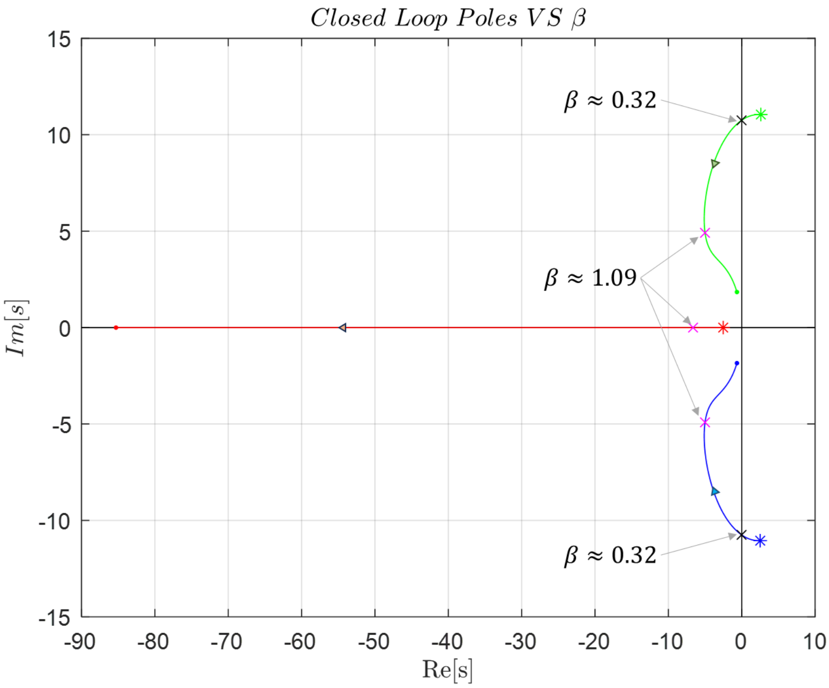

Figure 7.7: Locus of the closed loop system poles of when varying the parameter β from 0 to 5 and without any speed controller.

The Speed Controller

The speed controller block is responsible for computing the control input of the transfer function $G(s)$ (eq. 7.14). The controller was designed to track a step angular velocity reference input with a value that can vary from $0 rad/s$ to $10 rad/s$ (equivalent to a linear speed of 2.5 m/s) within a minimum settling time and with a limited peak in the system response. Moreover, it was designed to work when the sphere is rolling on an inclined plane with an angle of steepness that can vary from $-15°$ to $15°$. The SR is a highly non-linear system, and for this reason a non linear controller was adopted. A scheme of the overall speed controller is shown in fig. 7.8. It can be observed that a PID (Proportional Integral Derivative) and a PI (Proportional Integral) controllers have been used. The first one (PID$_1$) relies on a fuzzy gain scheduler logic to perform an on-line tuning of the PID gains on the basis of the error signal. The second one (PI*) is characterized by constant gains and it works only when the output gets closer to the reference input. Its objective consists of ensuring a faster convergence to the desired value limiting the response overshoot. A set/reset block is responsible for turning on or off the PI* block depending on how close the system response is to the reference input. Finally, a switch is used to turn to zero the output of the speed controller when the angle of the pendulum overcomes the 90°. This simple solution was adopted to limit the range of motion of the pendulum without slowing down the system response.

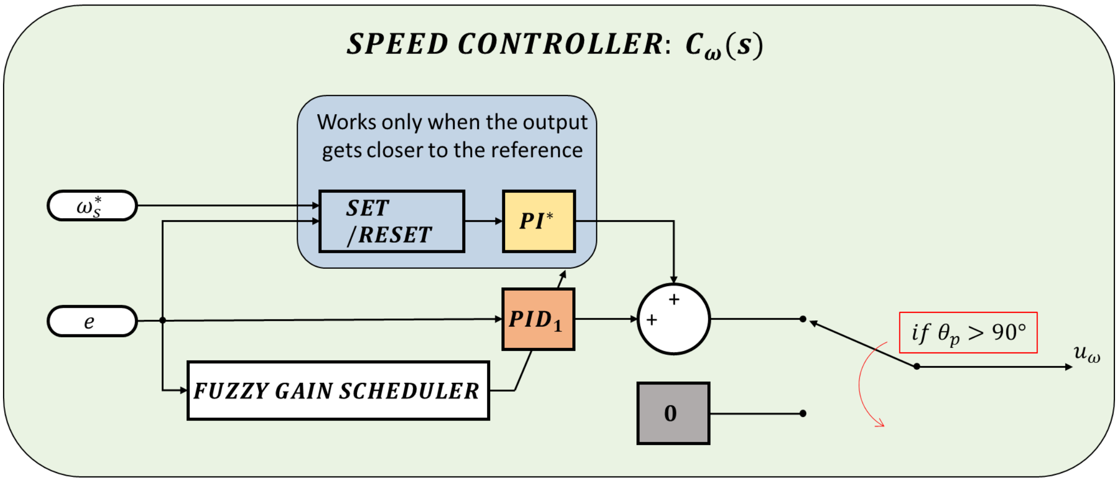

Figure 7.8: Scheme of the speed controller.

The Speed Controller: Fuzzy Gain Scheduler

The fuzzy gain scheduler was realized using the “lookup table” blocks from the Simulink Library. The result is the same as the one that would have been achieved through the “fuzzy” block, but this solution ensures a much faster simulation.

To design the fuzzy controller, the following steps were followed:

1. **Choose the fuzzy controller inputs and outputs**.
   Initially, two inputs were considered for the design: the error between the desired and actual angular velocity, and the inclination angle of the plane. However, it was found to be overly complex to evaluate the second value, resulting in the decision to utilize only the first input. The outputs of the controller are the three PID gains.

2. **Define the linguistic descriptors to be used.**
   The input and output variables are identified through “Linguistic Variables”: “error” was used to refer to the input signal, while “P-gain”, “I-gain”, and “D-gain” to the output ones. Both the input and output subsets can assume

different "Linguistic Values", each one corresponding to a specific value of the related variable. Specifically the input ones are "Ze","S","M","L","XL". The output linguistic values are:

- P-gain: "XS","S","M","L","XL";
- I-gain: "S","M".
- D-gain: "S","M".

3. **Define the membership function for each Linguistic Variable**.
   The membership functions are used to define the degree of membership of a linguistic variable to a certain linguistic value, the "degree of truth" of a statement (e.g. "The error is small" will have a degree of membership equal to 1 when $e(t) = 4\ rad/s$). In fig. 7.9, the graphic membership functions are depicted. The crisp values correspondent to each linguistic value of the PID gains were obtained by a manually tuning PID controllers to enhance the output response to five different step inputs, each one of the value of the crisp errors.

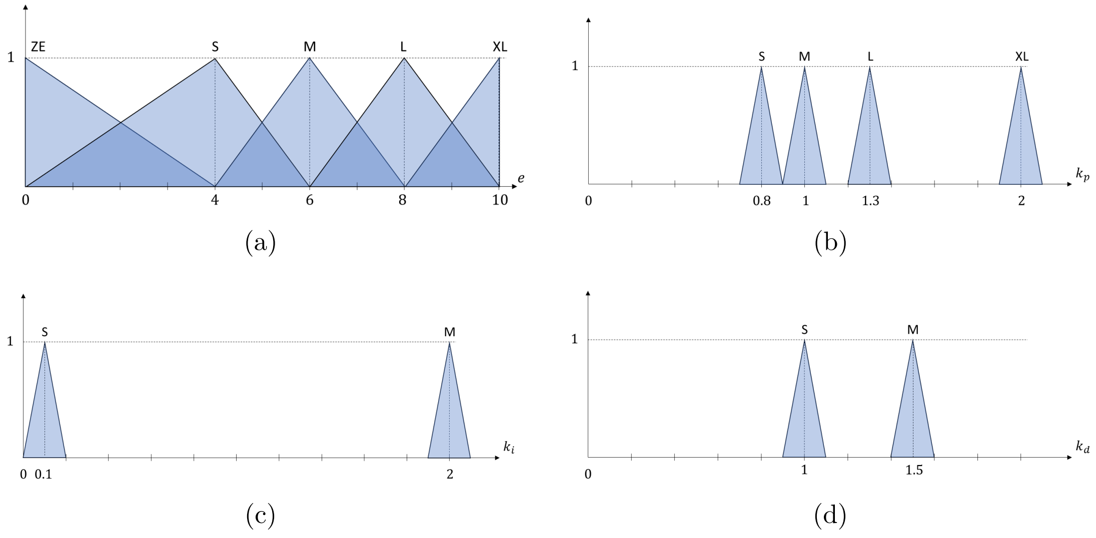

(a) (b)

(c) (d)

Figure 7.9: Membership functions of the error (a), the proportional gain (b), the integral gain (c), and the derivative gain (d).

4. **Define the rules and the defuzzification method**.
   The rules of the fuzzy block are depicted in fig. 7.10. The "centroid defuzzification method" was adopted.

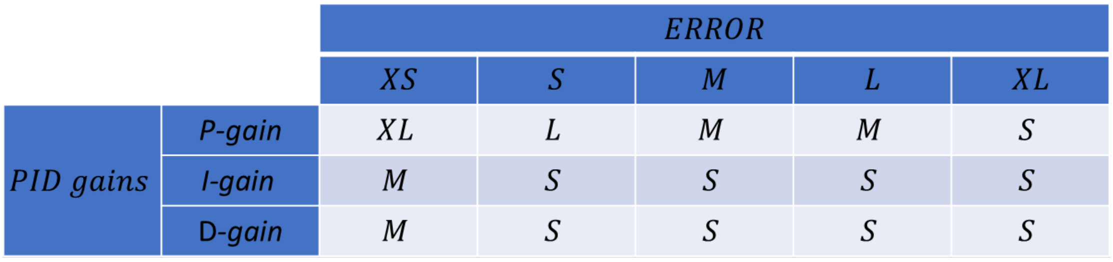

		ERROR				
		XS	S	M	L	XL
PID gains	P-gain	XL	L	M	M	S
	I-gain	M	S	S	S	S
	D-gain	M	S	S	S	S

Figure 7.10: Fuzzy rules table.

The Speed Controller: Set/Reset and PI*

The second controller is a proportional-integral controller. The controller gains have been chosen with the objective of providing a faster convergence of the output to the reference value. Consequently higher gains were selected, namely $k_p = 4$, and $k_i = 10$. As already mentioned, in order to to control the activation of the PI* controller, a set/reset block has been Incorporated before it. This block enables the PI controller to operate only when the error is close to zero. Specifically, if the speed reference is greater than 4 rad/s, the PI* will start working when the error is less than the 8% of the speed reference, while it will be deactivated if it overcomes the 20%.For speed references below 4 rad/s, the percentage error is calculated relative to this velocity. The use of different threshold values (8% and 20%) for activating and deactivating the controller was done to avoid chattering issues.

In fig. 7.11, the truth table of the reset dominant logic used is presented. From

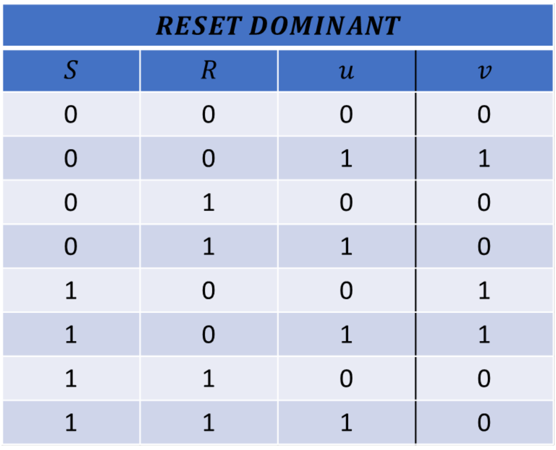

RESET DOMINANT			
S	R	u	v
0	0	0	0
0	0	1	1
0	1	0	0
0	1	1	0
1	0	0	1
1	0	1	1
1	1	0	0
1	1	1	0

Figure 7.11: Truth table of the set/reset, reset dominant logic.

the table, the following logic expression can be deduced:

$$v = \bar{S}\bar{R}u + S\bar{R}\bar{u} + S\bar{R}u = \bar{R}(u\bar{S} + S). \tag{7.15}$$

This expression can be represented graphically through the scheme of fig. 7.12.

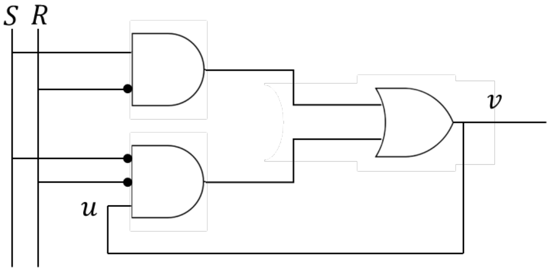

Figure 7.12: Logic circuit of the set/reset, reset dominant logic.

7.4 Straight Path Controller With Gravity Compensation

A second straight path controller was developed after testing the previous one on the multibody model. Specifically, the obtained results did not align with the expectations, showing that the robot couldn't move along a straight path on an inclined plane. Even if the same reference current (which is equivalent to a torque reference) was provided by the controller to the two motors, their speeds were unexpectedly different. This second controller was developed in the attempt to address the cause of this deviation. In fact, the difference from the other controller

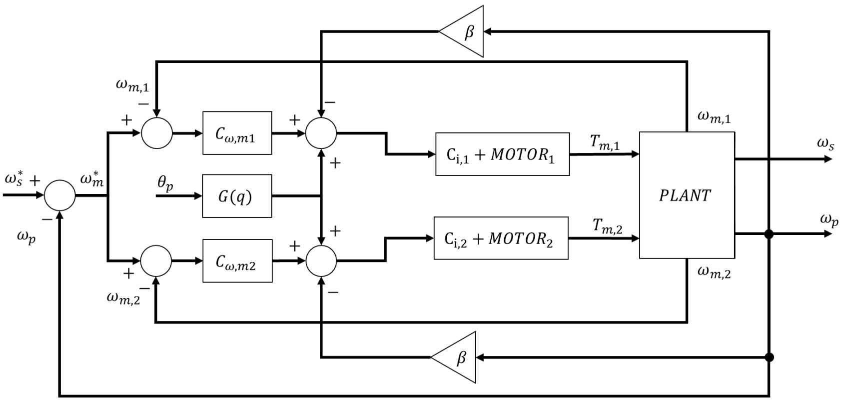

Figure 7.13: Scheme of the straight path controller with gravity compensation.

lies in the external control loop. Two different speed controllers are used, one for each motor, and each one of these compute the control input based on the single motor speed error. These values are calculated by subtracting the actual motor speeds from the motor reference speed, which is computed using eq. 4.1. The same damping contribution of the previous controller, calculated as the β parameter times the pendulum speed, is then subtracted to both the output of the speed controllers. Finally, gravity compensation is performed to compute the contribution needed to compensate the gravity force acting on the sphere. This part of the controller is crucial to guarantee steady state zero error when the robot moves on an inclined plane. The gravity compensation output is added to both the control inputs. The schematic diagram of this controller can be observed in fig. 7.13.

The two speed controllers consist in simple PDs (proportional-derivative controllers), where both the gain were selected equal to 0.02. The β parameter was chosen equal to 14. The output of the gravity compensation is equal to:

$$\tau_0 = m_p g l \ sin(\theta_p) \tag{7.16}$$

where θ_p is the angle of the pendulum with respect to the vertical axis. If the values of m_p and l used are close to the real ones, and no constant forces except for the gravitational one act on the robot, this controller allows a good tracking of the reference speed.

Chapter 8

Results

8.1 Introduction

In this chapter, the validation of the robot resulting from the design process presented thus far is illustrated.

In the first part, the Maximum Step Height (MSH) that a SR with the CMG system is able to climb is verified. The theoretical MSH value of the SR model incorporating all the design specifications defined along the design process is computed and it is then compared with the value specified in the project requirements. A simplified multibody model of this SR was realized in order to perform an experimental validation of this value. The results of this same test procedure are then presented for the SR model with the SolidWorks-designed components (fig. 4.19).

After these two first paragraphs, some considerations about the influence of the static friction coefficient on the step overcoming capability are made.

Subsequently, the chapter presents the simulation results of the robot when using the forward speed controllers designed in the previous chapter. The outcomes of both the analytical and multibody simulations are showcased.

It is important to note that the results of the simulations of the multibody model assembled with the SolidWorks-designed components did not align with the initial expectations. The underlying factors contributing to this deviation will be thoroughly examined and discussed at the end of this chapter.

8.2 Maximum Surmountable Step Analysis

8.2.1 Test Procedure

To assess the obstacle overcoming capability of the SR, first the theoretical value was calculated. Knowing the design specifications of the robot,this can be done in two ways: the first consists of simply using equation 3.13 and then multiplying the result by the sphere radius; the second one consists of computing the value of a^* and, after dividing it by R, the correspondent point on the curve of fig. 1.3 can be found, knowing the MSH/R value. This second option gives the possibility to understand how much the step that can be overcame with the aid of the gyroscopes is taller than the one that can be climbed without using them.

Then, an experimental test was performed, consisting in validating the obstacle overcoming capability inside the multibody simulations. In order to do that, the torque curves were directly inputted to the revolute-joints of the pendulum motors, while speed curves were given to the spinning and tilting revolute-joint motors of the gyroscopes. The simulations were started with the robot standstill in front of the step. First the torque needed to raise the pendulum at 90° was provided. Then, the CMG system was activated and, simultaneously, the torque needed to react to the gyroscope action was provided to the pendulum motors.

8.2.2 SR Model with Theorized Design Specifications

DESIGN SPECIFICATIONS		
R	$250\ mm$	Radius of the sphere
M_{tot}	$22\ kg$	Total mass of the sphere
M_{sf}	$6\ kg$	Sphere mass
m_p	$16\ kg$	Pendulum mass
a	$87.5\ mm$	Robot COM - sphere center distance
l	$120\ mm$	Pendulum COM - sphere center distance
τ_{90}	$18.88\ Nm$	Torque to raise the pendulum at a 90° angle.
ω	$8000\ rpm$	Flywheel spinning velocity
Ω	$15\ rpm\ W$	Flywheel tilting velocity
I_{fl}	$9.76E-3\ kg \cdot m^2$	Flywheel inertia
τ_G	$25.8\ Nm$	Maximum gyroscopic torque

Table 8.1: Theoretical design specifications of the SR.

The obstacle climbing capability of the SR incorporating all the design specifications defined along the design process was initially tested. In table 8.1 the design details of the model are listed. These specifications were defined in order to make the SR able to climb a step with a height of $110mm$. This value was chosen in order to satisfy the MSH design requirement of 100 mm.

From a theoretical point of view, it can be verified that these values are correct using the equation 3.14. In particular, the value of a^*/R results equal to 0.8285. The correspondent h/R value is equal to 0.44, which, when multiplied by the radius, gives a MSH of 110 mm. In fig. 8.1 , the MSH-over-radius curve is plotted and two points have been marked. The blue one corresponds to the MSH over radius of this robot without the aid of the gyroscopes, which only depends on the barycenter position. The red one, instead, represents the MSH that can be overcame when the gyroscopes are functioning with the spinning and tilting velocities from table 8.1. The MSH/R is increased from a value of 0.06325 to 0.8285, which correspond to steps of a height equal to 15.8 mm and 110 mm, respectively.

This result was then experimentally verified. A simplified multibody model of this SR was constructed in Simulink. A capture of the visualization interface of the SR assembled in the Simscape environment is shown in fig. 8.2. In fig. 8.3, four frames of the SR overcoming the step are shown. The first one shows that

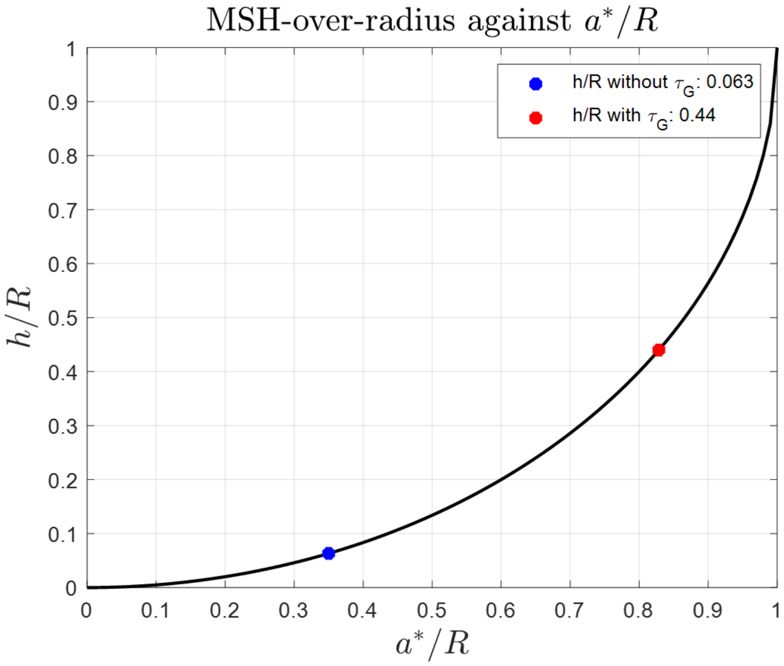

Figure 8.1: MSH-over-radius curve. The red dot identifies the position on the curve when using the gyroscopes, while the blue one when not using them.

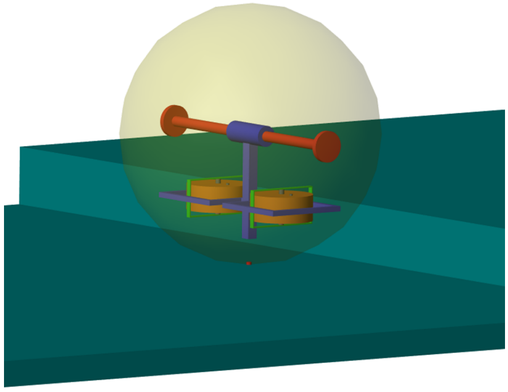

Figure 8.2: Capture of the visualization interface of the simplified SR assembled in the Simscape environment.

the robot is standstill in front of the step with the pendulum raised at 90°. The mere barycenter offset doesn't allow the robot to overcome the obstacle. In the subsequent frames, the spinning gyroscopes start the tilting motion, leading to an increase of the total torque transmitted to the spherical shell and allowing the robot to finally overcome the step.

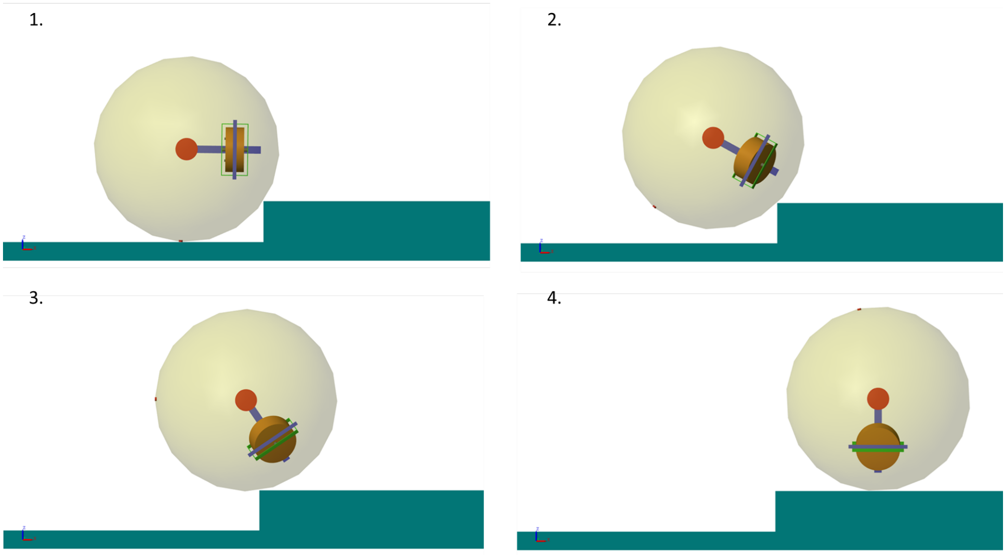

Figure 8.3: Four frames of the SR overcoming a step of 110 mm.

8.2.3 SR Model with SolidWorks-Designed Components

The same test was repeated on the SR model with the SolidWorks-designed components, which was shown in fig. 4.19. Because the hardware and the batteries weren't included in this model, the design specifications differ from the theorized ones and they can be read in table 8.2. Specifically the total mass is equal to only 17.3 kg. Consequently, the theoretical MSH of this robot is higher than 100 mm. It was computed through eq. 3.15, and it resulted equal to 205mm.

The multibody model of this SR was presented in section 5.3.1. A capture of the visualization interface of the SR assembled in the Simscape environment is shown in fig. 8.4. When testing the maximum surmountable obstacle through the simulations, the maximum height of the step was only equal to 162mm. The main reason why the result wasn't the one theorized is because, even if the same torque was given to the two pendulum motors, their output speed was slightly different. As a consequence, due to the utilization of the differential system, the sphere direction wasn't perpendicular to the step, and the torque available for overcoming the step was smaller than the needed one. A more in-depth explanation to this problem is presented in the next paragraphs.

In fig. 8.5, four frames of this SR overcoming the step 162mm tall are shown.

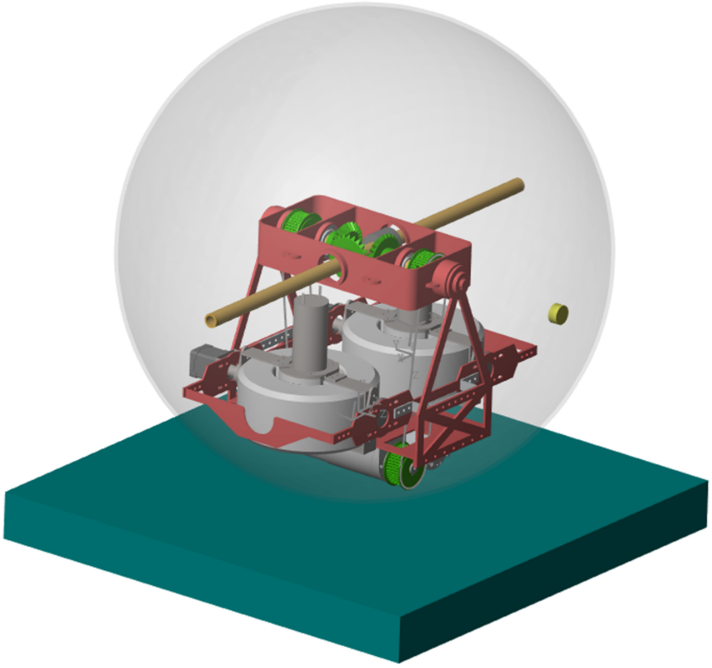

Figure 8.4: Capture of the visualization interface of the SR assembled with the Solidworks components in the Simscape environment.

DESIGN SPECIFICATIONS

R	$250\ mm$	Radius of the sphere
M_{tot}	$17.3\ kg$	Total mass of the sphere
M_{sf}	$4.2\ kg$	Sphere mass
m_p	$13.1\ kg$	Pendulum mass
a	$95.2\ mm$	Robot COM - sphere center distance
l	$126\ mm$	Pendulum COM - sphere center distance
τ_{90}	$16.18\ Nm$	Torque to raise the pendulum at a 90° angle.
ω	$8000\ rpm$	Flywheel spinning velocity
Ω	$15\ rpm\ W$	Flywheel tilting velocity
I_{fl}	$0.00976\ kg \cdot m^2$	Flywheel inertia
τ_G	$25.8\ Nm$	Maximum gyroscopic torque

Table 8.2: Specifications of the multibody model assembled using the CAD files of the SR designed through Solidworks.

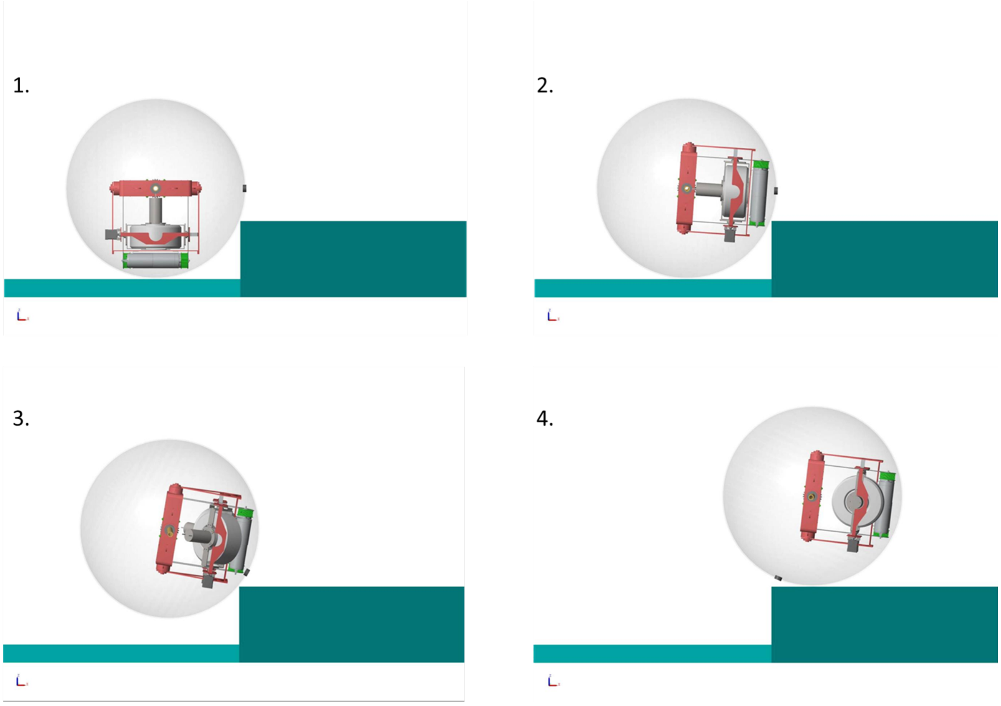

Figure 8.5: Four frames of the SR model with the SolidWorks-designed components overcoming a step of height $162mm$.

8.2.4 Static Friction Considerations

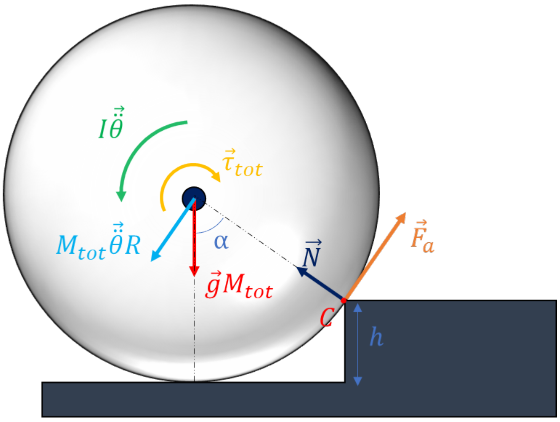

Figure 8.6: Free body diagram of the robot when overcoming a step.

In the tests that were performed, the hypothesis of pure rolling motion were made. However, it must be pointed out that in a real environment, the shell and the step materials determine the static friction coefficient, which can limits the height of the surmountable step. Referring to the figure above, the following equations can be deduced:

$$\begin{cases} M\ddot{\theta}R + Mg\ sin(\alpha) = F_a \\ \\ N = Mg\ cos(\alpha) = Mg\frac{R-h}{R} \\ \\ I\ddot{\theta} + M\ddot{\theta}R^2 + MgR\ sin(\alpha) = \tau \end{cases} \tag{8.1}$$

To have a pure rolling movement, which is necessary to overcome the step, the ratio between the friction and the force referred as N must be lower than the static friction coefficient. Its minimum value can be computed as:

$$\mu_s = \frac{(\frac{\tau - MgR\ sin(\alpha)}{I+MR^2})R + g\ sin(\alpha)}{g(R-h)/(R)} \tag{8.2}$$

To overcome a step 100 mm tall with the designed SR, a static friction coefficient of approximately 1.3 is needed. This value exceeds the average one typically observed among natural surfaces. Consequently, relying solely on the inherent friction between the spherical shell and the ground is impractical. Therefore, in the future, a thorough study must be performed to design a rubber cover with specific surface features that enhance the gripping capabilities of the shell on the ground.

8.3 Control Systems Validation

In the following paragraphs the results of the application of the linear speed controllers on the simulated SR models are presented. First, the results obtained from the analytical simulations when using the linear speed controller with the fuzzy gain scheduler are illustrated. Subsequently, the performance of this controller on the multibody model of the SR with Solidworks-designed components (fig. 8.4) is showcased. As anticipated in the previous chapter, these outcomes deviated from the results obtained through analytical simulations. To address this problem, a second control architecture with specific speed controllers dedicated to each motor was designed. Therefore, the results obtained by testing this second control system are shown. The problems that affected the previous results can be observed to also affect these ones. Finally, a discussion about the underlying factors contributing to this deviations is presented.

8.3.1 Test Procedures

To test the control architecture and verify their functioning, two linear speed profiles have been provided as input of the controllers and the system response have been evaluated comparing it with the desired one. These tests have been repeated for three different angles of inclination of the plane where the SR was moving: 0°, 7°, and 15°.

8.3.2 Analytical model

In the simulations of the analytical SR model, only the linear speed controller with the fuzzy gain scheduler was validated. This is due to the fact that only one motor with a doubled output torque was modeled in the analytical system. The second control architecture consisted of two specific speed controllers dedicated to each motor. Therefore, it couldn't be applied on this simulation.

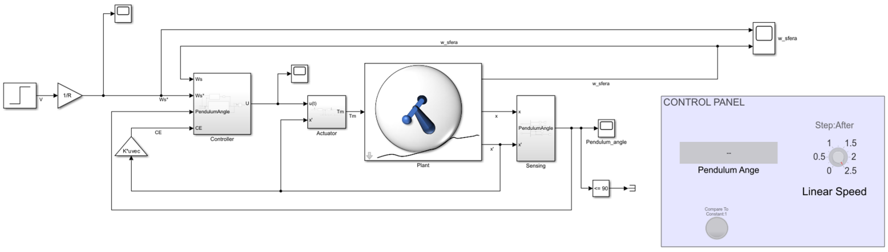

Figure 8.7: Screen capture of the analytical model of the robot with the linear speed controller simulated in Simulink.

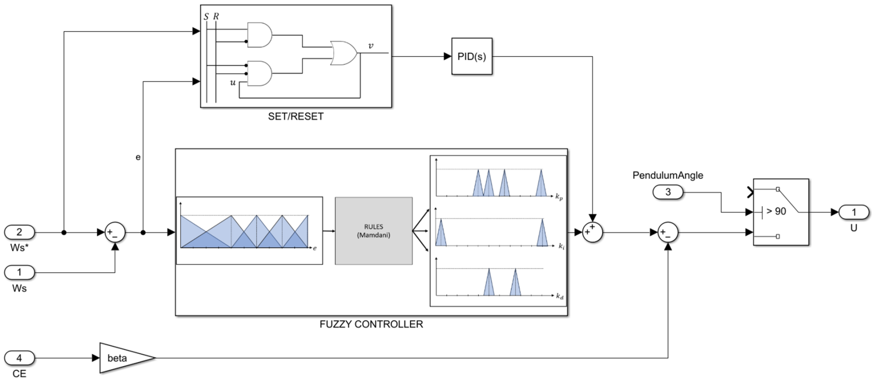

Figure 8.8: Screen capture of the structure of the controller block.

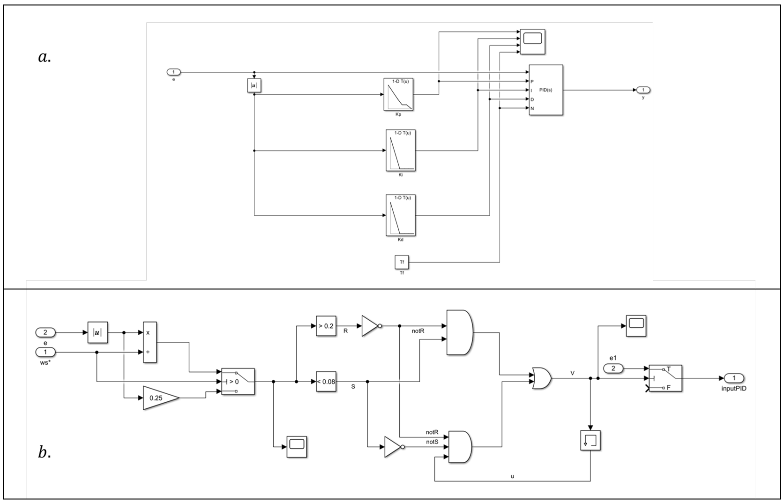

Figure 8.9: Structure of the fuzzy gain scheduler (a) and the set/reset block (b).

The screen capture of the analytical model of the robot with the linear speed controller is shown in fig. 8.7. In fig. 8.8 the structure of the controller block is illustrated, while the structure of the fuzzy gain scheduler and the set/reset blocks are shown in fig.8.9(a) and (b), respectively. The functioning of the system was evaluated giving two types of input: a signal composed by subsequent velocity steps of 1 m/s, 1.5 m/s, 2 m/s, and 2.5 m/s, and a trapezoidal velocity profile that reaches 2.5 m/s. The robot was tested on a plane with an inclination of 0°, 7°, and 15°. The results are shown in figures 8.10-8.12. It can be observed that the controller allows the tracking of the velocity profile in all three scenarios, enabling a good control of the system also on steeper terrains. At 7° and 15° the curves starts with a decreasing trend because the robot is in a standstill position on an inclined plane.

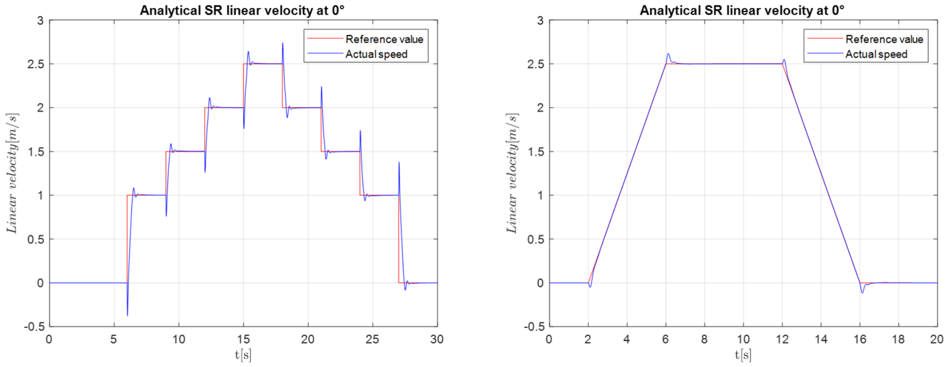

Figure 8.10: Linear speed of the analytical robot model VS input speed profile. Testing on a plane with an inclination of 0°.

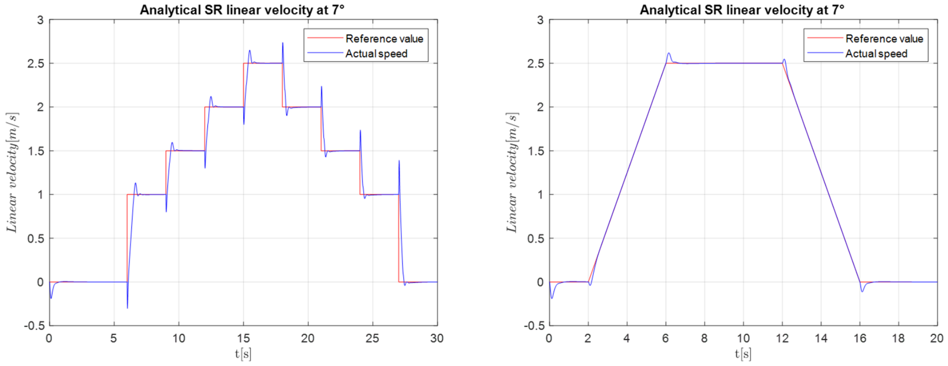

Figure 8.11: Linear speed of the analytical robot model VS input speed profile. Testing on a plane with an inclination of 7°.

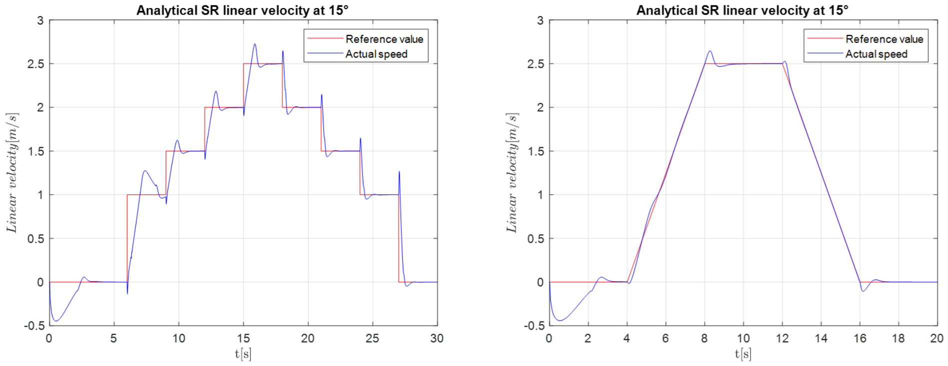

Figure 8.12: Linear speed of the analytical robot model VS input speed profile. Testing on a plane with an inclination of 15°.

8.3.3 Multibody Model

Linear Speed Controller with Fuzzy Gain Scheduler

In this paragraph, the results of the application of the fuzzy gain scheduler linear speed controller on the multibody model of the SR of fig. 8.4 are presented. A screen capture of the Simulink environment with the robot model and the controller is shown in fig. 8.13 . The results from testing the control architecture when the robot moves on a horizontal plane are shown in figure 8.14. The same input speed profiles that were given to the analytical model of the SR were used. It can be noted that the response doesn't overlap with the one of the analytical model, but both the velocity profiles are well tracked by the SR. Under the sphere center speed graphs, the path followed by the robot in the XY plane during the manoeuvres can be observes. It can be noted that, in the first scenario, there is a deviation of 16 *cm* in the negative direction of the y-axis. However, this deviation accounts for less than 0.5% of the length of the displacement along the x-axis. In fig. 8.15, the sphere center speed of the SR along the x-axis when moving on a slope of 5° is shown. It can be observed that the robot is not able to follow the desired trajectory. The cause of this result is the same one that was described in the paragraph 8.2.3. Specifically, even if the same torque was given to the two pendulum motors, their output speed differs, causing the sphere to move in a different way from the predicted one.

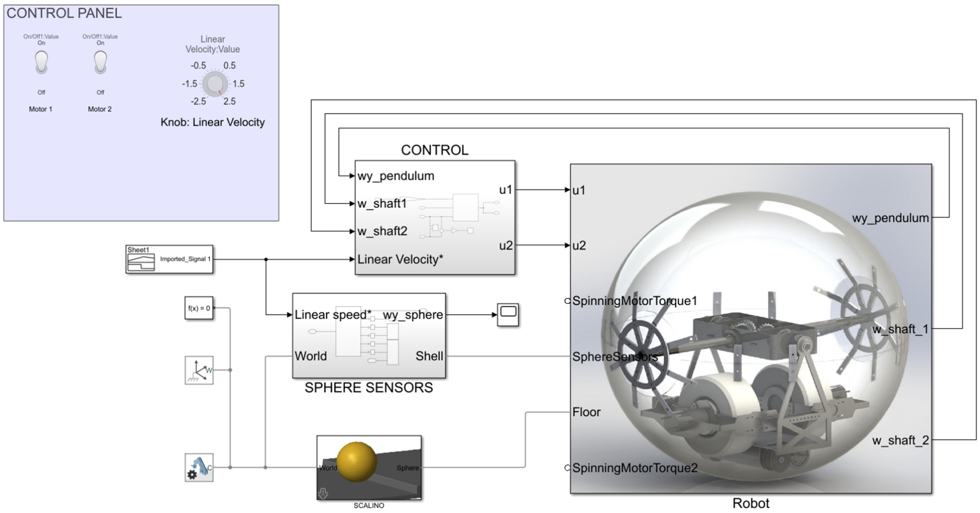

Figure 8.13: Simulink environment with the robot model and the linear speed controller.

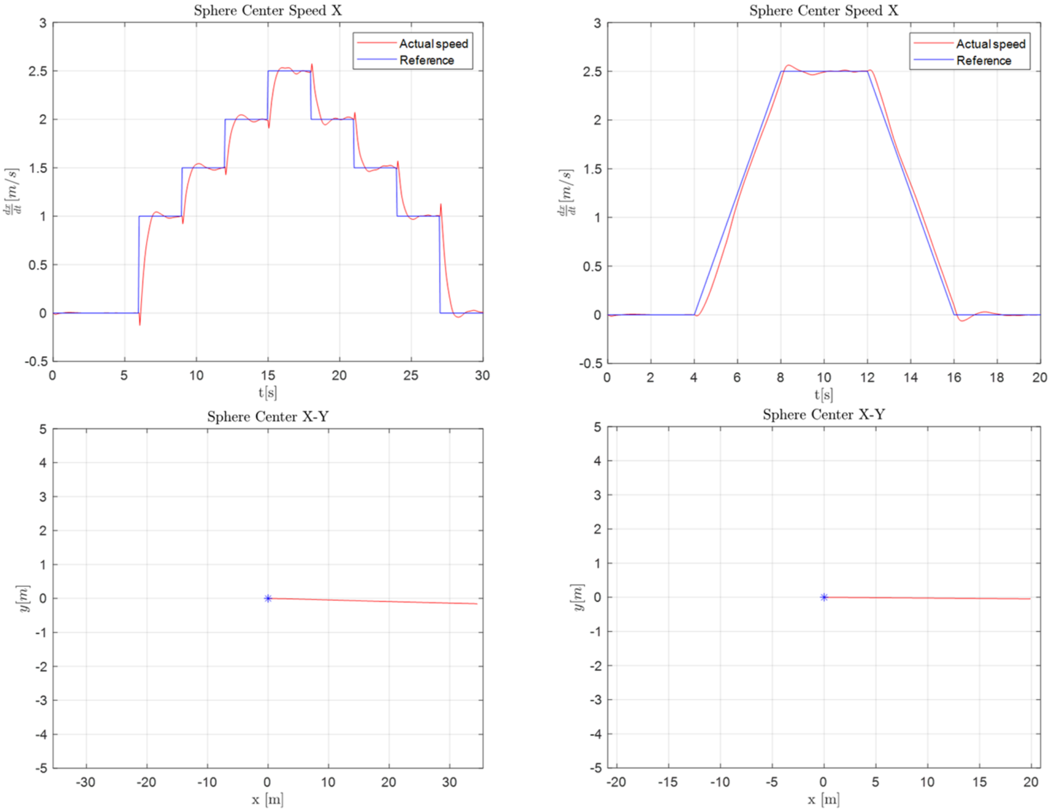

Figure 8.14: Linear speed of the multibody robot model VS input speed profile. Testing the fuzzy gain scheduler controller on a plane with an inclination of 0°.

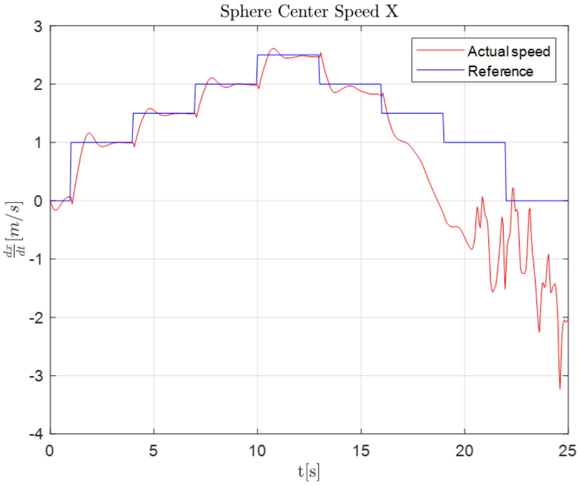

Figure 8.15: Linear speed of the multibody robot model VS input speed profile. Testing the fuzzy gain scheduler controller on a plane with an inclination of 7°.

Linear Speed Controller with Gravity Compensation

As already explained, to address the problem that was experienced when testing the fuzzy gain scheduler controller, a second control architecture with two separated speed controllers was developed. The same tests were performed. Here, only the result obtained when the sphere is moving on a plane with an inclination of 7° is presented and it can be observed in fig. 8.16. It can be noted that also this controller doesn't perform as planned. Specifically, also in this case, the speeds of the two motors differ. A graph showing the angular velocity curves of the motors can be observed in fig. 8.17. In the next paragraph, the possible cause behind this unexpected outcomes is discussed.

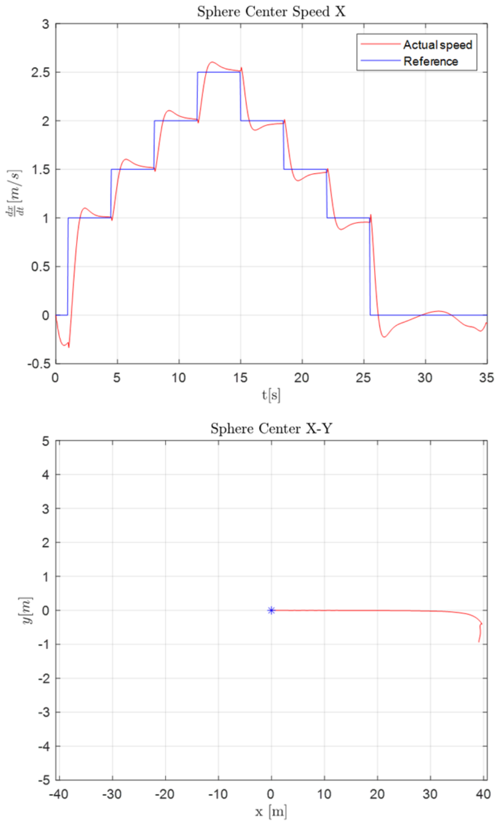

Figure 8.16: Linear speed of the multibody robot model VS input speed profile. Testing the controller with gravity compensation on a plane with an inclination of 7°.

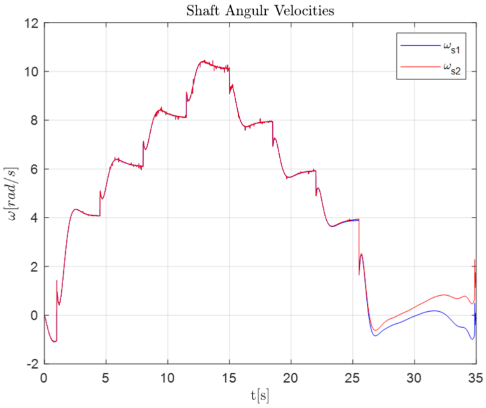

Figure 8.17: Shaft Angular Velocities of the two pendulum motors when controlled through the controller with gravity compensation on a plane with an inclination of 7°.

8.4 Analysis of Underlying Factors for Deviations in Simulation Results

The unexpected behavior of the robot when the control systems were tested can be attributed to the different output speeds of the two pendulum motors. This is believed to be caused by the action of varying resistive torques on the bevel gears of the differential system. These resistive torques, in turn, result from the tilting of the central shaft of the sphere as a consequence to friction forces acting along a direction not parallel to the rolling one.

This behavior was not anticipated, and it was initially assumed that the design of the straight-line motion control systems could be achieved based on the two-dimensional analytical equations of the robot. In particular, although the use of a differential system does not allow for decoupling the control of the two motors, it was believed that a system characterized by a single motor with a doubled output torque could effectively describe the problem at hand. This is because if the same resistive torques act on the two motors, they will have equal and opposite output speeds. It has been shown through the kinematic equations of the differential system that this results in a straight line movement of the robot.

However, if there are forces acting along a different direction from the rolling one, the linear speed controllers weren't designed to effectively correct the control input, causing the system response to be different from the desired one.

Chapter 9

Conclusions

This master's thesis focuses on the design and development of a pendulum-driven spherical robot (SR), drawing inspiration from prior research conducted by [1]. The framework outlined in [1] successfully addressed some of the technical challenges associated with creating such a complex robot. However, limitations in its design were identified, motivating extensive efforts to enhance the robot's efficiency and versatility. The primary objective of this research was to develop a viable solution that could improve the robot's obstacle-climbing capability.

To achieve this goal, a performance parameter called MSH (Maximum Step Height) was defined. Its value is computed as the height of a step at which the SR, when generating the maximum torque, is able to maintain an equilibrium condition on the step edge. The MSH value of the SR designed by [1] was equal to 25 *mm*. The objective of this thesis was to improve it up to a value of 100 *mm*.

For a simple pendulum-driven spherical robot it was shown that the only solution to improve the MSH value consisted in increasing the distance between the barycenter and the center of the sphere. Nevertheless, this complicates a lot the design process.

The solution proposed in this thesis entails the integration of a Control Moment Gyroscope (CMG) auxiliary propulsion system. This system enables to momentarily increase the maximum torque transmittable to the spherical shell. Consequently, the MSH can be substantially improved without necessitating a considerable displacement of the robot's barycenter from the sphere center.

The first part of this work was dedicated to study the working principle of the CMG systems. An innovative spherical robot driving mechanism composed only by gyroscopes was proposed. After a detailed analysis, it was concluded that this system couldn't be used to meet the project requirements. Hence, the use of the two CMGs as an auxiliary propulsion system was presented, coupling it with the pendulum system with the differential mechanism developed by [1]. It was explained the strategy behind this solution, and it was illustrated how the relation between the MSH and the robot barycenter position was changed by the introduction of the gyroscopic torque.

After this preliminary study, the design process of the gyroscopes was presented, showing the solutions adopted in order to meet the project requirements. A brief analysis of the drag forces acting on a high-speed spinning flywheel was realized in order to correctly select the motors responsible for the spinning motion. After finalizing the design of the CMG group, the two main motors controlling the pendulum were dimensioned, selecting them based on the nominal robot speed requirement of 2.5 m/s. Once all the motors were selected, the battery pack was dimensioned to meet the runtime requirement of a minimum of 1 h while working at the nominal operating point (climbing a slope of 15° at a speed of 2.5 m/s). For the spherical shell, the harmonic steel sheets used in [1] were substituted with two PMMA hollow hemispheres. A second layer made of impermeable rubber is needed to enhance the static friction of the shell on the ground.

The final result of the design process was a spherical UGV with a diameter of 0.5 m, and a total mass of 18 kg. The batteries and the hardware weren't included, but the whole dimensioning process was performed considering a total mass of 22 kg, allowing for the inclusion of hardware components weighing up to 4 kg while still adhering to the project requirements.

Simulated models of the SR were then created to study its performance. An analytical model able to describe the straight motion on an inclined plane was developed, and linear speed controllers were designed based on this model. More comprehensive multibody models of the SR were utilized to verify the project requirements and test the designed controllers.

The results demonstrated that the CMG system successfully enhanced the robot's obstacle overcoming capability. Through a simplified multibody model incorporating all the specifications obtained from the design process it was shown that this solution allowed to successfully climb steps with the expected height. However, when testing the robot's obstacle overcoming capability and the linear speed controllers on the multibody models with the differential mechanism developed by [1], discrepancies between the expected and obtained results were observed. These findings highlighted the challenges associated with controlling a spherical robot through a differential mechanism.

Overall, this master's thesis made significant progress in the design and development of a pendulum-driven spherical robot, presenting a viable solution to improve its obstacle-climbing capability. The integration of a Control Moment Gyroscope auxiliary propulsion system showed promise in enhancing the robot's performance. Further research should focus on selecting the appropriate hardware components, designing a rubber cover with surface features to enhance gripping capabilities, and developing a control system capable of controlling the robot on both straight and curvilinear paths. These future efforts will contribute to advancing the field of spherical robotics and maximizing the robot's capabilities in various applications.

Appendix A

Gantt

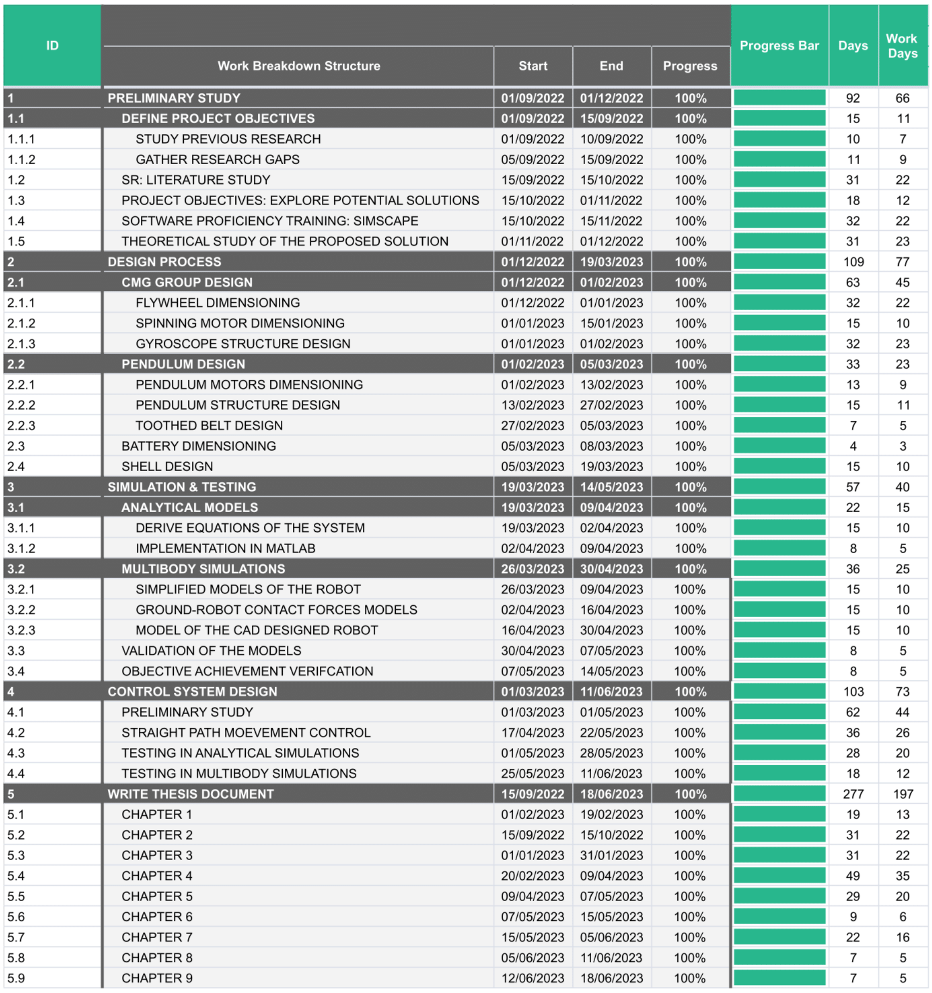

ID	Work Breakdown Structure	Start	End	Progress	Progress Bar	Days	Work Days
1	**PRELIMINARY STUDY**	**01/09/2022**	**01/12/2022**	**100%**	🟩	92	66
1.1	**DEFINE PROJECT OBJECTIVES**	**01/09/2022**	**15/09/2022**	**100%**	🟩	15	11
1.1.1	STUDY PREVIOUS RESEARCH	01/09/2022	10/09/2022	100%	🟩	10	7
1.1.2	GATHER RESEARCH GAPS	05/09/2022	15/09/2022	100%	🟩	11	9
1.2	SR: LITERATURE STUDY	15/09/2022	15/10/2022	100%	🟩	31	22
1.3	PROJECT OBJECTIVES: EXPLORE POTENTIAL SOLUTIONS	15/10/2022	01/11/2022	100%	🟩	18	12
1.4	SOFTWARE PROFICIENCY TRAINING: SIMSCAPE	15/10/2022	15/11/2022	100%	🟩	32	22
1.5	THEORETICAL STUDY OF THE PROPOSED SOLUTION	01/11/2022	01/12/2022	100%	🟩	31	23
2	**DESIGN PROCESS**	**01/12/2022**	**19/03/2023**	**100%**	🟩	109	77
2.1	**CMG GROUP DESIGN**	**01/12/2022**	**01/02/2023**	**100%**	🟩	63	45
2.1.1	FLYWHEEL DIMENSIONING	01/12/2022	01/01/2023	100%	🟩	32	22
2.1.2	SPINNING MOTOR DIMENSIONING	01/01/2023	15/01/2023	100%	🟩	15	10
2.1.3	GYROSCOPE STRUCTURE DESIGN	01/01/2023	01/02/2023	100%	🟩	32	23
2.2	**PENDULUM DESIGN**	**01/02/2023**	**05/03/2023**	**100%**	🟩	33	23
2.2.1	PENDULUM MOTORS DIMENSIONING	01/02/2023	13/02/2023	100%	🟩	13	9
2.2.2	PENDULUM STRUCTURE DESIGN	13/02/2023	27/02/2023	100%	🟩	15	11
2.2.3	TOOTHED BELT DESIGN	27/02/2023	05/03/2023	100%	🟩	7	5
2.3	BATTERY DIMENSIONING	05/03/2023	08/03/2023	100%	🟩	4	3
2.4	SHELL DESIGN	05/03/2023	19/03/2023	100%	🟩	15	10
3	**SIMULATION & TESTING**	**19/03/2023**	**14/05/2023**	**100%**	🟩	57	40
3.1	**ANALYTICAL MODELS**	**19/03/2023**	**09/04/2023**	**100%**	🟩	22	15
3.1.1	DERIVE EQUATIONS OF THE SYSTEM	19/03/2023	02/04/2023	100%	🟩	15	10
3.1.2	IMPLEMENTATION IN MATLAB	02/04/2023	09/04/2023	100%	🟩	8	5
3.2	**MULTIBODY SIMULATIONS**	**26/03/2023**	**30/04/2023**	**100%**	🟩	36	25
3.2.1	SIMPLIFIED MODELS OF THE ROBOT	26/03/2023	09/04/2023	100%	🟩	15	10
3.2.2	GROUND-ROBOT CONTACT FORCES MODELS	02/04/2023	16/04/2023	100%	🟩	15	10
3.2.3	MODEL OF THE CAD DESIGNED ROBOT	16/04/2023	30/04/2023	100%	🟩	15	10
3.3	VALIDATION OF THE MODELS	30/04/2023	07/05/2023	100%	🟩	8	5
3.4	OBJECTIVE ACHIEVEMENT VERIFCATION	07/05/2023	14/05/2023	100%	🟩	8	5
4	**CONTROL SYSTEM DESIGN**	**01/03/2023**	**11/06/2023**	**100%**	🟩	103	73
4.1	PRELIMINARY STUDY	01/03/2023	01/05/2023	100%	🟩	62	44
4.2	STRAIGHT PATH MOEVEMENT CONTROL	17/04/2023	22/05/2023	100%	🟩	36	26
4.3	TESTING IN ANALYTICAL SIMULATIONS	01/05/2023	28/05/2023	100%	🟩	28	20
4.4	TESTING IN MULTIBODY SIMULATIONS	25/05/2023	11/06/2023	100%	🟩	18	12
5	**WRITE THESIS DOCUMENT**	**15/09/2022**	**18/06/2023**	**100%**	🟩	277	197
5.1	CHAPTER 1	01/02/2023	19/02/2023	100%	🟩	19	13
5.2	CHAPTER 2	15/09/2022	15/10/2022	100%	🟩	31	22
5.3	CHAPTER 3	01/01/2023	31/01/2023	100%	🟩	31	22
5.4	CHAPTER 4	20/02/2023	09/04/2023	100%	🟩	49	35
5.5	CHAPTER 5	09/04/2023	07/05/2023	100%	🟩	29	20
5.6	CHAPTER 6	07/05/2023	15/05/2023	100%	🟩	9	6
5.7	CHAPTER 7	15/05/2023	05/06/2023	100%	🟩	22	16
5.8	CHAPTER 8	05/06/2023	11/06/2023	100%	🟩	7	5
5.9	CHAPTER 9	12/06/2023	18/06/2023	100%	🟩	7	5

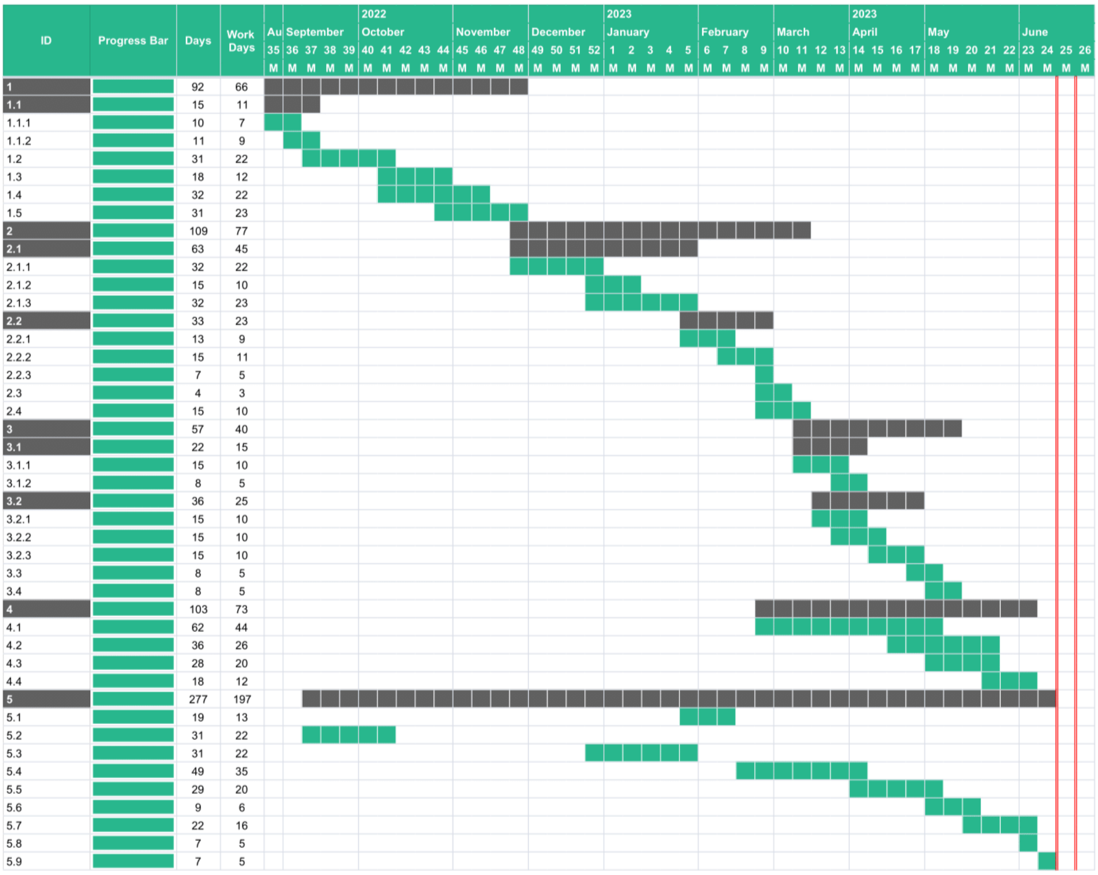

ID	Progress Bar	Days	Work Days
1	🟩	92	66
1.1	🟩	15	11
1.1.1	🟩	10	7
1.1.2	🟩	11	9
1.2	🟩	31	22
1.3	🟩	18	12
1.4	🟩	32	22
1.5	🟩	31	23
2	🟩	109	77
2.1	🟩	63	45
2.1.1	🟩	32	22
2.1.2	🟩	15	10
2.1.3	🟩	32	23
2.2	🟩	33	23
2.2.1	🟩	13	9
2.2.2	🟩	15	11
2.2.3	🟩	7	5
2.3	🟩	4	3
2.4	🟩	15	10
3	🟩	57	40
3.1	🟩	22	15
3.1.1	🟩	15	10
3.1.2	🟩	8	5
3.2	🟩	36	25
3.2.1	🟩	15	10
3.2.2	🟩	15	10
3.2.3	🟩	15	10
3.3	🟩	8	5
3.4	🟩	8	5
4	🟩	103	73
4.1	🟩	62	44
4.2	🟩	36	26
4.3	🟩	28	20
4.4	🟩	18	12
5	🟩	277	197
5.1	🟩	19	13
5.2	🟩	31	22
5.3	🟩	31	22
5.4	🟩	49	35
5.5	🟩	29	20
5.6	🟩	9	6
5.7	🟩	22	16
5.8	🟩	7	5
5.9	🟩	7	5

Appendix B

Project Ethical Implications

The use of spherical robots in applications such as search and rescue operations, surveillance, and exploration of unstructured or unknown environments presents both ethical opportunities and challenges. One of the key benefits is the enhanced safety they offer by reducing the risks and potential injuries to human workers in hazardous situations. These robots can access and navigate areas that are inaccessible or too dangerous for humans, allowing for more effective and efficient operations.

However, the widespread adoption of spherical robots also raises concerns about potential job displacement, particularly for workers in roles such as watchmen or security personnel. While these robots can perform certain tasks autonomously, there is an opportunity to mitigate the impact by retraining and re-educating workers to take on new roles as robot supervisors or operators. By providing the necessary training and skills, these workers can oversee and manage the robots' activities, ensuring their safe and responsible use while leveraging their human judgment and expertise.

Furthermore, the development and large-scale production of spherical robots have the potential to create new job opportunities in various sectors, ranging from manufacturing and maintenance to programming and technical support. This growth in the field can lead to the emergence of specialized roles and skillsets, fostering economic growth and increasing employment prospects.

To address the ethical implications, it is essential to prioritize a comprehensive approach that combines technological advancement with social responsibility. This includes investing in education and training programs to equip individuals with the necessary skills to adapt to the changing job landscape and actively participate in the deployment and management of spherical robots. Additionally, ongoing dialogue between stakeholders, including workers, policymakers, and industry leaders, can facilitate the development of inclusive and ethical practices that ensure a fair transition and balance between human workers and robotic systems.

Appendix C

Budget Analysis

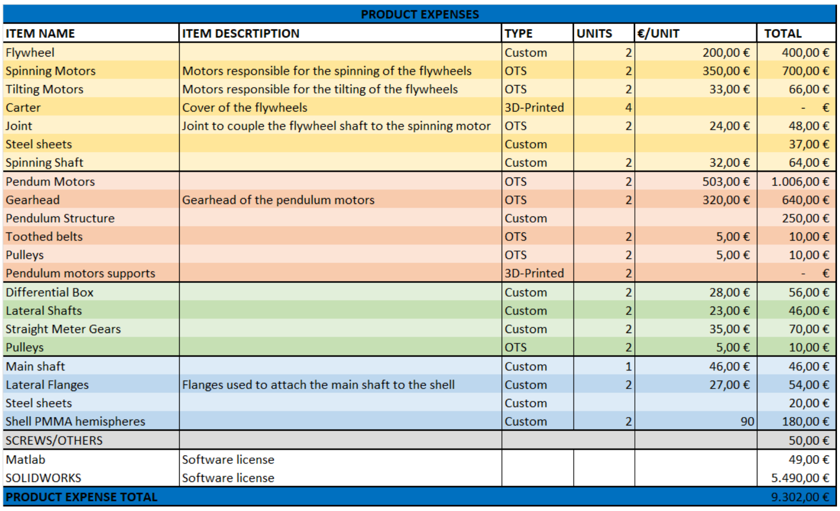

PRODUCT EXPENSES					
ITEM NAME	**ITEM DESCRTIPTION**	**TYPE**	**UNITS**	**€/UNIT**	**TOTAL**
Flywheel		Custom	2	200,00 €	400,00 €
Spinning Motors	Motors responsible for the spinning of the flywheels	OTS	2	350,00 €	700,00 €
Tilting Motors	Motors responsible for the tilting of the flywheels	OTS	2	33,00 €	66,00 €
Carter	Cover of the flywheels	3D-Printed	4		- €
Joint	Joint to couple the flywheel shaft to the spinning motor	OTS	2	24,00 €	48,00 €
Steel sheets		Custom			37,00 €
Spinning Shaft		Custom	2	32,00 €	64,00 €
Pendum Motors		OTS	2	503,00 €	1.006,00 €
Gearhead	Gearhead of the pendulum motors	OTS	2	320,00 €	640,00 €
Pendulum Structure		Custom			250,00 €
Toothed belts		OTS	2	5,00 €	10,00 €
Pulleys		OTS	2	5,00 €	10,00 €
Pendulum motors supports		3D-Printed	2		- €
Differential Box		Custom	2	28,00 €	56,00 €
Lateral Shafts		Custom	2	23,00 €	46,00 €
Straight Meter Gears		Custom	2	35,00 €	70,00 €
Pulleys		OTS	2	5,00 €	10,00 €
Main shaft		Custom	1	46,00 €	46,00 €
Lateral Flanges	Flanges used to attach the main shaft to the shell	Custom	2	27,00 €	54,00 €
Steel sheets		Custom			20,00 €
Shell PMMA hemispheres		Custom	2	90	180,00 €
SCREWS/OTHERS					50,00 €
Matlab	Software license				49,00 €
SOLIDWORKS	Software license				5.490,00 €
PRODUCT EXPENSE TOTAL					9.302,00 €

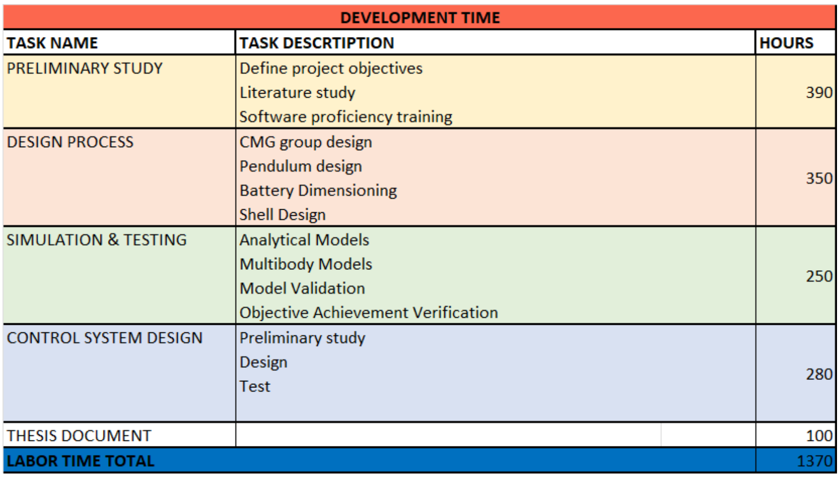

DEVELOPMENT TIME		
TASK NAME	**TASK DESCRTIPTION**	**HOURS**
PRELIMINARY STUDY	Define project objectives Literature study Software proficiency training	390
DESIGN PROCESS	CMG group design Pendulum design Battery Dimensioning Shell Design	350
SIMULATION & TESTING	Analytical Models Multibody Models Model Validation Objective Achievement Verification	250
CONTROL SYSTEM DESIGN	Preliminary study Design Test	280
THESIS DOCUMENT		100
LABOR TIME TOTAL		1370

Bibliography

[1] Matteo Melchiorre, Laura Salamina, Stefano Mauro, and Stefano Pastorelli. «Design of a Spherical UGV for Space Exploration». In: Sept. 2022 (cit. on pp. i–v, 1–4, 49–52, 65, 66, 70, 75, 81, 82, 124, 125).

[2] Jiazhen Chen, Ping Ye, Hanxu Sun, and Qingxuan Jia. «Design and motion control of a spherical robot with control moment gyroscope». In: *2016 3rd International Conference on Systems and Informatics, ICSAI 2016*. Institute of Electrical and Electronics Engineers Inc., Jan. 2017, pp. 114–120. ISBN: 9781509055210. DOI: `10.1109/ICSAI.2016.7810940` (cit. on pp. 5, 21).

[3] Vadym Bilous, Mayur Andulkar, and Ulrich Berger. «Design of a novel spherical robot with high dynamic range and maneuverability for flexible applications». In: *50th International Symposium on Robotics, ISR 2018* (2018), pp. 65–69 (cit. on p. 5).

[4] Gregory C Schroll. «THESIS DYNAMIC MODEL OF A SPHERICAL ROBOT FROM FIRST PRINCIPLES Submitted by». PhD thesis. 2010 (cit. on pp. 5, 12, 20, 22).

[5] Marek Bujňák, Rastislav Pirník, Karol Rástočný, Aleš Janota, Dušan Nemec, Pavol Kuchár, Tomáš Tichý, and Zbigniew Łukasik. *Spherical Robots for Special Purposes: A Review on Current Possibilities*. Feb. 2022. DOI: `10.3390/s22041413` (cit. on pp. 9, 11).

[6] Rotundus AB. *Rotundus*. 2008. URL: `https://rotundus.se` (cit. on pp. 9, 10).

[7] Mattias Seeman, Mathias Broxvall, Alessandro Saffiotti, and Peter Wide. «An autonomous spherical robot for security tasks». In: *Proceedings of the 2006 IEEE International Conference on Computational Intelligence for Homeland Security and Personal Safety, CIHSPS 2006*. Vol. 2006. 2006, pp. 51–55. ISBN: 1424407451. DOI: `10.1109/CIHSPS.2006.313312` (cit. on p. 9).

[8] Shaorong Xie, Jiqing Chen, Jun Luo, Hengyu Li, Junfeng Yao, and Jason Gu. «Dynamic analysis and control system of spherical robot for polar region scientific research». In: *2013 IEEE International Conference on Robotics and Biomimetics, ROBIO 2013*. IEEE Computer Society, 2013, pp. 2540–2545. DOI: `10.1109/ROBIO.2013.6739854` (cit. on pp. 9, 10, 26).

[9] Ye Ping, Sun Hanxu, Qiu Zhongjiang, and Chen Jiazhen. «Design and motion control of a spherical robot with stereovision». In: *Proceedings of the 2016 IEEE 11th Conference on Industrial Electronics and Applications, ICIEA 2016*. Institute of Electrical and Electronics Engineers Inc., Oct. 2016, pp. 1276–1282. ISBN: 9781509026050. DOI: `10.1109/ICIEA.2016.7603781` (cit. on p. 9).

[10] Maotao Yang, Tianping Tao, Jianwen Huo, Konstantin A. Neusypin, Zikun Zhang, Hua Zhang, and Mingming Guo. «Design and Analysis of a Spherical Robot with Two Degrees of Freedom Swing». In: 2020, pp. 4913–4918. ISBN: 9781728158556 (cit. on p. 10).

[11] Angelo Pio Rossi et al. «DAEDALUS - Descent And Exploration in Deep Autonomy of Lava Underground Structures : Open Space Innovation Platform (OSIP) Lunar Caves-System Study». In: 2021 (cit. on pp. 10, 22).

[12] Futao Wang, Chaobing Li, Shaohua Niu, Pengfei Wang, Huaisong Wu, and Bingyang Li. «Design and Analysis of a Spherical Robot with Rolling and Jumping Modes for Deep Space Exploration». In: *Machines* 10.2 (Feb. 2022). ISSN: 20751702. DOI: `10.3390/machines10020126` (cit. on p. 10).

[13] Bo Zhao, Mantian Li, Haitao Yu, Haiyan Hu, and Lining Sun. «Dynamics and motion control of a two pendulums driven spherical robot». In: *IEEE/RSJ 2010 International Conference on Intelligent Robots and Systems, IROS 2010 - Conference Proceedings*. 2010, pp. 147–153. ISBN: 9781424466757. DOI: `10.1109/IROS.2010.5651154` (cit. on pp. 10, 11).

[14] Joong Cheol Yoon, Sung Su Ahn, and Yun Jung Lee. «Spherical robot with new type of two-pendulum driving mechanism». In: *INES 2011 - 15th International Conference on Intelligent Engineering Systems, Proceedings*. 2011, pp. 275–279. ISBN: 9781424489565. DOI: `10.1109/INES.2011.5954758` (cit. on p. 11).

[15] Pham Dinh Ba, Quoc Dong Hoang, Soon Geul Lee, Thanh Hai Nguyen, Xuan Quang Duong, and Boi Chau Tham. «Kinematic modeling of spherical rolling robots with a three-omnidirectional-wheel drive mechanism». In: *International Conference on Control, Automation and Systems*. Vol. 2020-October. IEEE Computer Society, Oct. 2020, pp. 463–466. ISBN: 9788993215205. DOI: `10.23919/ICCAS50221.2020.9268200` (cit. on pp. 12, 13).

[16] Yury L. Karavaev and Alexander A. Kilin. «The dynamics and control of a spherical robot with an internal omniwheel platform». In: *Regular and Chaotic Dynamics* 20.2 (Mar. 2015), pp. 134–152. ISSN: 14684845. DOI: `10.1134/S1560354715020033` (cit. on pp. 12, 13).

[17] Wei Liu, Junyang Sun, Runjiao Wang, Guanwang Geng, and Xiaolong Han. *Heavy-duty Spherical Mobile Robot Driven by Five Omni Wheels.* Tech. rep., pp. 13–17. URL: `www.bjtu.edu.cn` (cit. on pp. 12, 13).

[18] Qiang Zhan, Yao Cai, and Caixia Yan. «Design, analysis and experiments of an omni-directional spherical robot». In: *Proceedings - IEEE International Conference on Robotics and Automation.* 2011, pp. 4921–4926. ISBN: 9781612843865. DOI: `10.1109/ICRA.2011.5980491` (cit. on p. 12).

[19] Akash Singh, Anshul Paigwar, Sai Teja Manchukanti, Manish Saroya, and Shital Chiddarwar. «Design and motion analysis of Compliant Omni-directional Spherical Modular Snake Robot (COSMOS)». In: *2018 International Conference on Reconfigurable Mechanisms and Robots, ReMAR 2018 - Proceedings.* Institute of Electrical and Electronics Engineers Inc., Aug. 2018. ISBN: 9781538663806. DOI: `10.1109/REMAR.2018.8449830` (cit. on pp. 12, 13).

[20] Prithvi Akella, Oliver M. O'Reilly, and Koushil Sreenath. «Controlling the locomotion of spherical robots or why BB-8 works». In: *Journal of Mechanisms and Robotics* 11.2 (Apr. 2019). ISSN: 19424310. DOI: `10.1115/1.4042296` (cit. on pp. 12, 13).

[21] Shengju Sang, Jichao Zhao, Hao Wu, Shoujun Chen, and Qi An. «Modeling and simulation of a spherical mobile robot». In: *Computer Science and Information Systems* 7.1 (Feb. 2010), pp. 51–62. ISSN: 18200214. DOI: `10.2298/CSIS1001051S` (cit. on p. 14).

[22] Seyed Amir Tafrishi, Sandor M. Veres, Esmaeil Esmaeilzadeh, and Mikhail Svinin. «Dynamical Behavior Investigation and Analysis of Novel Mechanism for Simulated Spherical Robot named "RollRoller"». In: (Oct. 2016). arXiv: `1610.06218`. URL: `http://arxiv.org/abs/1610.06218` (cit. on p. 14).

[23] Lianchao Jia, Zhiqiang Hu, Lingbo Geng, Yi Yang, and Chao Wang. «The concept design of a mobile amphibious spherical robot for underwater operation». In: *6th Annual IEEE International Conference on Cyber Technology in Automation, Control and Intelligent Systems, IEEE-CYBER 2016.* Institute of Electrical and Electronics Engineers Inc., Sept. 2016, pp. 411–415. ISBN: 9781509027323. DOI: `10.1109/CYBER.2016.7574860` (cit. on pp. 14, 15).

[24] Takeshi Aoki, Keisuke Asami, Satoshi Ito, and Shotaro Waki. «Development of quadruped walking robot with spherical shell: improvement of climbing over a step». In: *ROBOMECH Journal* 7.1 (Dec. 2020). ISSN: 21974225. DOI: `10.1186/s40648-020-00170-5` (cit. on pp. 16, 17).

[25] Supaphon Kamon, Natthaphon Bunathuek, and Pudit Laksanacharoen. «A three-legged reconfigurable spherical robot No.3». In: *2021 30th IEEE International Conference on Robot and Human Interactive Communication, RO-MAN 2021*. Institute of Electrical and Electronics Engineers Inc., Aug. 2021, pp. 426–433. ISBN: 9781665404921. DOI: `10.1109/RO-MAN50785.2021.9515319` (cit. on p. 16).

[26] Jie Pan, Zhen Yun Shi, and Tian Miao Wang. «Variable-model SMA-driven spherical robot». In: *Science China Technological Sciences* 62.8 (Aug. 2019), pp. 1401–1411. ISSN: 18691900. DOI: `10.1007/s11431-018-9408-3` (cit. on pp. 17, 18).

[27] Natthaphon Bun-Athuek and Pudit Laksanacharoen. «Simulation of a reconfigurable spherical robot IV for confined environment». In: *IEEE Region 10 Annual International Conference, Proceedings/TENCON*. Vol. 2020-Novem. Institute of Electrical and Electronics Engineers Inc., Nov. 2020, pp. 1058–1062. ISBN: 9781728184555. DOI: `10.1109/TENCON50793.2020.9293694` (cit. on p. 17).

[28] Maoxun Li, Shuxiang Guo, Hideyuki Hirata, and Hidenori Ishihara. «Design and performance evaluation of an amphibious spherical robot». In: *Robotics and Autonomous Systems* 64 (Feb. 2015), pp. 21–34. ISSN: 09218890. DOI: `10.1016/j.robot.2014.11.007` (cit. on p. 18).

[29] Kuan Yi Ho and N. Michael Mayer. «Implementation of a mobile spherical robot with shape-changed inflatable structures». In: *International Conference on Advanced Robotics and Intelligent Systems, ARIS*. Vol. 2017-Septe. 2018. ISBN: 9781538624197. DOI: `10.1109/ARIS.2017.8297199` (cit. on p. 19).

[30] Mengjie Zhang, Bo Chai, Lijuan Cheng, Zhaowu Sun, Guang Yao, and Lei Zhou. *Multi-Movement Spherical Robot Design and Implementation*. 2018 IEEE International Conference on Mechatronics and Automation (ICMA), 2018, pp. 1464–1468. ISBN: 9781538660751 (cit. on p. 19).

[31] Guanghui Shu, Qiang Zhan, and Yao Cai. «Motion control of spherical robot based on conservation of angular momentum». In: *2009 IEEE International Conference on Mechatronics and Automation, ICMA 2009*. 2009, pp. 599–604. ISBN: 9781424426935. DOI: `10.1109/ICMA.2009.5245059` (cit. on p. 21).

[32] Qingxuan Jia, Yili Zheng, Hanxu Sun, Hongyu Cao, and Hongyi Li. «Motion control of a novel spherical robot equipped with a flywheel». In: *2009 IEEE International Conference on Information and Automation, ICIA 2009*. 2009, pp. 893–898. ISBN: 9781424436088. DOI: `10.1109/ICINFA.2009.5205045` (cit. on p. 22).

[33] E. V. Potapov, A. A. Ipatov, A. L. Priorov, and A. A. Romanov. «Developing Spherical Mobile Devices for Indoor Exploration». In: *2020 Systems of Signal Synchronization, Generating and Processing in Telecommunications, SYNCHROINFO 2020*. 2020, pp. 1–4. ISBN: 9781728160726. DOI: `10.1109/SYNCHROINFO49631.2020.9166095` (cit. on p. 23).

[34] Wei Jer Chang, Chih Ling Chang, Jen Hung Ho, and Pei Chun Lin. «Design and implementation of a novel spherical robot with rolling and leaping capability». In: *Mechanism and Machine Theory* 171 (May 2022). ISSN: 0094114X. DOI: `10.1016/j.mechmachtheory.2022.104747` (cit. on p. 23).

[35] Yangyang Dong, Tongle Zhang, Shaojie Han, Yipan Guo, Bo Zeng, Yongbin Wang, and Zijian Zhang. «Spherical robot with spring energy storage type hopping mechanisms: design, dynamics and experimental evaluation». In: *Industrial Robot* 49.4 (June 2022), pp. 760–769. ISSN: 0143991X. DOI: `10.1108/IR-08-2021-0172` (cit. on p. 23).

[36] Christopher J. Dudley, Alexander C. Woods, and Kam K. Leang. «A micro spherical rolling and flying robot». In: *IEEE International Conference on Intelligent Robots and Systems*. Vol. 2015-Decem. Institute of Electrical and Electronics Engineers Inc., Dec. 2015, pp. 5863–5869. ISBN: 9781479999941. DOI: `10.1109/IROS.2015.7354210` (cit. on p. 24).

[37] Sahand Sabet, Ali Akbar Agha-Mohammadi, Andrea Tagliabue, D. Sawyer Elliott, and Parviz E. Nikravesh. «Rollocopter: An Energy-Aware Hybrid Aerial-Ground Mobility for Extreme Terrains». In: *IEEE Aerospace Conference Proceedings*. Vol. 2019-March. IEEE Computer Society, Mar. 2019. ISBN: 9781538668542. DOI: `10.1109/AERO.2019.8741685` (cit. on p. 24).

[38] Liwei Shi et al. «A Fuzzy PID Algorithm for a Novel Miniature Spherical Robots with Three-dimensional Underwater Motion Control». In: *Journal of Bionic Engineering* 17.5 (Sept. 2020), pp. 959–969. ISSN: 25432141. DOI: `10.1007/s42235-020-0087-3` (cit. on p. 25).

[39] Shuoxin Gu, Shuxiang Guo, and Liang Zheng. «A highly stable and efficient spherical underwater robot with hybrid propulsion devices». In: *Autonomous Robots* 44.5 (May 2020), pp. 759–771. ISSN: 15737527. DOI: `10.1007/s10514-019-09895-8` (cit. on p. 25).

[40] Tuanjie Li and Weigang Liu. «Design and Analysis of a Wind-Driven Spherical Robot with Multiple Shapes for Environment Exploration». In: *Journal of Aerospace Engineering* 24.1 (2011), pp. 135–139. ISSN: 0893-1321. DOI: `10.1061/(asce)as.1943-5525.0000063` (cit. on p. 25).

[41] G. (Giancarlo) Genta. *Kinetic energy storage : theory and practice of advanced flywheel systems*. Butterworths, 1985, p. 362. ISBN: 0408013966 (cit. on pp. 56, 59).

[42] Johan Abrahamsson, Janaína Gonçalves de Oliveira, Juan de Santiago, Johan Lundin, and Hans Bernhoff. «On the efficiency of a two-power-level flywheel-based all-electric driveline». In: *Energies* 5 (8 2012), pp. 2794–2817. ISSN: 19961073. DOI: `10.3390/en5082794` (cit. on pp. 56, 57, 59).

[43] Sergej Sirigu Antonello, Gallizio Federico, Giorgi Giuseppe, Mauro Bonfanti, Bracco Giovanni, and Mattiazzo Giuliana. «Numerical and experimental identification of the aerodynamic power losses of the ISWEC». In: *Journal of Marine Science and Engineering* 8 (1 Jan. 2020). ISSN: 20771312. DOI: `10.3390/jmse8010049` (cit. on pp. 57, 59).

[44] James W. Daily and Ronald E. Nece. «Chamber Dimension Effects on Induced Flow and Frictional Resistance of Enclosed Rotating Disks». In: *Journal of Basic Engineering* 82 (1960), pp. 217–230 (cit. on p. 58).

[45] Steve Miller. *Simscape Multibody Contact Forces Library.* 2023. URL: `https://it.mathworks.com/matlabcentral/fileexchange/47417-simscape-multibody-contact-forces-library` (cit. on pp. 81, 82).